



**HAL**  
open science

# Development of new bioanalytical tool for the detection and monitoring of breast cancer biomarkers via saliva

Imad Abrao Nemeir

## ► To cite this version:

Imad Abrao Nemeir. Development of new bioanalytical tool for the detection and monitoring of breast cancer biomarkers via saliva. Biochemistry [q-bio.BM]. Université de Lyon; Université Saint-Esprit (Kaslik, Liban), 2020. English. NNT : 2020LYSE1159 . tel-03592539

**HAL Id: tel-03592539**

**<https://theses.hal.science/tel-03592539>**

Submitted on 1 Mar 2022

**HAL** is a multi-disciplinary open access archive for the deposit and dissemination of scientific research documents, whether they are published or not. The documents may come from teaching and research institutions in France or abroad, or from public or private research centers.

L'archive ouverte pluridisciplinaire **HAL**, est destinée au dépôt et à la diffusion de documents scientifiques de niveau recherche, publiés ou non, émanant des établissements d'enseignement et de recherche français ou étrangers, des laboratoires publics ou privés.



Holy Spirit  
University  
of Kaslik

N°d'ordre NNT : 2020LYSE1159

## THESE de DOCTORAT EN COTUTELLE DE L'UNIVERSITE DE LYON

opérée au sein de  
l'Université Claude Bernard Lyon 1  
L'université Saint-Esprit de Kaslik

Ecole Doctorale de chimie de Lyon  
Faculté des Arts et des Sciences

**Spécialité de doctorat** : Analytical Biochemistry

**Discipline** : Chemistry

Soutenue publiquement le 30/09/2020, par :

**Imad Abrao Nemeir**

---

# Development of new bioanalytical tool for the detection and monitoring of breast cancer biomarkers via saliva

---

Devant le jury composé de :

LEONARD Didier	Professeur des universités UCBL-1	Président de Jury
JABBOUR Jihane	Professeure Université Libanaise-Fanar	Rapporteure
KORRI-YOUSSOUFI Hafsa	Directrice de Recherche CNRS Paris	Rapporteure
YAAKOUBI Nourdin	Maitre de conférences université de Mans	Examineur
ZERROUKI Chouki	Maitre de conférences CNAM-Paris	Examineur
ERRACHID EL-SALHI Abdelhamid	Professeur des universités UCBL-1	Directeur de thèse
SAAB Joseph	Professeur USEK	Directeur de thèse
HLEIHEL Walid	Professeur Associé USEK	Co-directeur de thèse
ZINE-LOUKILI Nadia	Maitre de conférences UCBL-1	Invitée



## **DEDICATION**

I dedicate this thesis first to God and Jesus Christ for giving me the patience and perseverance to see this project through to the end.

I would like to give thanks to my parents and sister for giving me their full support during my studies.

I would like to give thanks to my friends which made my time an enjoyable ride.

I would like to give thanks to all the people I annoyed to no end and who kept supporting me despite my being a nuisance to them.

I would like to thank 2020 for not being so apocalyptic as to delay my thesis defense till 2021.

## **ACKNOWLEDGMENTS**

I would like to give thanks to the UK Lebanon Tech hub for financing and supporting my thesis.

I would like to thank my advisors, Dean Joseph Saab, Prof. Abdelhamid Errachid, Doc. Nadia Zine, Doc. Walid Hleihel, who read my numerous revisions and helped make some sense of the confusion. Also thanks to my committee members, Didier Leonord, Jabbour Jihane, Korri-Youssoufi Hafsa. Nourdin Yaakoubi, and Chouki Zerrouki, who offered guidance and support.

I would also like to thank the University staff and experts without whom I would not have been able to complete the surveys and the analysis.

Last but not the least, I would like to thank my colleagues for their support and encouragement.

## ABSTRACT

Breast cancer affects 1 in 8 women globally. In 2018 alone, an additional 2 million new cases with 626000 deaths from breast cancer have been recorded. Treatment effectiveness and survivability can be increased with early detection. However, current early detection methods used for breast cancer are both invasive and costly. A popular alternative method, biosensors are devices that detect biological molecules at low concentrations with high precision and low cost. In recent years, saliva as a detection medium has been proven to be an excellent alternative to blood and tissue due to the fact that it is rich in protein biomarkers including breast cancer biomarkers. As such, this thesis aims to develop a biosensor for the detection of breast cancer biomarkers in saliva.

Three biosensors for the detection of each salivary breast cancer biomarkers (Epidermal Growth factor receptor (EGFR), Human epidermal receptor 2 (HER2), Tumor protein 53 (p53)) have been developed. Electrochemical impedance spectroscopy (EIS) have been used for the characterization of the biosensors, and for the detection of all three biomarkers. The biosensors have shown good sensitivity toward their respective biomarkers in their concentration ranges found in saliva, they showed also good selectivity when compared with other salivary breast cancer biomarkers, and finally they showed excellent accuracy when detecting the biomarkers in both real and artificial saliva using the standard addition method.

**Keywords:** Biosensors, EIS, breast cancer, saliva, EGFR, HER2, p53, electrochemical impedance spectroscopy.

## RÉSUMÉ

Le cancer du sein affecte 1 femme sur 8 dans le monde. Rien qu'en 2018, 2 millions de nouveaux cas supplémentaires ont été enregistrés avec 626000 décès par cancer du sein. L'efficacité du traitement et la capacité de survie peuvent être augmentées grâce à une détection précoce. Cependant, les méthodes actuelles de détection précoce utilisées pour le cancer du sein sont à la fois invasives et coûteuses. Les biocapteurs présentent une méthode alternative. Ce sont des dispositifs qui détectent les molécules biologiques à de faibles concentrations avec une grande précision et un faible coût. Récemment, la salive en tant que milieu de détection s'est avérée être une excellente alternative au sang et aux tissus en raison de sa richesse en biomarqueurs protéiques, y compris les biomarqueurs du cancer du sein. Cette thèse vise donc à développer un biocapteur pour la détection de biomarqueurs du cancer du sein dans la salive.

Trois biocapteurs pour la détection de chacun des biomarqueurs du cancer du sein salivaire EGFR (*Epidermal Growth factor receptor*), HER2 (*Human epidermal receptor 2*), p53 (*Tumor protein 53*) ont été développés. La spectroscopie d'impédance électrochimique (SIE) a été utilisée pour la caractérisation des biocapteurs et pour la détection des trois biomarqueurs. Les biocapteurs ont montré une bonne sensibilité dans les gammes de concentrations trouvées dans la salive, ils ont montré aussi une bonne sélectivité par rapport à d'autres biomarqueurs du cancer du sein salivaire, et enfin ils ont montré une excellente précision lors de la détection des biomarqueurs dans la salive réelle et artificielle en utilisant la méthode des ajouts dosés.

**Mots clés:** biocapteur, cancer de sein, EIS, HER2, EGFR, p53, Impedance spectroscopic

**TABLE OF CONTENTS**

<b>DEDICATION</b>	<b>III</b>
<b>ACKNOWLEDGMENTS</b>	<b>IV</b>
<b>ABSTRACT</b>	<b>V</b>
<b>TABLE OF CONTENTS</b>	<b>VII</b>
<b>LIST OF ABBREVIATIONS</b>	<b>XII</b>
<b>LIST OF SYMBOLS</b>	<b>XIV</b>
<b>LIST OF TABLES</b>	<b>XVI</b>
<b>LIST OF FIGURES</b>	<b>XVII</b>
<b>INTRODUCTION</b>	<b>1</b>
<b>CHAPTER 1</b>	
<b>LITERATURE REVIEW</b>	<b>4</b>
<i>1.1 Introduction to Biosensors.</i>	<i>4</i>
<i>1.2 Interfacial Chemistry</i>	<i>6</i>
1.2.1 Screen Printed Electrodes	7
1.2.2 Voltammetry techniques	11
1.2.3 Surface Modification	15
1.2.4 Electrochemical Impedance Spectroscopy	18
<i>1.3 Breast Cancer</i>	<i>32</i>
1.3.1 P53	36
1.3.2 MUC1	37
1.3.3 Human epidermal receptor family	38

Table of contents	viii
1.3.4 Carcinoembryonic Antigen	41
1.3.5 Vascular Endothelial Growth Factors	42
<b>CHAPTER 2</b>	
<b>DEVELOPMENT OF A BIOSENSOR FOR THE DETECTION OF EGFR</b>	<b>43</b>
<i>Objective</i>	43
2.1 <i>Introduction</i>	44
2.1.1 Structure	44
2.1.2 Signaling pathway	45
2.1.3 Clinicology of EGFR	47
2.2 <i>Materials and Methods</i>	48
2.2.1 Materials	48
2.2.2 Methods	49
2.3 <i>Results and discussion</i>	54
2.3.1 CMA electrodeposition	54
2.3.3 Detection of EGFR, HER2 and HER3	54
2.3.4 Effect study of artificial saliva on the biosensor	57
2.3.5 Detection of EGFR in artificial saliva using the standard addition method.	58
2.4 <i>Conclusion</i>	61
<b>CHAPTER 3</b>	
<b>DEVELOPMENT OF A BIOSENSOR FOR THE DETECTION OF P53</b>	<b>62</b>
<i>Objective</i>	62
3.1 <i>Introduction</i>	63
3.1.1 P53 structure	63
3.1.2 P53 functions in breast cancer	64

3.1.3 Clinicology of p53 in breast cancer	65
<i>3.2 Experimental</i>	<i>66</i>
3.2.1 Materials	66
3.2.2 Methods	67
<i>3.3 Results</i>	<i>70</i>
3.3.1 CMA electrodeposition	70
3.3.2 EIS measurements of p53	71
3.3.3 Detection of p53 using Bradford.	75
3.3.4 Detection of p53 in artificial saliva.	76
<i>3.4 Conclusion</i>	<i>80</i>
<b>CHAPTER 4</b>	
<b>DEVELOPMENT OF A BIOSENSOR FOR THE DETECTION OF HER2</b>	<b>81</b>
<i>Objective</i>	<i>81</i>
<i>4.1 Introduction</i>	<i>82</i>
4.1.1 Structure of HER2	82
4.1.2 Signaling pathway	83
4.1.3 HER2 and breast cancer	84
4.1.4 HER2 detection	85
<i>4.2 Materials and methods</i>	<i>86</i>
4.2.1 Materials	86
4.2.2 Methods	87
<i>4.3 Results</i>	<i>90</i>
4.3.1 ABA electrodeposition	90
4.3.2 Measurement of HER2 concentration in PBS.	90
4.3.3 Measurement of HER2 concentration in real saliva.	94
<i>4.4 Conclusion</i>	<i>98</i>

<b>CONCLUSION AND PERSPECTIVE</b>	<b>99</b>
<b>ARTICLES PUBLISHED</b>	<b>102</b>
<b>CONFERENCE ATTENDED</b>	<b>104</b>
<b>REFERENCES</b>	<b>105</b>
<b>APPENDIXES</b>	<b>116</b>
<i>Appendix A</i>	<i>116</i>
<i>Design and fabrication of the transducer</i>	<i>116</i>
Fabrication process	117
<i>Appendix B</i>	<i>121</i>
<i>Optimization of CMA electrodeposition</i>	<i>121</i>
Introduction	121
Method	121
Results	122
Conclusion	125
<i>Appendix C</i>	<i>126</i>
<i>Optimization of EDC/NHS for antibody immobilization</i>	<i>126</i>
Introduction	126
Method	126
Results	127
Optimization of anti-EGFR antibody immobilization	127
Conclusion	129
<i>Appendix D</i>	<i>130</i>
<i>Optimization of ABA electrodeposition</i>	<i>130</i>
Introduction	130
Method	130
Results	132

Table of contents	xi
Conclusion	138
<i>References</i>	<i>138</i>

**LIST OF ABBREVIATIONS**

EGFR	Epidermal growth factor receptor
p53	Tumor protein 53
HER2/3/4	Human epidermal receptor 2 and 3 and 4
MUC1	Mucin 1
CA 15-3	Cancer antigen 15-3
CA 27.29	Cancer antigen 27.29
CEA	Carcinoembryonic antigen
VEGF	Vascular Endothelial Growth Factors
L1/2	Ligand binding domains1 and 2
CR1/2	Cysteine-rich domains
AKT1	Protein kinase B oncogene
STAT3	Signal transducer and activator of transcription 3
RAS	rat sarcoma oncoprotein family
Ras/MAPK	Ras Mitogen-activated protein kinase
PI3K/AKT	Akt phosphatidylinositol (3,4,5) trisphosphate activated by phosphoinositide 3-kinase
TIGAR	TP53-induced glycolysis and apoptosis regulator
TAD1/2	The N-terminal transactivation domain1/2
PRD	Pro-rich domain
DBD	DNA binding domain
TD	tetramerization domain
BD	the C-terminal basic domain
DNA	Deoxyribonucleic acid

SPE	Screen-printed electrodes
IUPAC	International Union of Pure and Applied Chemistry
CA	Chronoamperometry
LSV	Linear sweep voltammetry
CV	Cyclic voltammetry
EIS	Electrochemical impedance spectroscopy
R	resistance
C	capacitance
CPE	Constant phase element
W	Warburg impedance
EDC	N-(3-dimethylaminopropyl)-N-ethyl- carbodiimide hydrochloride
NHS	N-hydroxysuccinimide
CMA	Carboxymethyl aniline
ABA	Aminobenzoic acid
PBS	Phosphate buffer saline solution
HCl	hydrochloric acid
NaNO <sub>2</sub>	sodium nitrite

**LIST OF SYMBOLS**

$E_0$	Start potential
$E_t$	Potential at time t
$E$	Applied potential
$E^0$	Formal potential of the given species
$R$	Universal gas constant
$T$	Temperature
$n$	Number of electron transfer
$F$	Faradaic constant
$i_p$	peak's intensity value
$A$	electrode's electroactive area
$C$	bulk solution concentration
$D$	analyte diffusion coefficient
$v$	scan rate
$Z$	Total impedance
$Z'$	Real impedance
$Z''$	Imaginary impedance
$U$	Given resistance
$i$	Current intensity
$\omega$	Angular frequency
$f$	frequency
$\theta$	Phase difference
$j$	Imaginary number
$V_T$	Thermal potential
$k$	Boltzmann constant
$e$	Photon charge
$R_s$	Solution resistance
$C_{dl}$	Double layer capacitance

$R_{ct}$	Charge transfer resistance
$Z_w$	Warburg impedance
$k_{ox}/k_{red}$	Heterogeneous rate constants of the oxidation reaction/reduction reaction
$C_{o(0)}/C_{r(0)}$	Concentrations of the oxidant and reducer on the electrode's surface
$k_0$	Heterogeneous rate constant at the standard potential
$\alpha$	Transfer coefficient
$E_{1/2}$	reversible half-wave potential
$D_o/D_r$	Diffusion coefficient of the oxidant and reducer
$\xi$	Square root of the divided diffusion coefficients of the oxidant and reducer
$l$	Depth
$r$	Radius
$Z_{wo}/Z_{wr}$	Specific impedances of the oxidant and reducer species
$\sigma'/\sigma$	Mass transfer coefficient
$\sigma'_o/\sigma'_r$	Specific mass transfer coefficients for each of the oxidant and reducer
$Q$	CPE's coefficient
$Z_{CPE}$	Impedance value of CPE element
$\eta$	CPE's exponent

## LIST OF TABLES

<b>Table 1:</b> Modelization result of the EGFR Nyquist plot.	55
<b>Table 2:</b> List of electrochemical biosensors developed for the detection of EGFR.	60
<b>Table 3:</b> Result of the fitting of the Nyquist plots of p53 concentrations.	73
<b>Table 4:</b> List of p53 biosensors, their assay types, detection techniques, optimization, functional range, the limit of detection, and medium of detection.	78
<b>Table 5:</b> resulting parameters from the modelization of HER2 detection.	93
<b>Table 6:</b> List of biosensors for the detection of HER2.	96
<b>Table 7:</b> Summary of the Mask Steps Designed for the Fabrication of the Lab-on-a-chip	117

## LIST OF FIGURES

- Figure 1:** Scheme showing the large versatility of biosensors through exploring the large choice in their components [8]. 5
- Figure 2:** Example of interfaces used in electrochemistry [10]. 7
- Figure 3:** The search results from ISI Web of Knowledge showing (a) the number of articles per year (b) number of citations per year (c) countries of contribution for these articles with “screen printed electrode” as key search words [15]. 9
- Figure 4:** Screen printing fabrication process [15]. 10
- Figure 5:** List of chemical components of the ink used in SPE production [14]. 11
- Figure 6:** Voltammetric methods and their graphic representation showing a) Chronoamperometry, b) Linear sweep voltammetry, c) Cyclic voltammetry, d) Staircase voltammetry, e) differential sweep voltammetry, Square wave voltammetry, AC voltammetry [19]. 12
- Figure 7:** A typical CV experiment showing: from A to G the concentration profile of the electrode, H the cyclo-voltammogram, and I the applied potential in relation to time [21]. 13
- Figure 8:** Example of diazonium deposition [26]. 16
- Figure 9:** Example of the anti-fouling property of diazonium deposition [26]. 17
- Figure 10:** EDC/NHS amide formation reaction mechanism [27]. 18
- Figure 11:** Representation of an impedimetric vector, also called an angram diagram, with its real and imaginary components in relation to the phase shift  $\theta$  [32]. 21

- Figure 12:** Example of tridimensional impedance plot (in  $\Omega$ ), generated by ZView [31]. 23
- Figure 13:** Randle circuit and its impedance spectrum with a)Nyquist plot, b)Impedance Bode plot and c) phase angle bode plot [31]. 24
- Figure 14:** Effect of the analyte concentration (A), potential applied (B) and porosity (C) on the shape of the Nyquist plot of a given electrode's surface [31]. 27
- Figure 15:** The modelization of two semicircle circuit's impedance spectra with a)Nyquist plot, b)Impedance Bode plot and c) phase angle bode plot showing  $R_0 = 10 \Omega$ ,  $R_1 = R_2 = 100 \Omega$ ,  $C_1 = 20 \mu\text{F}$  with varying  $C_2$  ( $0.1, 10^{-3}, 10^{-4}, 2 \times 10^{-5}$ , and  $10^{-5}$ ) which are represent [31]. 28
- Figure 16:** Global percentage of incidence and mortality by cancer site for both sexes (A), Males only (B) and female only (C) [37]. 32
- Figure 17:** The decision tree for breast cancer therapy in regards to Molecular classifications [43]. 35
- Figure 18:** Role of p53 in cells [47]. 37
- Figure 19:** activation of MUC1 subunits in cancer cells [50]. 38
- Figure 20:** Different subtypes of HER family and their respective ligands [52]. 39
- Figure 21:** Downstream signaling pathways result from the dimerization of EGFR and HER2 [52]. 41
- Figure 22:** Schematic of EGFR structure [57]. 45
- Figure 23:** non-kinase pathways of EGFR and their outcomes showing EGFR role in A) preventing autophagy, B) inhibiting pro-apoptotic proteins, and C) regulating gene transcription pathways [51]. 46
- Figure 24:** Canonical actions of the EGFR signaling pathway [60]. 47
- Figure 25:** (A) A picture of the microfluidic system, (B) The nutplug and the PTFE tubes attached to the channels, (C) the rubber rings that seal the channel, (D) first step in closing the system, (E) the second step in closing

the system, (F) the experimental set-up, (G) Filling the microfluidic system with solutions. 50

**Figure 26:** Nyquist plots showing the EIS measurements of EGF concentrations with the measurement after the immobilization of anti-EGFR antibody in black, after incubation of 50 pg/mL EGFR in red, 80 pg/mL EGFR in blue, 100 pg/mL EGFR in green, and 120 pg/mL EGFR in magenta 54

**Figure 27:** Equivalent circuit used in the modelization of the Nyquist plots. 55

**Figure 28:** Standardization curve of the detection of EGFR (black), HER2 (red), and HER3 (blue) showing the normalized signal versus the concentration of the proteins in pg/mL. 56

**Figure 29:** Effect of artificial saliva concentration on the biosensor. 58

**Figure 30:** Plot showing the detection of EGFR in artificial saliva using the standard addition method. 59

**Figure 31:** Structure of p53 showing A the relative position of each domain, B the structure of each domain, and C the dimer surface of each domain [65]. 64

**Figure 32:** Activation pathway of p53 through hormone or cellular stresses [48]. 65

**Figure 33:** percentage of mutation in BRCA1 breast cancer and other types of breast cancer [68]. 65

**Figure 34:** Schematic of the Bradford assay. 69

**Figure 35:** (A) reactions for the electrodeposition of CMA on gold SPE, (B) cyclo-voltammogram for the electrodeposition of CMA, (C) CV characterization of SPE before and after electrodeposition. 71

**Figure 36:** The Nyquist plot of a typical detection of p53 showing the variation of different concentrations (from anti-p53 (black), 1 (red), 4 (blue), 7 (green), 10 (magenta)  $\mu\text{g/mL}$ ). 72

- Figure 37:** Equivalent circuit used for the fitting of the Nyquist plot. 73
- Figure 38:** Graphical representation of the detection of p53 showing (A) the standardization curves of p53 (black), the interferences HER3(red) and MUC1(blue), and their respective equations 74
- Figure 39:** Absorbance of the Bradford assay for each p53 concentration before and after incubation on the electrode's surface. 75
- Figure 40:** detection of p53 in artificial saliva using the standard addition method. 76
- Figure 41:** (A) HER2 secondary structure (B) HER2 tertiary structure (C) Schematic of HER2 structure [78]. 83
- Figure 42:** Signaling pathways of HER2 dimerization [79]. 84
- Figure 43:** Location of trastuzumab drug and lapatinib drug activity in breast cancer [80]. 85
- Figure 44:** salivary HER2 concentration in relation to HER2 tissue expression in breast cancer [82]. 86
- Figure 45:** Nyquist plot showing the measurements of the different concentrations of HER2 starting with the Nyquist from the immobilization of anti-HER2 antibodies (black), then 5 pg/mL HER2 (red), 10 pg/mL HER2 (blue), then 20 pg/mL HER2 (green), then finally 40 pg/mL HER2 (magenta). 90
- Figure 46:** Bode plot showing the impedance Bode in dots and the phase degree shift in stars versus the logarithm of the frequencies for the EIS measurements of HER2 concentrations starting with the immobilization of anti-HER2 antibodies (black), then 5 pg/mL HER2 (red), 10 pg/mL HER2 (blue), then 20 pg/mL HER2 (green), then finally 40 pg/mL HER2 (magenta). 91
- Figure 47:** Equivalent circuit used for the modelization of the measurement of HER2 concentrations. 92

- Figure 48:** Standardization curves for the detection of HER2 (black) with the detection of the interference proteins EGFR (red) and HER3 (blue). 94
- Figure 49:** Detection of HER2 concentration in real saliva using the standard addition method. 95
- Figure 50:** Design and proportions of the transducer. 117
- Figure 51:** the dimensions of the biotransducers showing the result of the applied first four masks in (A) and the fifth and final mask in (B) 119
- Figure 52:** Scheme showing the steps taken for the optimization of CMA electrodeposition parameters. 122
- Figure 53:** passivation layers resulting from different cycles of electrodeposition of CMA. 123
- Figure 54:** Sensitivity of the biosensor in relation to the number of cycles. 123
- Figure 55:** Passivation layer resulting from the electrodeposition of CMA at different scan rates. 124
- Figure 56:** passivation layer resulting from the electrodeposition of CMA at the different potential window of detection. 125
- Figure 57:** Schematic summarizing the optimization done for the immobilization of antibody anti-EGFR showing the optimization of the concentration of EDC/NHS (A) and the optimization of the time (B). 127
- Figure 58:** Optimization of EDC/NHS concentration showing the sensitivity of the detection against the concentration of EDC/NHS used. 128
- Figure 59:** Optimization of the SPE incubation time in EDC/NHS and in the antibody anti-EGFR showing the sensitivity of the detection against the incubation time. 129
- Figure 60:** The optimization scheme for ABA electrodeposition through (A) CV parameters, (B) Chemical parameters. 132

- Figure 61:** Electrodeposition using the literature electrodeposition parameters. 133
- Figure 62:** CV showing the result of the optimization of the number of cycles after the electrodeposition of ABA. 133
- Figure 63:** CV showing the result of the optimization of the scan rate after the electrodeposition of ABA. 134
- Figure 64:** CV showing the result of the optimization of the potential window after the electrodeposition of ABA. 134
- Figure 65:** CV showing the resulting electrodeposition when ABA was incubated with ice and without ice. 135
- Figure 66:** CV showing the resulting passivation layer from different ABA incubation time. 136
- Figure 67:** CV showing the resulting passivation layer from different ABA concentrations. 136
- Figure 68:** CV showing the resulting passivation layer from different methods of preparing ABA. 137
- Figure 69:** Difference between the electrodeposition of ABA with the original parameters, and with the optimized parameters. 138

## INTRODUCTION

Breast cancer is one of the most impactful cancers around the world, touching an additional 2 million women and accounting for 25% of all cancer cases globally. In addition to its widespread, breast cancer is also a notorious disease to treat due to its heterogeneity and molecular and genetic diversity. However, one feature of breast cancer is that it has a linear progression that can be classified. As such, the treatment of breast cancer is best when it is caught during its early stages [1].

The methods for detecting breast cancer are numerous; imaging methods are the most relied upon with mammography being the golden standard for breast cancer detection. However, imaging techniques are expensive to set up and to operate. They are also bulky and hard to transport which makes them hard to adopt in impoverished nations. Biopsy, and subsequently all techniques that rely on it, is the most relied on technique for breast cancer classification, however, it is the most invasive and carries a lot of risks. Blood analysis is the most relied on for monitoring breast cancer progression, prognosis, and therapy, however, like a biopsy, it remains invasive and expensive. Because of these drawbacks, the current breast cancer detection methods are less than optimal [1,2].

As such, scientists have been looking for an alternative for these detection methods, and saliva is showing to be one of them. Saliva is the fluid secreted in the buccal cavity to aid in digestion, while that is its main function, closer studies have shown that saliva has a large number of disease-related biomarkers prompting some to call it the mirror of the body [3]. Also,

several studies have shown that saliva is rich in breast cancer biomarkers [4], making it an excellent alternative to blood in the analysis of breast cancer.

But there are a few issues that prevent saliva from becoming truly an alternative to blood. The first one is the concentration of breast cancer biomarkers found in saliva is far lower than for it be detected in any commercially viable means [1,5]. The other is the reputation of saliva as being unreliable as a medium for the detection of proteins due to the difficulties its matrix imposes on the detection methods [1,6]. As such, new detection methods are needed to overcome these disadvantages; biosensors are molecular detection devices that offer several advantages in regards to the detection of biomarkers, they are cost-effective, precise even at low concentrations, and are easy to manipulate with minimal effects from the solution matrix [1]; as a consequence, development of a biosensor for the detection of salivary breast cancer biomarkers is a valid strategy moving forward with the evolution of breast cancer detection.

This thesis is the result of responding to this strategy. It is divided into four different chapters, the first is dedicated to a literature review, the second explains the development of a biosensor for the detection of epidermal growth factor receptor (EGFR), the second for the detection of tumor protein 53 (p53), the third and final chapter for the detection of human epidermal receptor 2 (HER2).

The first chapter in this thesis covers the state of the art of each of the techniques used for the detection, detailing the specific components of the biosensor that were employed in the strategy, the functionalization steps, detection method, and cancer biomarkers used for this detection.

The second chapter details the development of a biosensor for the detection of EGFR, the materials and methods used, as well as its detection in artificial saliva.

The third chapter details the development of a biosensor for the detection of p53, the materials methods used, as well as the validation of the detection and its detection in artificial saliva.

The fourth and final chapter details the development of a biosensor for the detection of HER2, the materials and methods used, as well as its detection in real saliva.

## CHAPTER 1

### LITERATURE REVIEW

#### 1.1 Introduction to Biosensors.

Biosensors are devices engineered to translates biological molecules' ability to recognize each other into a readable parameter that is physical. They are an attractive field of research that is reshaping how diseases are being detected due to their low detection limit while remaining highly sensitive and selective, at the same time, they are immensely versatile, which it is explained in figure 1 with flexible designs that can accommodate the detection of multiple protein biomarkers at the same time [1].

Biosensors first debut in 1984 when Cass et al designed the first amperometry glucose sensor that uses ferrocene as a probe. Then a big break to biosensors came when BIAcore in 1990 introduced surface plasmon resonance which allowed monitoring the interactions of biological molecules in real time a real possibility with over 540 measurements without loss of sensitivity, fully automated detection which significantly cut the time needed for detecting biological components. The 90s also saw a rise in DNA biosensor which used the Watson-Crick base pair recognition ability of DNA to detect DNA strands in the genome, however, functional DNA such as DNAnzymes, aptamer, and aptazymes extended the function of DNA biosensor further to detect target proteins and other molecules. Current trends in biosensor detection are the creation of more advanced biorecognition molecule through molecular biology for more robust

biosensors, miniaturization which will the creation of lab-on-chip designs which will further reduce the cost of these devices while nanomaterials needed to create these lab-on-chips greatly enhances the biosensor's sensitivity and detection range [7].

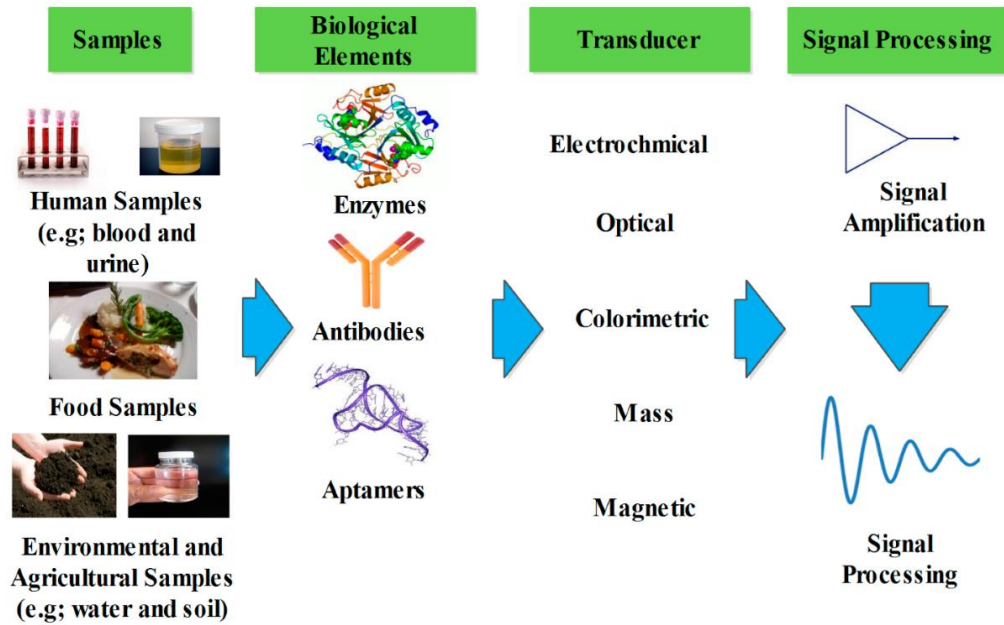


**Figure 1:** Scheme showing the large versatility of biosensors through exploring the large choice in their components [8].

## 1.2 Interfacial Chemistry

The branch of chemistry that studies the structural aspects, processes, and electrical current modifications that occur at the interface either electronic conductor and an ionic conductor, also called an electrode and electrolyte respectively, or two ionic conductors are referred to as electrochemistry.

However, the above explanation requires further expansion. By interface, we indicate that the region in which an electrode and electrolyte meet possess properties that differ much from their respective bulk solutions. This interface can be modified to a great extent, producing functional structures granting them desired properties for a multitude of purposes, from anti-corrosion to selective recognition. This interface can also denote a change in the special properties of a given surface. It is also worthy to note that an interface can be solid-liquid or liquid-liquid where the liquids in question are immiscible. Because of this, electrochemistry as a field of study also lies at the interface of both physics and chemistry, and, as such, is taught in many fields from material science to engineering [9,10].

Electrochemistry, as defined above, can thus be described as a system in which an electrode and electrolyte meet and the electrical and chemical processes that occur at their surface, with the electrode being anything from noble metals (Au and Pt), liquid metals (Hg), semiconductors (TiO<sub>2</sub>, Si), and organic layers (graphene, conductive polymers), figure 2 summarizes these interactions, while the electrolyte is any solution containing charged ions (H<sup>+</sup>, Na<sup>+</sup>, Cl<sup>-</sup>, Fe<sup>2+</sup>/Fe<sup>3+</sup>...) in either aqueous or organic solvents, however, one property of the electrolyte have to be a sufficiently high conductivity to carry the experiment. However, to think of this system as a simple electrode and electrolyte interface is too simplistic. To carry out an electrochemical experiment, an electrochemical cell is needed; this cell consists of two to

three electrodes linked together inside an electrolyte solution. This is usually done because, while one interface is where the processes are carried out, the other interfaces are used to study and follow the electrical current as it unfolds during said process [11].

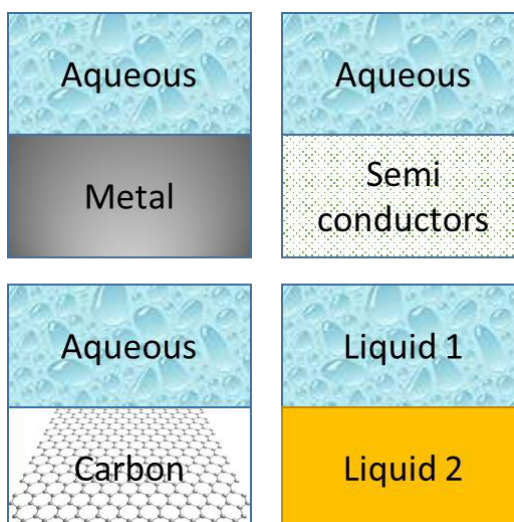


**Figure 2:** Example of interfaces used in electrochemistry [10].

In this chapter, we will explain the nature of the electrochemical cells as well as the electrochemical processes used in the experiment.

### 1.2.1 Screen Printed Electrodes

As the 21st century began in earnest, analytical studies shifted from unwieldy electrochemical cells toward the expansion of novel and robust methodologies that are characterized with being fast, easy to use, trivial, portable, inexpensive, and disposable electrode systems [12].

As such, current trends in the electrochemical analysis have geared towards screen printing technology, if the number of scientific publications is an arbiter. Besides miniaturization, screen printing is an efficient technique for large scale production of single electrodes or multiple array electrodes in various arrangements (three electrodes system for standard electrochemical cell) for simple and fast electrochemical analysis. Besides, screen printing is not limited to the type of substrate it can be used upon, granting it even more

flexibility with its design and customization. Unlike other techniques for electrode creation (Lithography) however, this customization doesn't come at the expense of cost, this gives screen printed electrodes (SPE) greater market penetration ability; cost-effective devices with immense customizability in their design and materials are essential components for the creation of highly adaptive devices which are tailor-made for a very specific purpose such as devices for the internet of things and wearable devices for direct monitoring of individual health, environmental, and even chemical warfare [13,14]. However, several issues remain prevalent with this technology, such as improper functionalization which alters the structural and functional parts of the biorecognition elements affecting these electrode's performance, necessitating optimization of the necessary biofunctionalization parameters. Other improvements to this technology are still being developed such as simplifying the scheme-of-detection, less tedious labeling of the biomarkers, simpler immobilization and amplification methods for an enhanced signal to noise ratio all the while, continued enhancement of the mass transport on the surface level as well as the use of graphene, nanoparticles and carbon nanotubes continuously for better detection at a lower concentration, and finally, the development of microarrays and the use of screen-printed electrodes in microfluidic systems allows the use of these technologies in point-of-care and even wearable devices [13]. In this part, we will focus on screen printing technology, its history, and the variety of its use.

### **1.2.1.1 History**

Growth in the development of screen printing has been exponential starting with 1992 till 2011 with China, USA, and the UK leading the race; the reason behind this growth is the rapid evolution of multidisciplinary sciences including microfabrication processes and biosensor technology.

While first-generation screen-printed electrodes were a single working electrode, the second generation was the development of auxiliary electrodes with modifiable ink composition, allowing the development of several types of electrodes such as gold electrodes for working and silver electrodes for reference. This has the effect of eliminating issues found in the classical solid electrodes, such as memory effect and complicated pre-treatment, that limited their use. Statistics on this issue can be found in figure 3.

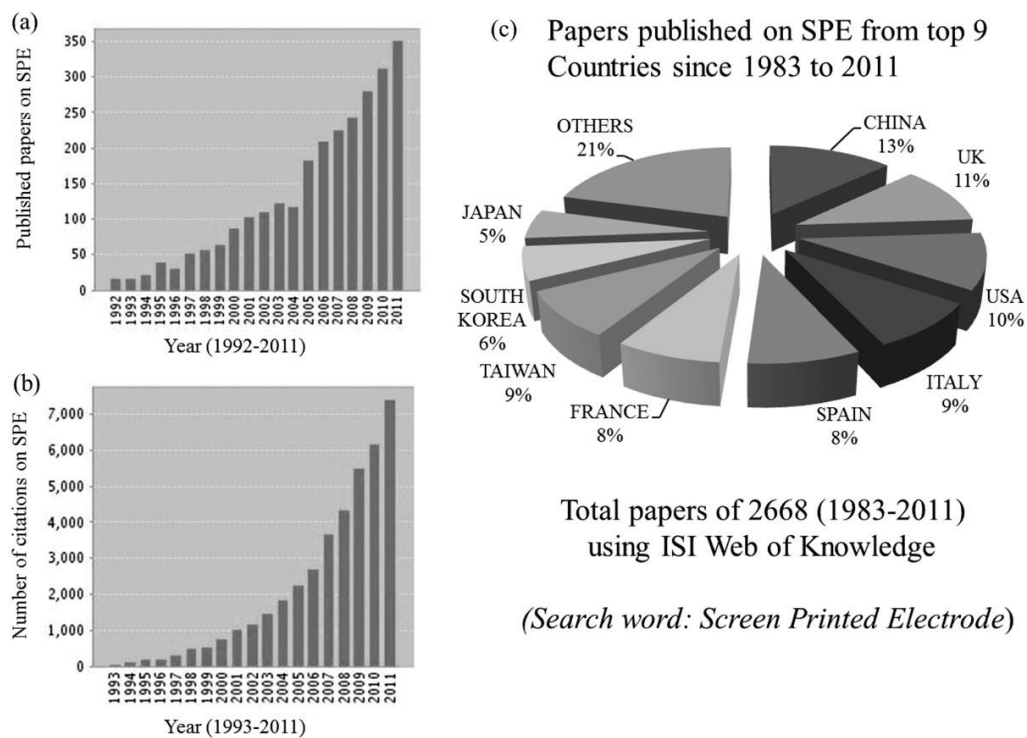


**Figure 3:** The search results from ISI Web of Knowledge showing (a) the number of articles per year (b) number of citations per year (c) countries of contribution for these articles with “screen printed electrode” as key search words [15].

### 1.2.1.2 Technology Fundamentals

The basic screen printing technology uses a blade called a squeegee to squeeze an ink or a paste made of either an organic or metallic origins through a mesh that grants it its shape and onto a substrate which could be anything from polymers [13], ceramic [16], even paper [17]. Figure 4 summarizes the entire process. However, the limitation of such a technique

is its low resolution in the fabrication of miniaturization of the created electrodes [18].

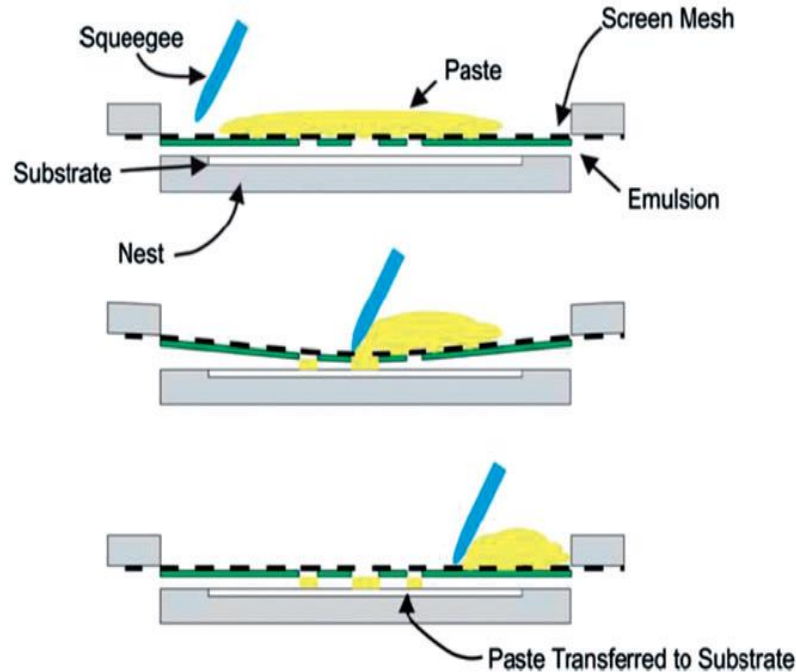


**Figure 4:** Screen printing fabrication process [15].

The ink is of particular importance as it contains all the necessary components for a functioning electrode. The ink is made up of four distinct components:

- Fillers are the conductive element of the ink, it can be made with anything from metallic, to carbon nanotubes and other tubes of nanoparticles.
- The binder helps hold all the components together, it's also what gives the ink its physical properties such as flexibility, biodegradability, or self-healing. It's also highly dependent on the properties of the filler as well as the type of application that the ink is going to be used for. Examples of binders are acrylic, silicone, styrene, fluoroelastomers, and urethane.
- The solvent is what allows the ink to flow. It needs to be soluble to the binder, all the while having good viscosity, surface tension, and homogeneity.

• Additives are the final components, they provide specific characteristics for the ink such as wetting, healing, or even stretching properties. All these properties can be found in figure 5.

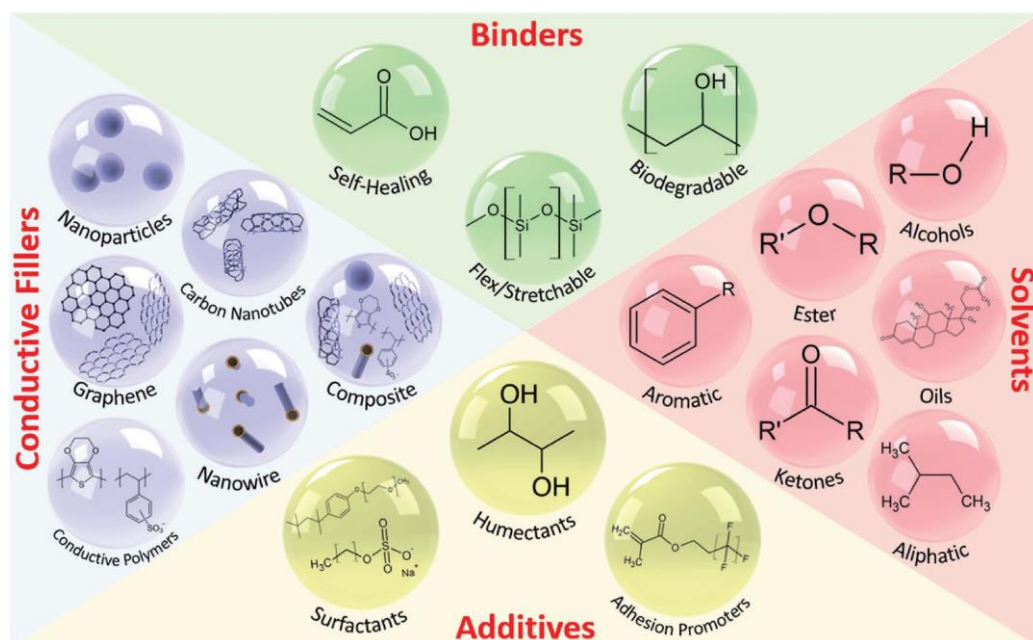


**Figure 5:** List of chemical components of the ink used in SPE production [14].

## 1.2.2 Voltammetry techniques

The reduction in the cost of electronics in the last couple of decades has engendered an expansion in the use of electrochemical measurements. This has led to the creation of many different pieces of equipment dedicated to the measurement of a large variety of electrochemical experiments which relies on the characterization of an electrode's potential [19]. In this chapter, we will discuss a variety of techniques used for the measurements and characterization of said potential.

### 1.2.2.1 Fundamentals

Every electrochemical reaction starts in a thermodynamic equivalency that characterizes a zero-current state in which both anodic and cathodic currents equate each other. The application of any given potential through an electrode to shift this potential (if it is lower, then it shift toward the cathodic;

if it is higher, it shift toward the anodic) allows the study of the kinetics behavior through said electrode in the presence of one or several electroactive species.

And the specific way this behavior, also known as the electrode potential, is studied gives rise to more than 20 electrochemical techniques as mentioned by the International Union of Pure and Applied Chemistry (IUPAC) in 1975. Most of these techniques can be described as the record of a perturbation by an application of potential as shown in figure 6, followed by a relaxation of the electroactive species in the medium, the one used in the experiments will be discussed below.

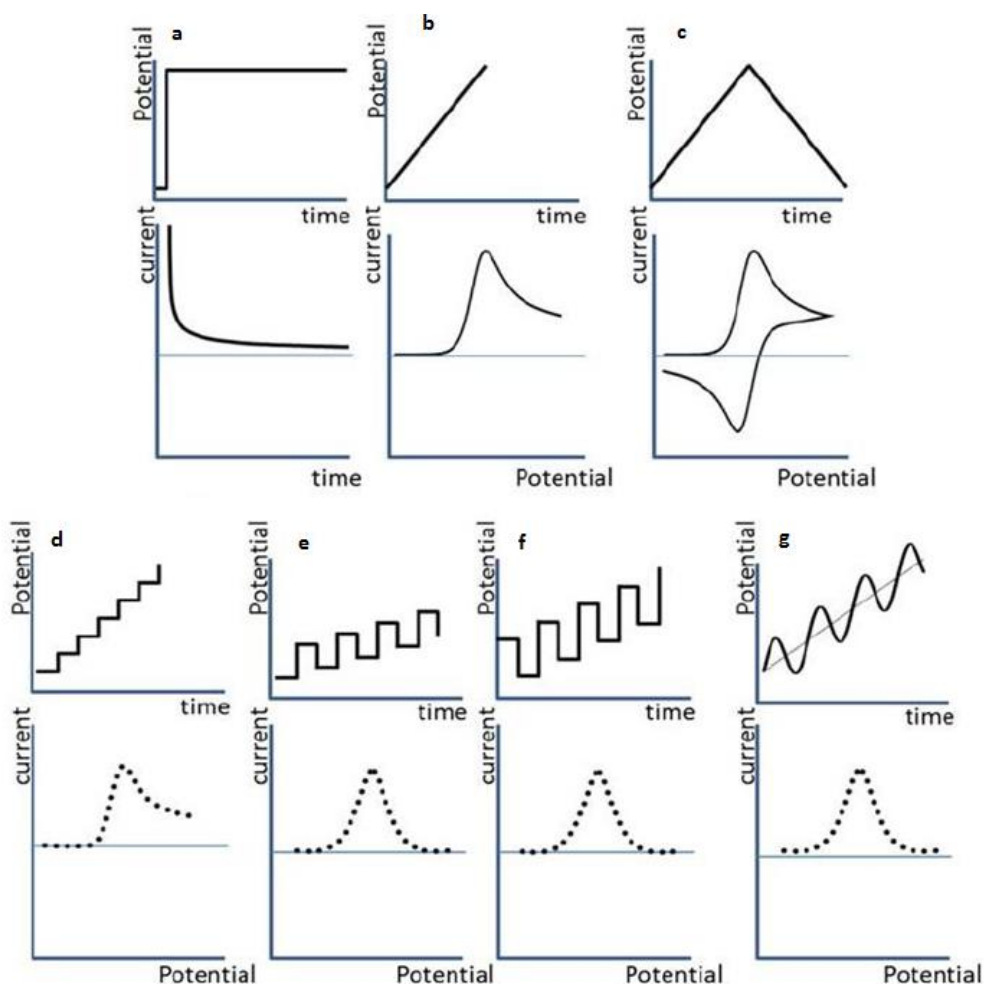


**Figure 6:** Voltammetric methods and their graphic representation showing a) Chronoamperometry, b) Linear sweep voltammetry, c) Cyclic voltammetry, d) Staircase voltammetry, e) differential sweep voltammetry, Square wave voltammetry, AC voltammetry [19].

### 1.2.2.2 Cyclic Voltammetry (CV)

CV also referred to as stationary electrode polarography [11], is considered the second step above CA. They consist of continuously changing the potential as a linear function of time. This technique excels in studying the kinetics of electrochemical reactions, in determining the formal redox potentials of electrodes, and in inducing reversible and irreversible reactions of molecules under study [20]. CV is very similar to another technique called linear sweep voltammetry (LSV) with the main difference between them is that, while LSV is a continuous linear increase of voltage from a hypothetical  $E_0$  to  $E_t$ , the CV experiment reverses the potential between  $E_0$  and  $E_t$  as such making a cycle where the potential starts at  $E_0$  rises to  $E_t$  then falls back to  $E_0$  linearly as depicted in the picture below.

The classical experiment for a CV is usually those that the effects of electromigration of a supporting electrolyte with an inert salt [11].

For a fast and reversible electrochemical reaction of  $\text{Ox} + n\text{e}^- \leftrightarrow \text{Red}$ , the experiment takes shape as described in figure 7.

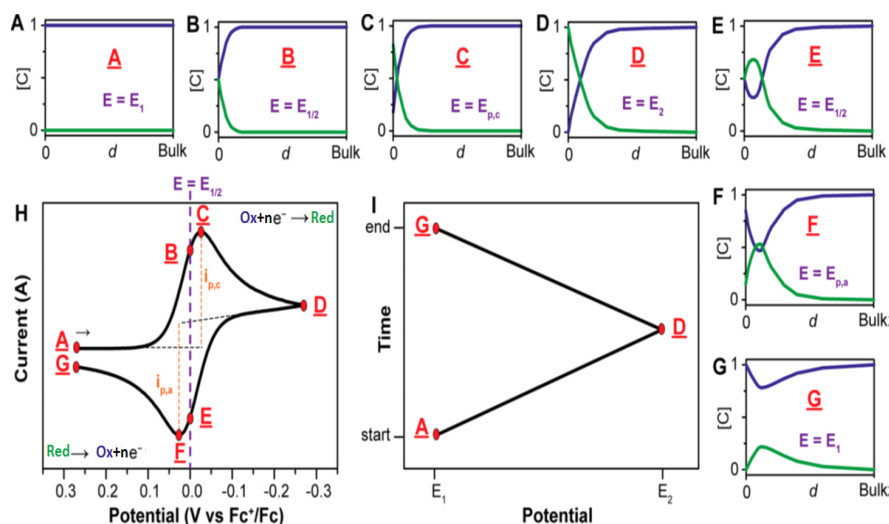


**Figure 7:** A typical CV experiment showing: from A to G the concentration profile of the electrode, H the cyclo-voltammogram, and I the applied potential in relation to time [21].

The potential of the reaction dictates the concentration of the Ox Red species on the surface of the electrode through Nernst equation 1.1

$$E = E^0 + \frac{RT}{nF} \ln \frac{[\text{Ox}]}{[\text{Red}]} \quad (1.1)$$

Here, we have  $E^0$  is the formal potential of the given species,  $E$  is the applied potential at any given time,  $R$  is the universal gas constant,  $T$  is the temperature,  $n$  is the number of electrons transferred,  $F$  is the faradaic constant,  $[\text{Ox}]$  and  $[\text{Red}]$  are the concentrations of the oxidized and reduced analyte. Following the Nernst equation, we find that  $E_{1/2}$ , or when the oxidized and reduced analyte are in equal concentrations, is equal to  $E^0$ , as such,  $E_{1/2}$  is dependent on the species of the analyte being studied.

While Nernst is useful to study the concentrations in relation to the potential, the intensity of the peaks follows the Randles-Sevcik equation 1.2.

$$i_p = (2.69 \times 10^5) n^{3/2} A C D^{1/2} v^{1/2} \quad (1.2)$$

In this case, the value  $i_p$  is the peak's intensity value in amperes,  $n$  is the number of electrons transferred from the electrode to the medium,  $A$  is the electrode's electroactive area in  $\text{cm}^2$ ,  $C$  is the bulk solution concentration in  $\text{mol/L}$ .  $D$  is the analyte diffusion coefficient in  $\text{cm}^2/\text{s}$ , and  $v$  is the scan rate in  $\text{V/s}$ .

Unfortunately, the measurement of peak current in CV is imprecise because the correction for charging current is typically uncertain, and this issue is amplified by the reversed peak. As such, CV is not used for qualitative measurements. However, CV's power lies in its diagnostic strength, stemming from the ease of qualitative and semi qualitative interpretation [21].

### **1.2.3 Surface Modification**

The majority of common, standard techniques for trace-level detection of analytes use large-scale equipment based in the laboratory such as spectrometry, which, despite their reliability and sensitivity, have some disadvantages, including high price, their time-consuming and laborious operation. Therefore, developing an accurate, fast, simple method for the routine methods for analyte detection in samples is required. As such, Electrochemical methods that utilize chemically modified electrodes are surfacing as alternatives to spectroscopic methods [22].

The history of deliberately modifying starts in the 1970s when the first reports came describing electrode modification with covalently bonded functional groups, polymer films, adsorbed molecules, and other non-liquid depositions [23].

For this thesis, we would like to discuss the main techniques used to modify the electrode's surface.

#### **1.2.3.1 Methods for electrode modifications**

Several modes of electrode modifications have been developed; however, they fall under two umbrellas, physical and chemical.

Physical modifications rely on physical interactions to change the electrode surface. Physical adsorption allows the deposition of bioreceptors through electrostatic interactions, it is the simplest method for deposition, however, it also lacks reproducibility and has low sensibility. Another physical method is entrapment of the bioreceptors in a polymer, or a 3D gel, however, this technique doesn't work for small molecule bioreceptors as they can just escape the matrix that is made to house them.

Because of the problems mentioned above, chemical modifications rely on creating a covalent bond between the surface of the electrode, and the bioreceptor is much more attractive. These modifications can be done with

any type of electrode made from common materials and include the formation of a self-assembled monolayer of thiol groups on gold, silanization, and aryl group formation.

All of these techniques allow the addition of a carboxyl or related group on the surface of the electrode thus allowing its functionalization through chemical bonding reactions [24].

### 1.2.3.2 Diazonium activation

Diazonium salts are the term used to describe two nitrogen atoms that are attached to each by a triple bond, also known as an aryl group, and further attached to an organic group, often a ring, subsequently, the groups attached on that ring can be changed to suit the necessary specifications of the functionalization process the process is described in figure 8.

The way Diazonium modification works, when the aryl group is reduced through electrochemical methods, it creates a radical that is covalently bonded onto the surface of the electrode. This creates a duality, while this property means that diazonium cannot be used on something that isn't conductive, it also means that a special selectivity is an option when modifying an electrode [25].

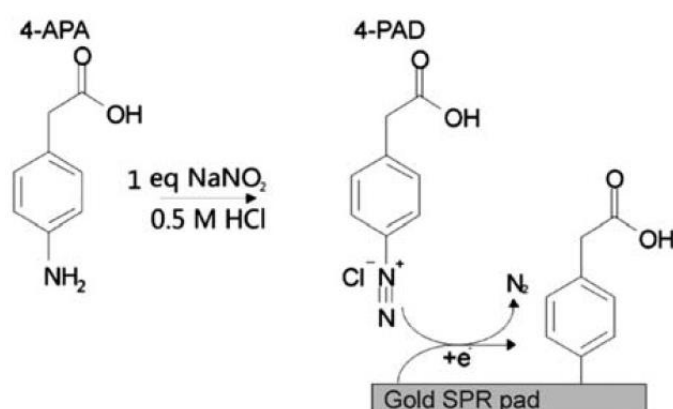


**Figure 8:** Example of diazonium deposition [26].

### 1.2.3.2.1 Advantages of using diazonium salt

Diazonium salt provides several advantages to other modification techniques, first, they provide excellent anti-fouling agents due to their zwitterion properties that make them electrically neutral, as seen in figure 9, which in turn decrease the non-specific attraction the electrode's surface has with interference molecule that hinders the recognition of the target analyte. Also, they form a uniform layer on the electrode's surface which enhances the immobilization of bioreceptor, as such, enhances the detection of target molecules [26].

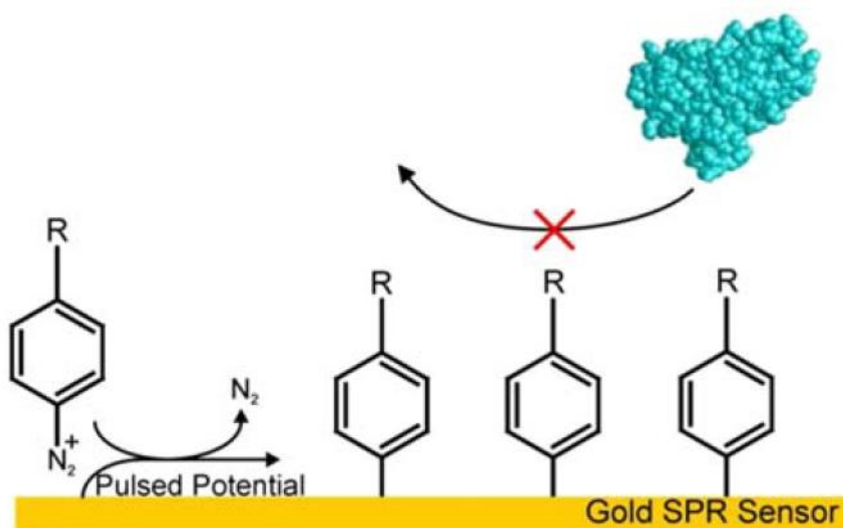


**Figure 9:** Example of the anti-fouling property of diazonium deposition [26].

### 1.2.3.2.2 Functionalization of diazonium salt

Aryl diazonium groups are often accompanied by a large choice of the terminal group R, which allows the salts to serve as coupling agents to attach bioreceptors on the electrode's surface, providing unique strategies to sensor development. The most common terminal group R is the functional group  $-COOH$ ; its charged nature makes the formation of chelating bonds with metals or other charged molecules easier, while also possessing compatibility with esters coupling agents such as 1-ethyl-3-(3-(dimethylamino)propyl)carbodiimide hydrochloride (EDC)/N-

hydroxysuccinimide (NHS) which forms stable -CO-NH- bonds with the biorecognition molecules, the mechanism of which is described in figure 10 [25].

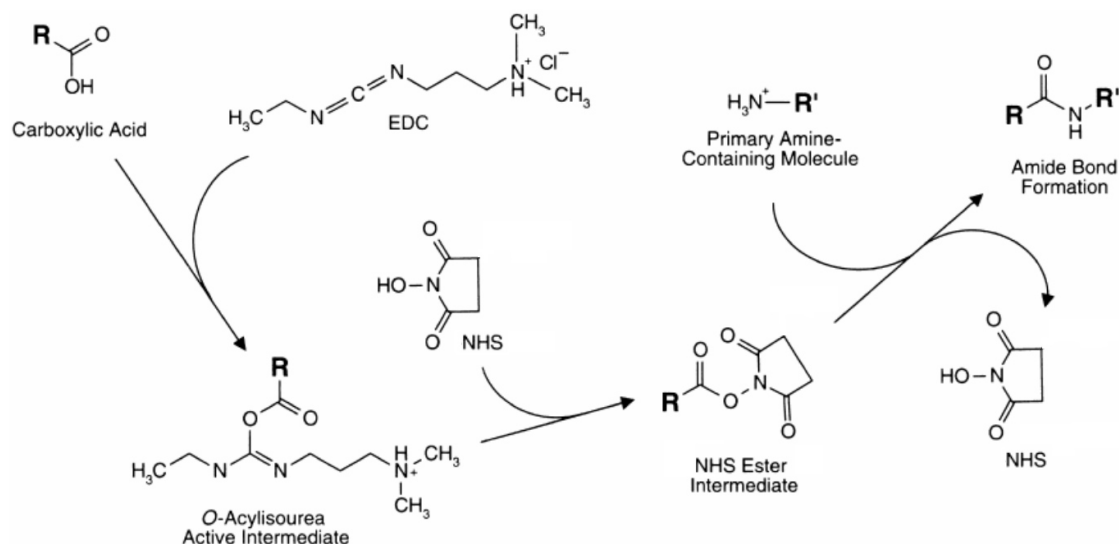


**Figure 10:** EDC/NHS amide formation reaction mechanism [27].

### 1.2.4 Electrochemical Impedance Spectroscopy

To understand EIS, one must understand two key concepts in electrochemistry: the faradaic process involves the charge transfer between the electrode and the oxidized species, while the non-faradaic process involves the accumulation of charge between the interface of said system. EIS is a reliable tool for the measurements of both processes [28].

EIS is capable of doing such measurements because it estimates the transfer function between current and potential. EIS measurements consist of subjecting an electrochemical interface to a small (ideally infinitesimal) sinusoidal voltage (potentiostatic mode) or current (galvanostatic mode) perturbations for a known frequency range while recording concomitantly the resulting sinusoidal current or voltage response. And this response can be shown in a multitude of functions from voltage to current amplitude ratio, phase lag, and complex value function  $Z(f)$  all of which are dependent on the

frequency perturbations. It should be noted that three conditions are necessary if EIS measurements are to be relevant, and they are stability, linearity, and causality [29].

EIS data interpretation relies commonly on the construction of an equivalent circuit model. This is done by, first, regarding the electrochemical system as a series of basic electrical components such as resistance (R), capacitance (C), and constant-phase elements (CPE), and Warburg element (W) linked together in series or parallel; these electrochemical systems are often distributed in space, as such, these individual elements are the result of rigorous physical principles that are calculated after solving physics-based boundary value problem. By building the equivalent circuit, the value of each component can then be measured and the specifics of the electrochemical system can then be deduced, as such, choosing the equivalent circuit model is an important step that determines the accuracy of the interpretation of the entire analysis. Herein lies the problem, the most common method of choosing a suitable equivalent circuit model is by screening potential models given to different applications then fitting them mathematically to generate corresponding patterns, while this can be automated such as the case for genetics and gene expression programming, the mere act of developing an analog represents an incomplete analysis of data [29,30].

#### 1.2.4.1 Basic calculations

According to Ohm's law, a resistance  $U$  subjected to a potential  $E$  then affects the current  $i$  using equation 1.3.

$$E=Ui \quad (1.3)$$

This equation is used to determine the current of a known voltage in a circuit or the voltage of a current flowing through the resistance. The equation also proves no lagging between the current and the potential while

retaining its sign (positive if it flows from positive to negative and negative if it flows in the other direction) [31].

Impedance is a more general concept than the one described in Ohm's law since it also incorporates phase differences into its equation. This is the case for a monochromatic signal that follows equation 1.4.

$$v(t)=V_{\text{peak}} \sin(\omega t) \quad (1.4)$$

Here, the voltage at any given time  $v(t)$  is written in the form of a sinusoidal function of the angular frequency multiplied by time  $\sin(\omega t)$  multiplied by the peak voltage  $V_{\text{peak}}$ . The frequency of such a signal is given in 1.5.

$$f=\frac{\omega}{2\pi} \quad (1.5)$$

When applied to a circuit, such potential yields the current seen in 1.6.

$$i(t)=I_{\text{peak}} \sin(\omega t+\theta) \quad (1.6)$$

The most notable inclusion is the phase difference  $\theta$  between the current and the potential. In purely resistive currents this phase difference is zero.

As such, through Laplace and Fourier transformations, any electrical component  $Z$  can then be expressed into a planar vector with a right-hand orthogonal system of axes, which with a magnitude equal to the sum of the components  $a$  and  $b$  along the axes, as in, it can be expressed as a complex number  $Z=a+jb$  with  $j=\sqrt{-1}=e^{j\frac{\pi}{2}}$  meaning that the vector goes in an anticlockwise rotation in relation to the x-axis. Now since the equation is a representation of a right-handed orthogonal axe, the real part  $a$  becomes in the direction of the x-axis and the imaginary part  $b$  becomes in the direction of the y-axis. As such, figure 11 becomes a valid interpretation for the EIS spectrum.

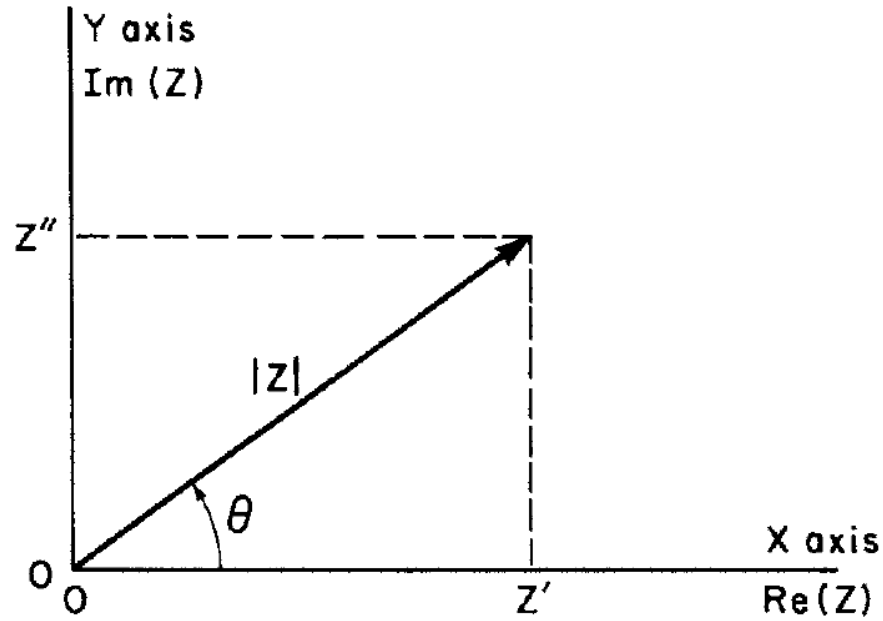


**Figure 11:** Representation of an impedimetric vector, also called an angram diagram, with its real and imaginary components in relation to the phase shift  $\theta$  [32].

With the above vector translating into  $Z=Z'+jZ''$  and its resolution is found in equation 1.7.

$$\begin{aligned}
 Z' &= Z_{\text{re}} = |Z| \cos \theta \\
 Z'' &= Z_{\text{im}} = |Z| \sin \theta \\
 \theta &= \tan^{-1} \frac{Z''}{Z'} \\
 |Z| &= \sqrt{Z'^2 + Z''^2}
 \end{aligned} \tag{1.7}$$

As these equations indicate,  $Z$  is frequency-dependent. As such, plotting  $Z$  vs  $\omega$  is one of the most common methods of deriving information regarding a system. However, for nonlinear systems such as those found in electrochemistry, these plots provide meaningful insights into the system only for signals whose magnitude where the overall electrode-material system is electrically linear; this is usually achieved if  $V_{\text{peak}}$  is less than the thermal voltage of the system which is defined in equation 1.8.

$$V_T = \frac{RT}{F} = \frac{kT}{e} \quad (1.8)$$

In 1.8,  $V_T$  is the thermal voltage,  $T$  is the temperature in kelvin,  $R$  is the gas constant,  $F$  is the faradaic constant,  $k$  is the Boltzmann constant, and  $e$  is the electron charge. This leads to the thermal voltage being 25 mV for a temperature of 25°C [32].

#### **1.2.4.2 Graphical presentation and interpretations of EIS.**

There are a couple of ways EIS produces results, either as real  $Z'$  and imaginary  $Z''$  impedances or as modulus  $|Z|$  and phase angle  $\theta$  as functions of frequency. These representations are known respectively as Nyquist plot (Also referred to as complex plane plot since Nyquist plots often refer to stability plots as well) and Bode plot (Bode plot is usually divided into two separate plots, the impedance Bode plot where  $\log|Z|$  is plotted against  $\log(f)$ , and phase shift bode where the phase angle  $\theta$  is plotted against  $\log(f)$ ), and the graphical inspection of these plots usually makes it possible to identify the electrical equivalent circuit. The equivalent circuit model is then used to model the data to obtain a numerical value for the system. In an experimental setting, it is strongly recommended that both plots be used, while Nyquist plot provides a lot of information regarding a system, it lacks any information regarding the frequencies, as such, most modern programs that perform EIS fitting automatically shows either both the Nyquist and the bode plots or a tridimensional Nyquist plot with the frequency being in the third axis as seen in figure 12.

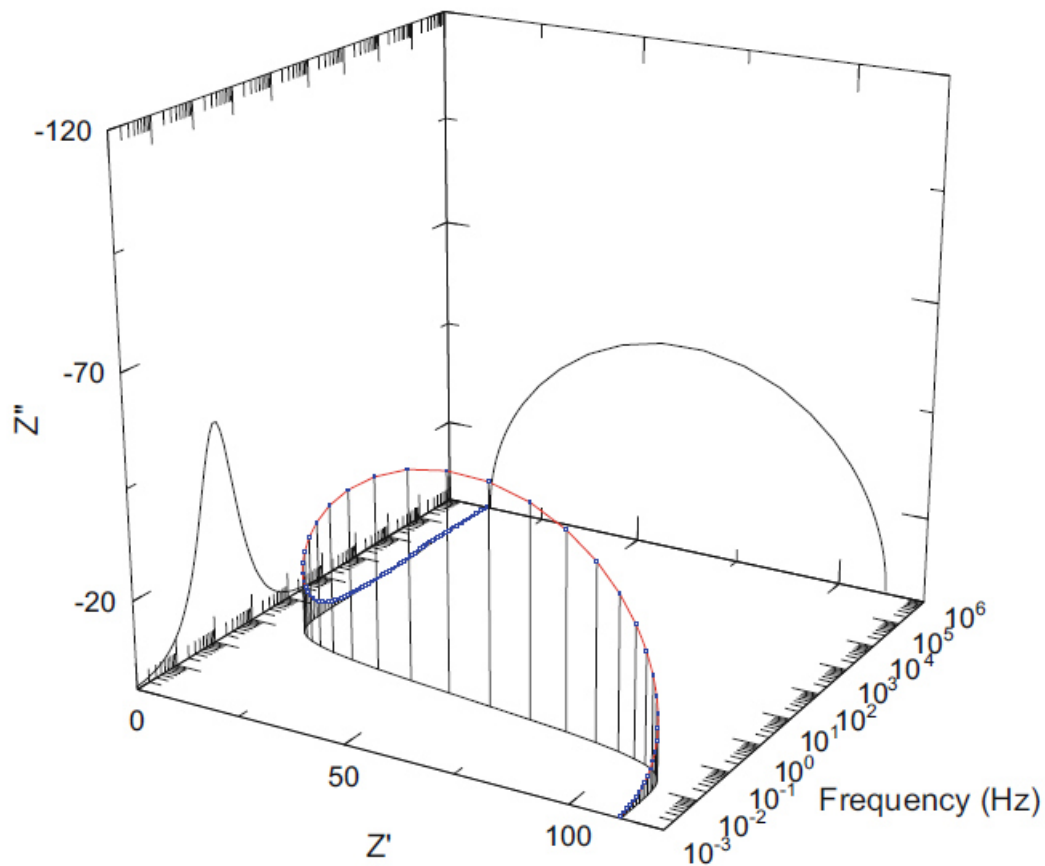


**Figure 12:** Example of tridimensional impedance plot (in  $\Omega$ ), generated by ZView [31].

It should be noted that in all the cases that follow,  $Z''$  is always negative.

The biggest issue is then faced in finding out a physically meaningful equivalent circuit that can explain the processes involved in the system. This is usually done by counting the number of semi-circles in an EIS Nyquist plot, through the present literature, and through guessing from basic knowledge of the system. However, these methods lack the rigorousness necessary for characterizing any system with multiple processes that are close to each other. As such, graphical analysis of both Nyquist and Bode are a necessity for meaningful use of EIS [33].

### 1.2.4.2.1 Faradaic process in EIS

For planar electrode, Randle circuit is the most common circuit found in electrochemistry used to describe the faradaic processes of a reversible electrochemical reaction of a system; it is written as  $R_s(C_{dl}(R_{ct}Z_w))$ , where the solution resistance is called  $R_s$ , the charge transfer resistance is called  $R_{ct}$ , the double layer capacitance is called  $C_{dl}$ , and the Warburg diffusion element is called  $Z_w$ . Randle circuit covers all the necessary functions of a simple

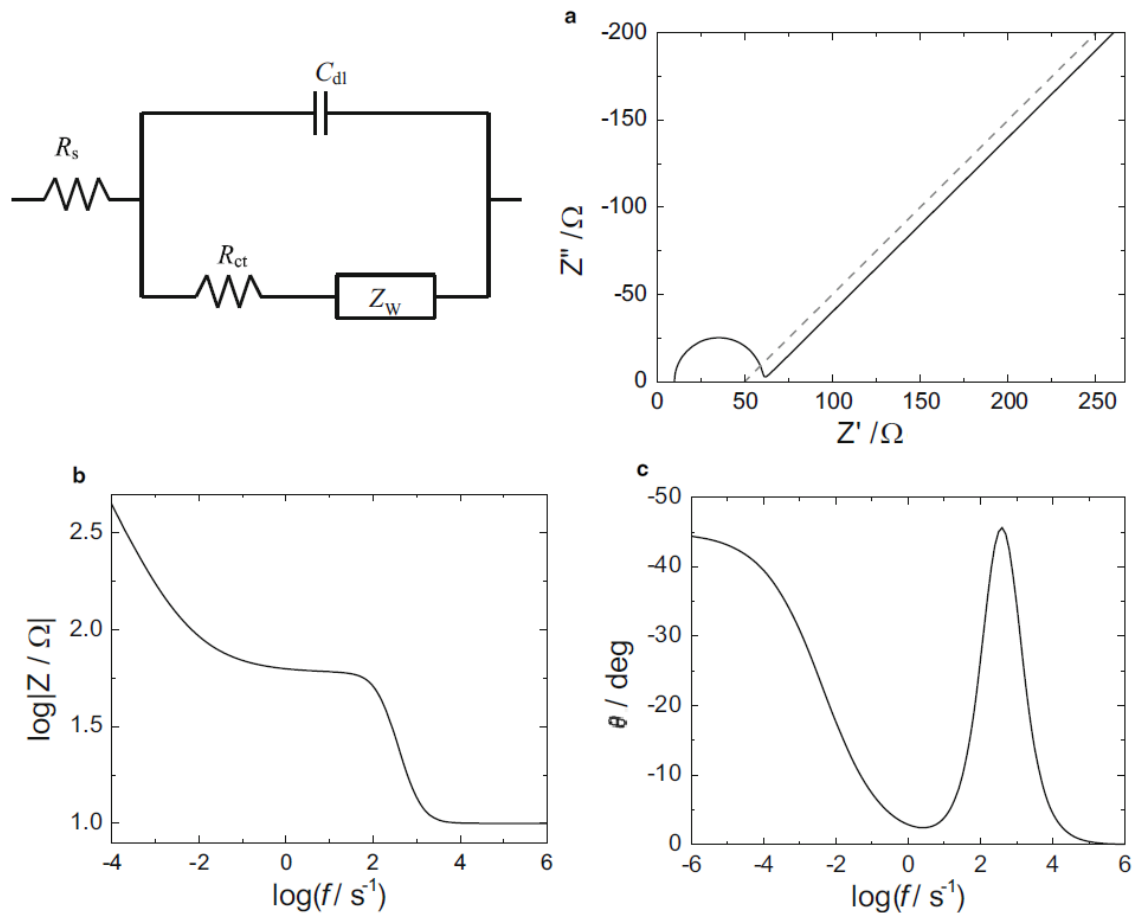


**Figure 13:** Randle circuit and its impedance spectrum with a) Nyquist plot, b) Impedance Bode plot and c) phase angle Bode plot [31].

Randle is governed by the equation 1.9.

$$Z = R_s \frac{1}{j\omega C_{dl} + \frac{1}{R_{ct} + Z_w}} \quad (1.9)$$

The Nyquist plot corresponding to this equation is a semicircle which is the result of the pairing of  $R_{ct}$  and  $C_{dl}$ ; the semicircle starts at  $R_s$  and ends at  $R_s + R_{ct}$  on  $Z'$  this semicircle then ends with the diffusion element also known as  $Z_w$ , which will be talked about later, is shown in figure 13 as a dotted line.  $R_{ct}$  is related to the concentrations of the oxidant and reducer species at the electrode's surface as well as the electrode's potential under equation 1.10.

$$R_{ct} = \frac{RT}{n^2 F^2} \frac{1}{\alpha k_{ox} C_{o(0)} + (1-\alpha) k_{red} C_{r(0)}} = \frac{RT}{n^2 F^2 k^0 C_o} \frac{1 + e^{\left[ \frac{nF}{RT} (E - E_{1/2}) \right]}}{\xi^\alpha e^{\left[ (1-\alpha) \frac{nF}{RT} (E - E_{1/2}) \right]}} \quad (1.10)$$

In equation 1.10,  $\alpha$  is the transfer coefficient,  $k_{ox}$  and  $k_{red}$  are the heterogeneous rate constants of the oxidation reaction and the reduction reaction respectively.  $R$  is the gas constant,  $T$  is the temperature,  $n$  is the number of electrons,  $F$  is the faradaic constant, and  $C_{o(0)}$  and  $C_{r(0)}$  are the concentrations of the oxidant and reducer on the electrode's surface,  $k_0$  is the heterogeneous rate constant at the standard potential (cm/s),  $C_o$  is the bulk concentration of the oxidant,  $f = RT/F$ ,  $\alpha$  is the transfer coefficient,  $E$  is the applied potential,  $E_{1/2}$  is the reversible half-wave potential which is also expressed as:  $E_{1/2} = E^{0'} + \frac{RT}{nF} \ln \sqrt{\frac{D_R}{D_o}}$  with  $E^{0'}$  is the standard wave potential, and  $D_o$  and  $D_r$  are the diffusion coefficient of the oxidant and reducer respectively which, when combined can then be written as such:  $\xi = \sqrt{\frac{D_o}{D_r}}$ .

Bode Impedance plot starts with  $R_s$  at the high frequencies, then becomes  $R_s + R_{ct}$  at the medium frequencies before finishing as a  $45^\circ$  line at the low frequencies which represents  $Z_w$ . The phase degree Bode plot follows a similar trend where it displays a peak at the frequencies where the semicircle of the Nyquist plot is supposed to be, before heading as a  $45^\circ$  line at the low frequencies like the Bode impedance plot [31].

#### **1.2.4.2.2 Porous Electrode Impedance**

Porous electrodes are usually used in industrial applications where a large surface area is needed. Porous electrodes are different from the rough surface electrode with a depth  $l$  and a diameter  $r$ , in that it also has a ratio  $l/r$  which characterizes its porosity.

For a faradaic impedance, the electrode is displayed in Nyquist plots as two semicircles that changes shape depending on the concentrations of the active species (The higher the concentration, the sharper the semicircles become), the electrode's potential (it tends to 2 semicircles the more negative the potential is applied), and its porosity (too much porosity or too little porosity will yield a single semicircle, a proportional amount of porosity is required for two semicircles), all of which affects the shape and sharpness of the semicircles. Example of which can be found in figure 14.

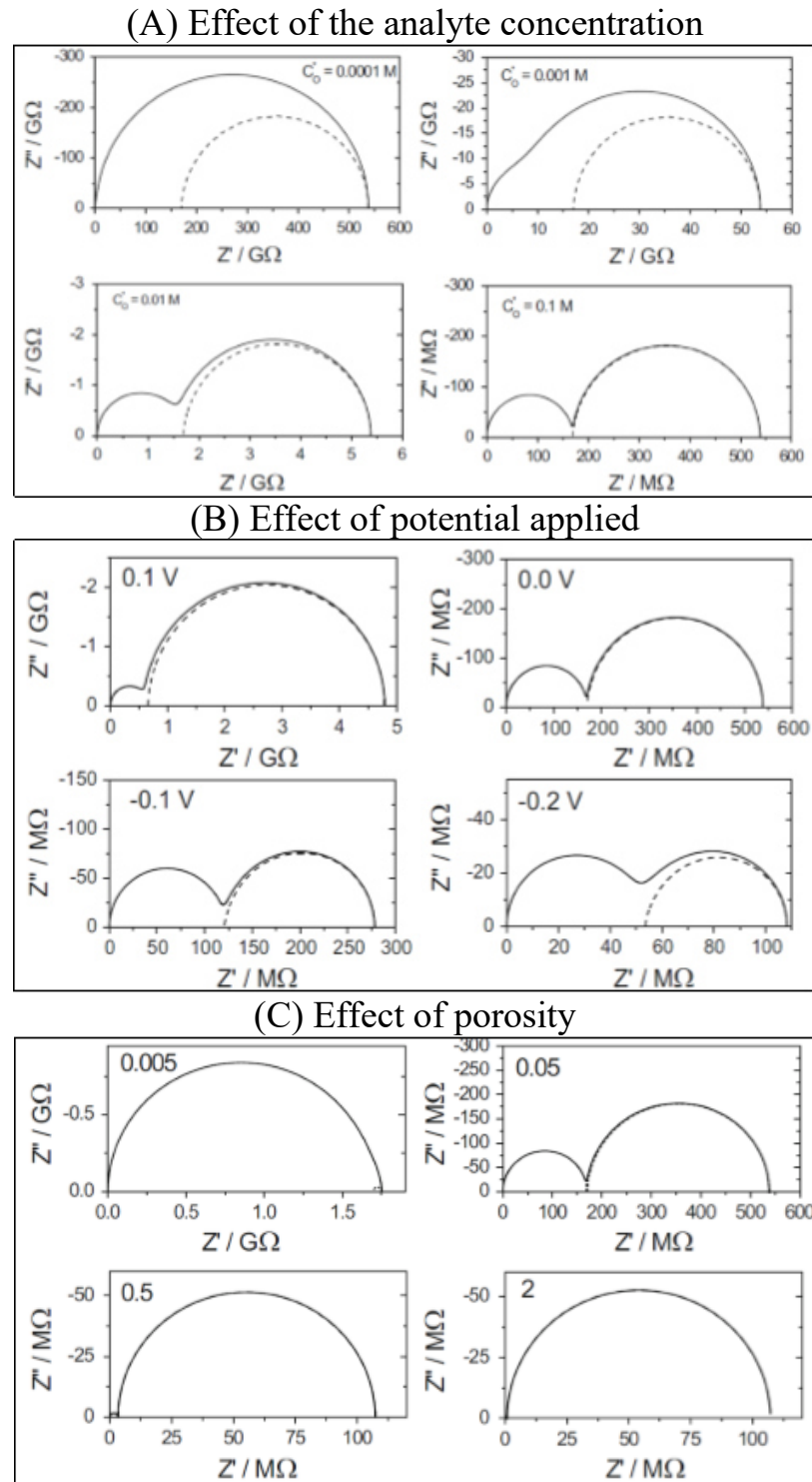


**Figure 14:** Effect of the analyte concentration (A), potential applied (B) and porosity (C) on the shape of the Nyquist plot of a given electrode's surface [31].

As such, porous electrodes are treated with an equivalent circuit  $R_s(C_1R_1)(C_2R_2)$  which follow the equation 1.11.

$$Z = R_s + \frac{1}{\frac{1}{R_1} + j\omega C_1} + \frac{1}{\frac{1}{R_2} + j\omega C_2} \quad (1.11)$$

For simplification,  $\tau$  is used to describe the RC pairs, the value of  $\tau = RC$  and is measured in s. This yields the following EIs plots:

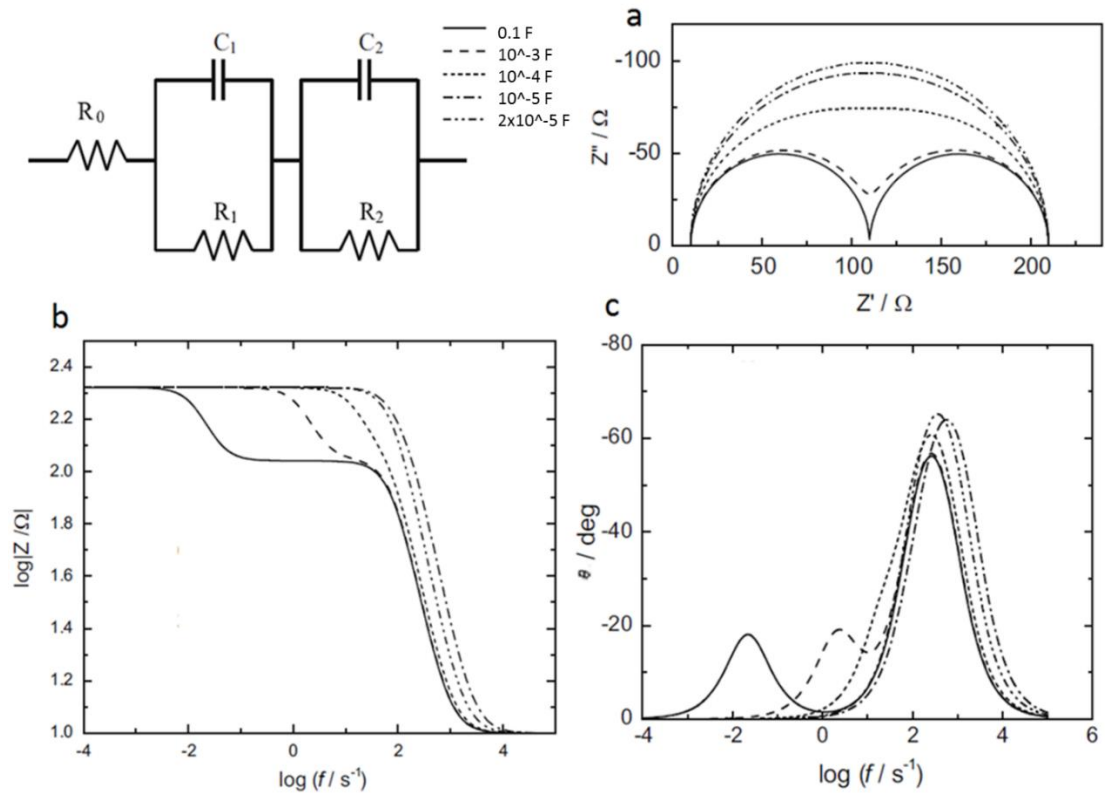


**Figure 15:** The modelization of two semicircle circuit's impedance spectra with a) Nyquist plot, b) Impedance Bode plot and c) phase angle Bode plot showing  $R_0 = 10 \Omega$ ,  $R_1 = R_2 = 100 \Omega$ ,  $C_1 = 20 \mu\text{F}$  with varying  $C_2$  ( $0.1, 10^{-3}, 10^{-4}, 2 \times 10^{-5},$  and  $10^{-5}$ ) which are represent [31].

From figure 15, the first observation that can be made is that the smaller one of the double layer capacitance is to the other, the less sharpness we have for the peaks. For the Nyquist plot, the semicircles merge when the difference is sufficiently large. While in Bode Impedance plot, the less the difference is, the more we can distinguish two steps as the frequencies become lower: at the high frequencies, the impedance starts at  $R_0$ , then, when the frequency is decreased, we obtain the first step which is equal to  $R_0 + R_1$ ,

the as the frequency heads toward the lower frequencies, we obtain the value of  $R_0 + R_1 + R_2$ . At the phase angle Bode plot, however, at equal capacitance, the peaks are merged into one, but, as the difference between the parameters increases, the second peak starts to move toward the lower frequencies and it becomes more separate from the original peak [31].

#### 1.2.4.2.1 Warburg element

Warburg impedance is an element that represents the diffusion of the electroactive species in the solution, it cannot be represented as a simple function such as a resistance or a capacitance as it doesn't behave as such.  $Z_W$  is always at  $-45^\circ$  angle to  $Z'$ . It follows the equation 1.12.

$$Z_W = Z_{w_o} + Z_{w_r} = \frac{\sigma'}{\sqrt{j\omega}} = \frac{\sqrt{2}}{\sqrt{j}} \frac{\sigma}{\sqrt{\omega}} = \frac{\sigma}{\sqrt{\omega}} (1-j) \quad (1.12)$$

In the above equation,  $Z_{w_o}$  and  $Z_{w_r}$  are the specific impedances of the oxidant and reducer species in the bulk solution,  $j$  is the imaginary number and  $\omega$  is the radial frequency,  $\sigma'$  and  $\sigma$  are the mass transfer coefficients which are equal to the sum of the contribution of the oxidant and reducer species and they are also governed by the equations 1.13.

$$\sigma' = \sqrt{2}\sigma = \sigma'_o + \sigma'_r = \frac{RT}{n^2F^2} \left[ \frac{1}{\sqrt{D_o}C_{O(0)}} + \frac{1}{\sqrt{D_r}C_{R(0)}} \right] \quad (1.13)$$

Where  $\sigma'_o$  and  $\sigma'_r$  are the specific mass transfer coefficients for each of the oxidant and reducer,  $R$  is the gas constant,  $T$  is the temperature,  $n$  is the number of electrons,  $F$  is the faradaic constant,  $D_o$  and  $D_r$  is the diffusion coefficient of the oxidant and reducer respectively, and  $C_{o(0)}$  and  $C_{r(0)}$  are the concentrations of the oxidant and reducer on the electrode's surface [34].

#### 1.2.4.2.4 Constant Phase Element (CPE)

In electrochemistry, a well-known phenomenon that affects EIS measurement is frequency dispersion. This phenomenon is mainly due to surface heterogeneity, the coupling of faradaic properties and double layer charging current, non-specific anion adsorption, and even geometry induced current and potential distribution. As such, CPE is used in the analysis. CPE is a fractional element that describes the double layer capacitance while taking into account the above-mentioned behavior. CPE impedance is usually written as equation 1.14.

$$Z_{\text{CPE}} = \frac{1}{Q(j\omega)^\eta} \quad (1.14)$$

Q here refers to CPE's coefficient expressed in  $\text{s}^\eta \Omega^{-1}$  and the coefficient depends on  $\eta$  which is its exponent [33].

It is worth noting that, while some references claim that the CPE exponent is affected by the electrode's roughness [33], other research deny such observations [35].

What is certain is that CPE has a profound effect on the shape of the Nyquist plot [36].

#### 1.2.4.3 Advantages and Disadvantages of using EIS

The main and biggest advantage to using EIS is the wealth of knowledge that the technique provides, EIS is a measurement of a lot of parameters at every frequency, its data can be drawn in a real versus imaginary plot or complex plots that show different variations for each frequency. However, the amount of knowledge that EIS provides is also one of its major limitations as it also generates a lot of ambiguity with the obtained data; analyzing the information provided by EIS without prior knowledge about the complex system is too vague that EIS is only used after more information

is known about a complex electrochemical system when said the system requires fine-tuning [31,32].

Another major issue with EIS is the equivalent circuit. Choosing an equivalent circuit is the most important part of any analysis. But because of the subjectivity of these circuits, many models can correctly interpret the same plot, which makes them inherently unreliable [32]. As such, a thorough graphical analysis is usually proposed to obtain the most compelling model [33], while modeling is being employed to enhance fitting protocol [29], and machine learning is being developed to remove the inherent subjectivity [30].

### 1.3 Breast Cancer

The biggest health challenge in the 21<sup>st</sup> century and the greatest obstacle to extending humanity’s lifespan is cancer. However, even amongst all cancer sites, breast cancer stands out as it affects women disproportionately while at the same time remains the second most frequently diagnosed cancer site in the world as seen in figure 16 [37].

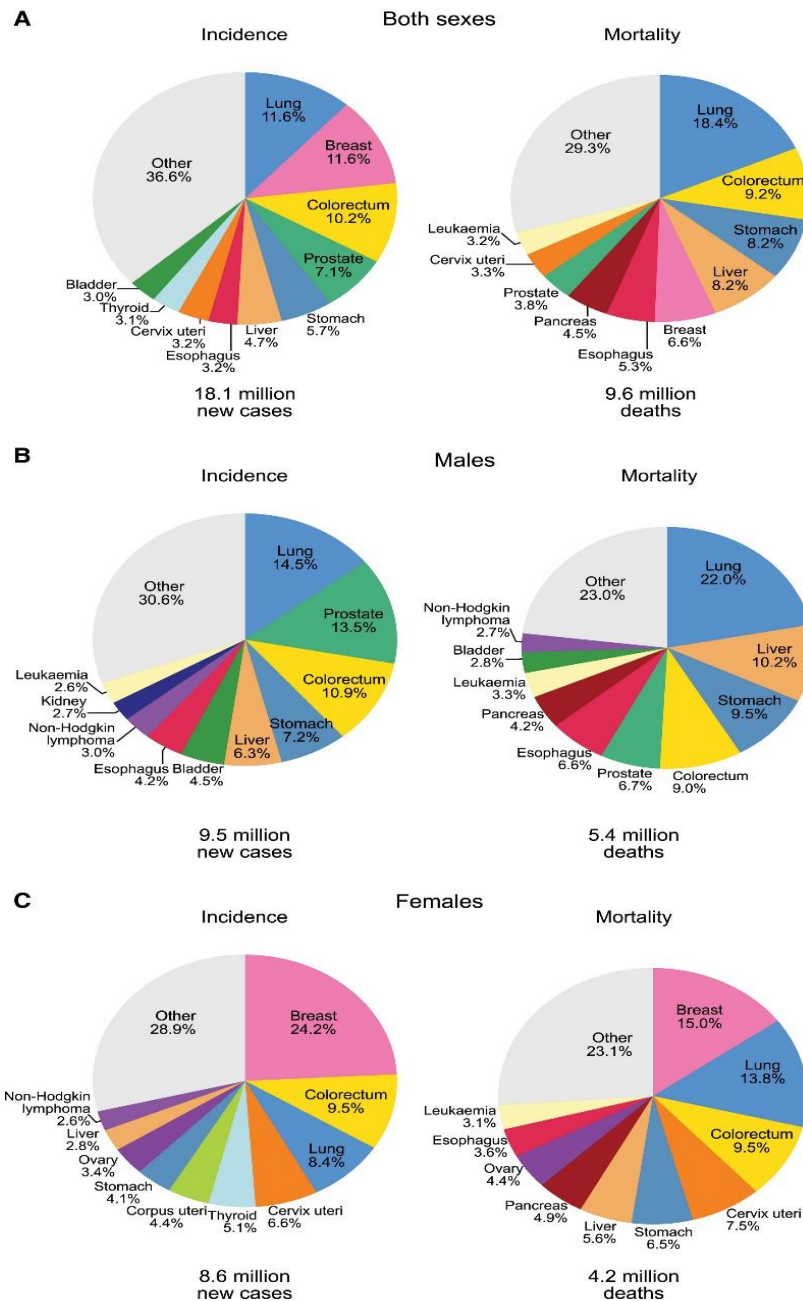


**Figure 16:** Global percentage of incidence and mortality by cancer site for both sexes (A), Males only (B) and female only (C) [37].

This trend is also the case in Lebanon, where the proportion of breast cancer patients is the highest in the region [38]. Not only that, but recent studies also show that this proportion is increasing and is becoming, overtaking even, comparable to those found in western countries [39]. Preliminary genetic screening, however, shows that BRCA1 and 2 account for 15.5% of familial breast cancer [40].

Although we know of breast cancer for more than 3500 years now, it remains a serious health concern now more than ever due to a shift toward a lifestyle that increases its risk factors that are identified by clinicians and epidemiologists such as obesity and lack of exercise, bad diet, drinking, and smoking, all of which causes 70% of breast cancer cases along with hormone replacement therapy and other factors that negatively affect a woman's hormonal balance, while biological factors such as age, family history, early menarche that are usually beyond patient's control contribute to the remaining 30% [41].

One of the main problems with breast cancer is its inherent heterogeneity, possessing a wide variety of morphological and biological features which account for its varied clinical behavior and treatment responses. Traditionally, Breast cancer has been classified by its histological grading, which is the classification of breast cancer by its pathologic growth pattern, tumor cell type, extracellular secretions, and architectural features. However, most breast cancer (70-80%) falls under invasive ductal carcinoma – no special type, which is why this classification fails to account for all of breast cancer's heterogeneity. Classifying breast cancer based on their microscopic features, also known as grading, is a more reliable tool for classifying breast cancer that is commonly used for prognostic purposes a higher-grade breast cancer is more likely to be very different from normal-looking cells. Interestingly, some genetic factors have shown to directly influence and affect the grading of breast cancer [42].

Amongst the traditional classification techniques, molecular classification through immunohistochemical features has been the most reliable. This classification managed to classify breast cancer into five intrinsic subtypes by hierarchical clustering. These classifications are Lumina A, Luminal B, HER2-overexpressed, Basal-like, and normal-like breast cancer.

- Luminal A and Luminal B are characterized by varying levels of estradiol and progesterone receptors on their surface (also called ER and PR), they are similar to other types of epithelial breast cells. Clinically, Luminal A is possible to be treated using hormonal therapy alone, while Luminal B requires additional chemotherapy.
- HER2 overexpression breast cancer is a type of high-grade that has ER- and PR-. They are an aggressive form of breast cancer that is also highly responsive to anti-HER2 therapies.
- Basal-like breast cancer is a type of breast cancer with an overexpression gene found in basal/myoepithelial cells, however, they do not overexpress ER, PR, or HER2 on their surface, thus they are sometimes called triple-negative breast cancer (TNBC).
- Normal like breast cancer is a controversial group that is very similar to normal epithelial breast cells. It can be caused by the contamination of normal breast cells with those of malignant types.

Most of these classifications can be summarized in figure 17.

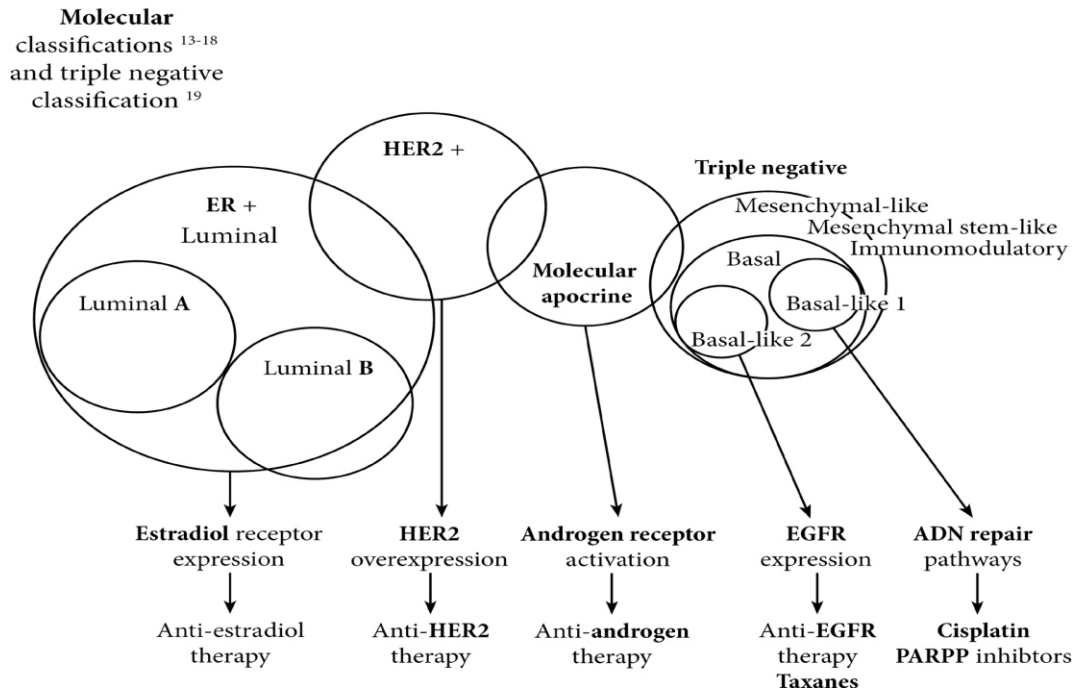


**Figure 17:** The decision tree for breast cancer therapy in regards to Molecular classifications [43].

In recent years, the search for molecules that indicate the presence or provide information about cancers has been increasing in importance to the point where it is mandatory in patients to measure specific biomarkers for their respective malignancy (Duffy 2017 biomarker overview). For breast cancer, a sufficient number of targets have been identified for its diagnosis and prognosis. It is noteworthy to mention MammaPrint and OncotypeDX multigene tests which are commonly used for breast cancer subtype prediction and treatment response [44,45]. The biggest issue with gene testing is poor early detection associated with low concentrations of gene cancer biomarkers. Because of that, protein biomarkers remain the major indicator of breast cancer's presence and behavior [46] with the archetypal biomarkers able to detect small tumors with a high level of selectivity and specificity [4].

Blood plasma is the major source of these protein biomarkers, this is mainly due to its function as a carrier of nutrients and cell debris in the body.

However, blood as a medium for biomarker detection has a few limitations, the lack of understanding of a given cancer's molecular environment while the limited quantity and quality of the said biomarkers makes the necessary steps for discovery and validation inherently hard especially for the limited resources allocated for such endeavor [1].

On the other hand, Saliva is generally viewed as an alternative for blood. Saliva is a readily available body fluid that is secreted in large quantities, it also contains all the necessary biomarkers found in the blood. However, the detection of biomarkers in saliva presents its own challenges. Chiefly among them is the low concentration of said biomarkers that are found in saliva, in addition, the salivary matrix is especially challenging due to its inherently being affected by age, sex, time of day, and even diet [1].

The main protein biomarkers found in saliva for the detection of breast cancer are: Tumor protein 53 (p53), Mucin 1 (MUC1), Human Epithelial receptor 2 (HER2), Epidermal growth factor receptor (EGFR), Carcinoembryonic antigen (CEA), Vascular epidermal growth factor (VEGF) [5].

### **1.3.1 P53**

p53 is the most widely studied tumor suppressor protein to date. Its main canonical function is the regulation of a cell's life and searches for gene damage, p53 is much more multifaceted than previously thought because of its role in regulatory pathways functioning for metabolic homeostasis especially in breast cancer where p53 shows a clear association through the modulation of key proteins in mitochondrial metabolism, cytochrome c oxidase 2 synthesis, and the TP53-induced glycolysis and apoptosis regulator (TIGAR) with clear roles in cellular programming, differentiation, and survival as seen in figure 18 [47,48].

During pregnancy, hormonal activation of p53 pathways at a critical time in mammary development has been linked to long-term negative or positive modifications in the mammary glands, increasing or decreasing breast cancer risk. Also, mounting pieces of evidence were observed that indicate that Estradiol receptors on breast cancer cell surface and p53 are mutually regulated [47].

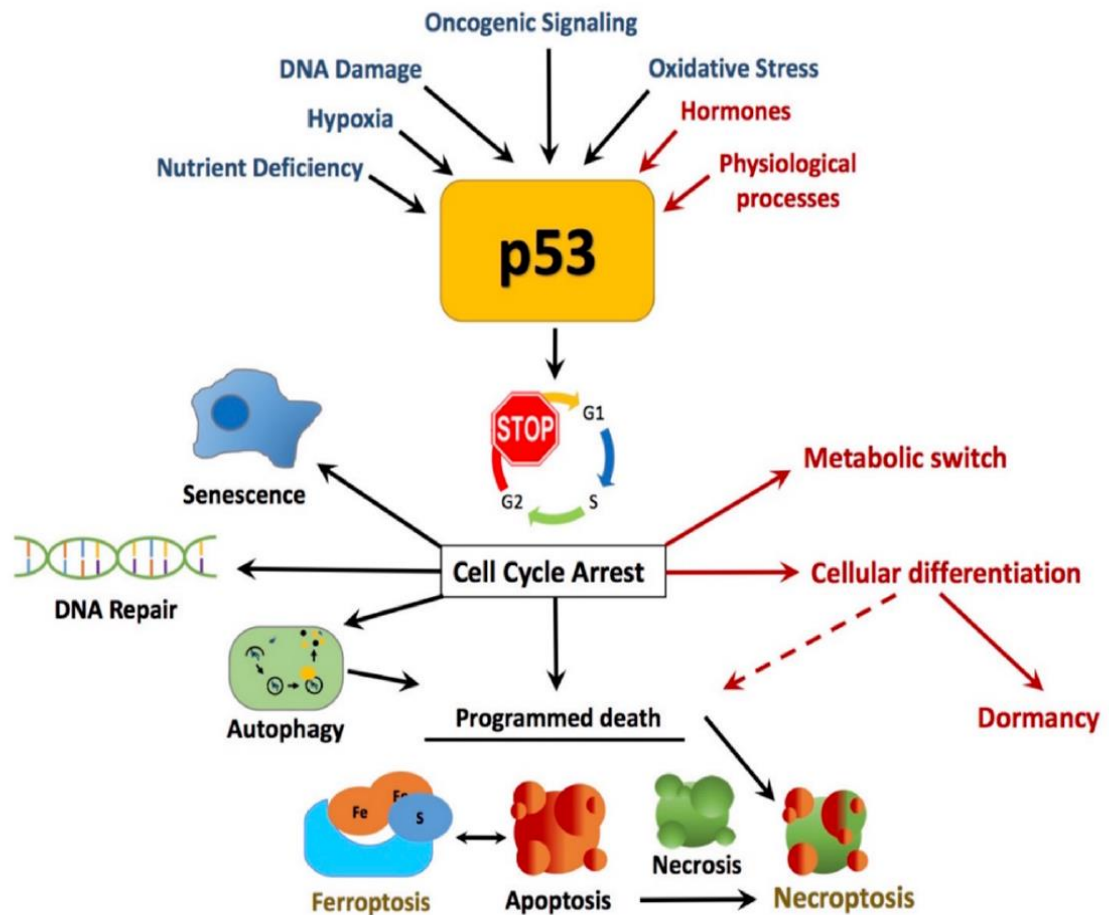


**Figure 18:** Role of p53 in cells [47].

### 1.3.2 MUC1

MUC1, also known as cancer antigen 15-3 (CA15-3) and cancer antigen (CA27.29), is a glycoprotein whose primary function is hydration and protection as it provides to the mucosal and epithelial membrane. During milk production, MUC1 acts both as an emulsifier for lipids and as a decoy against bacterial contamination of the milk. In breast cancer, seventy-eight

isoforms of MUC1 were identified from breast and ovarian cancer cell lines, however, their roles in cancer and other diseases remain a mystery as all but two of the isoforms were shown to inhibit cancer cell growth *in-vivo*. MUC1 is expressed on all epithelial cells except for those in the skin and mesenchymal cells. MUC1 is however overexpressed in malignant cancers. Its function in breast cancer is explored in figure 19. As such, several tests have been developed for its detection for a specific type of cancer such as CA15-3 which detects the epitope DTRPAP using the anti-MUC1 VNTR Mab DF3 antibody, and CA27.29 that uses anti-MUC1 VNTR Mab B27.29 antibody to detect the epitope PDTRPAP. Another test called MSA is developed for the detection of MUC1 carbohydrate moieties that can detect 76% of stages I and II breast cancer and 86% to detect stages III and IV [49].

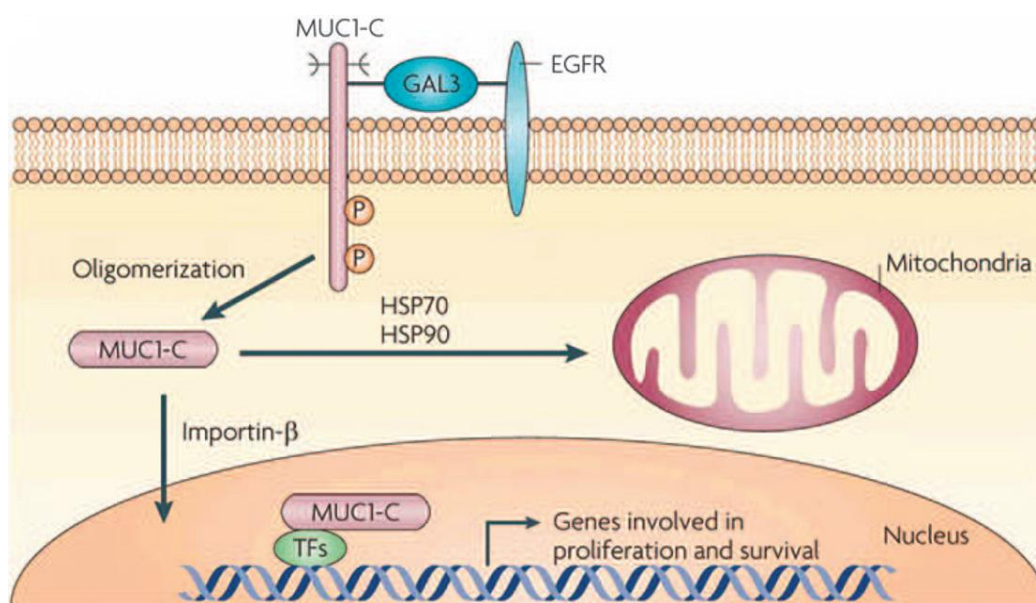


**Figure 19:** activation of MUC1 subunits in cancer cells [50].

### 1.3.3 Human epidermal receptor family

The human epidermal receptor (HER) family is a large and best-known family of protein kinases that have been extensively studied. It has been implicated in functions ranging from cellular proliferation to apoptosis, mobility, and adhesion. The structure of HER family is compromised with 3

main domains: an amino-terminal extracellular domain ranging between 643 to 652 amino acid residues that are further classified into 4 subtypes; a transmembrane domain comprising 10 to 25 hydrophobic amino acid residues; the intracellular domain that holds a kinase subdomain is around 550 amino acids. The HER family receptors are each transcribed from a different chromosome: Chromosome 7 for HER1, Chromosome 17 for HER2, Chromosome 12 for HER3, and Chromosome 2 for HER4 [51,52]. Each of these receptors can form one of 28 homo or heterodimers to combine with different receptors. Until now, more than 600 receptor-ligand complexes have been discovered; it is worth mentioning that HER2 doesn't have a specific ligand rather it acts as an amplifier to other HER monomers [52,53]. Figure 20 shows the different structures for each member of the HER family.

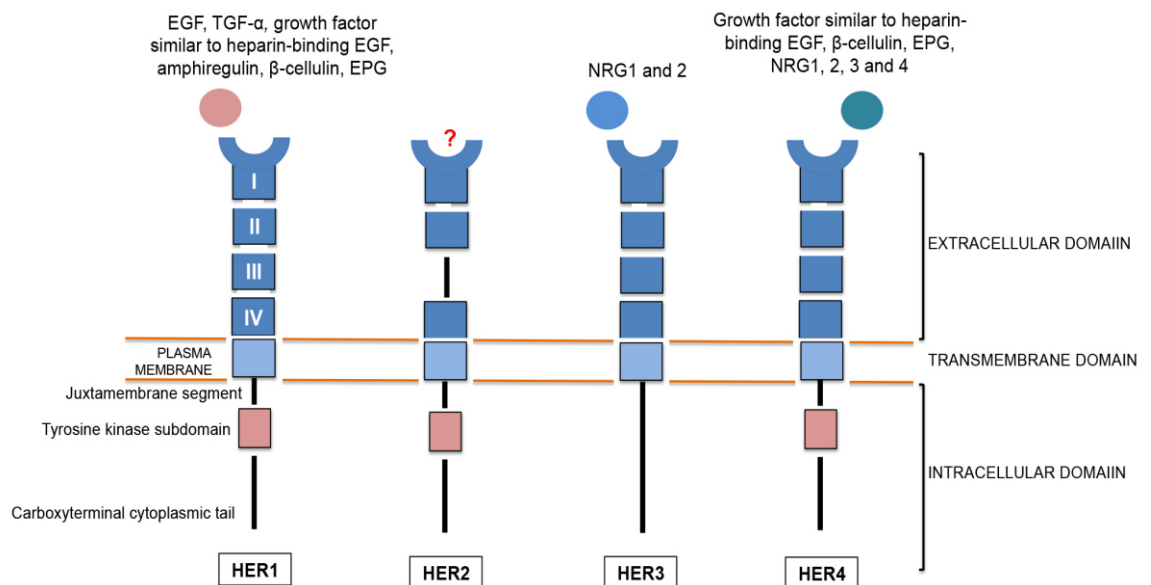


**Figure 20:** Different subtypes of HER family and their respective ligands [52].

In this family, two biomarkers have been recognized for breast cancer, and they are HER1 (Also known as epidermal growth factor receptor (EGFR)) and HER2.

### **1.3.3.1 Epidermal Growth factor receptor**

One of the most influential members of the HER family, EGFR has an important role in the initiation and signaling pathways that infers the behavior of epithelial cells and tumors of epithelial origins. One of the most important ligands of EGFR is the epidermal growth factor of which it is named after, as well as transforming growth factor-alpha ( $TGF\alpha$ ). As mentioned earlier, EGFR can form either homodimer with itself or heterodimers with the other HER family subtypes; this dimerization activates the intracellular kinase region of EGFR which results in auto-phosphorylation of tyrosine amino acids at the C-terminus. This, in turn, will lead to the activation of a signaling cascade with the activation of several signal transducers that are responsible for multiple downstream signaling pathways such as kinases, phosphatases, transcription factors, and adaptor proteins. With such an impressive functional repertory, EGFR and the remaining HER family are prime targets for cancer cell deregulation and gene amplification [51].

### **1.3.3.2 Human Epidermal Receptor 2**

It is one of the most known biomarkers for breast cancer, HER2 left a mark on this particular disease since overexpression of the HER2 gene is often associated with an aggressive disease. HER2 is unique in the HER family in that its extracellular domain is made up of an open conformation, thus, exposing the dimerization loop. This characteristic HER2 structure lacks any known ligand-binding site, while at the same time enables HER2 to form dimers with other HER members. This property is used in breast cancer, as overexpression of HER2 allows it to form dimers, both homo, and heterodimers, in the absence of ligands. Thus, leading to the activation of the downstream signaling pathways associated with cell proliferation and enhancing breast cancer survival. An example of the downstream effects of

HER2 activation is seen in figure 21. It is worth mentioning that, before the development of anti-HER2 therapy, HER2 enriched breast cancer were notoriously difficult to treat. However, the creation of HER2 targeted drug has increased the survival of breast cancer patients considerably [54].

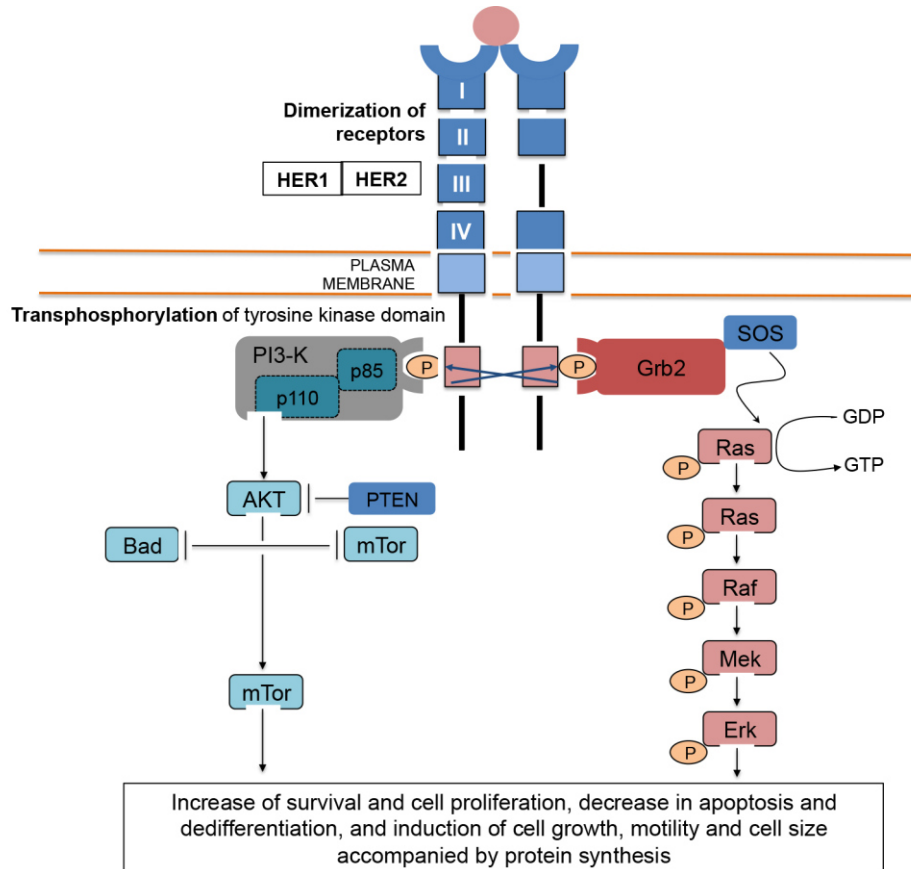


**Figure 21:** Downstream signaling pathways result from the dimerization of EGFR and HER2 [52].

### 1.3.4 Carcinoembryonic Antigen

Carcinoembryonic antigen (CEA) is the first serum biomarker to ever be discovered for cancers in the world [1]. However, its poor sensitivity and selectivity toward a specific type of cancer meant that it cannot be used for the detection of any type of cancer, including breast cancer [4]. Despite that, current studies show that CEA remains a valuable biomarker for the monitoring of metastatic breast cancer [55,56].

### **1.3.5 Vascular Endothelial Growth Factors**

As its name implies Vascular Endothelial Growth Factors (VEGF) function in promoting the formation of blood vessels in the tissue. Higher levels of VEGF in cancer indicate greater levels of vascularization and worse prognosis. VEGF isn't specific for any type of cancer, as such, it can't be used for the detection of breast cancer despite being an important biomarker for the prognosis of triple-negative breast cancer [4].

## **CHAPTER 2**

### **DEVELOPMENT OF A BIOSENSOR FOR THE DETECTION OF EGFR**

#### **Objective**

The goal of this chapter is to report the development of a biosensor for the detection of epidermal growth factor receptor (EGFR) in saliva. This chapter covers the detection of EGFR using EIS, then the optimization of each step of the fabrication process before developing the standardization curve for EGFR. The biosensor's selectivity was then tested by measuring interference proteins and the biosensor detected EGFR with greater sensitivity than interference proteins HER2 and HER3. This was followed by testing the biosensor's sensitivity to artificial saliva before performing the detection of EGFR in artificial saliva using the standard addition method.

## 2.1 Introduction

Discovered in the early 1980s, EGFR has attracted a lot of attention for its role in cancer development. Its overexpression is linked to an increase in cell proliferation and inhibition of cellular apoptosis, thus leading to a poor prognosis [57]. In Breast cancer, EGFR is expressed in 18 to 35 % of breast cancer, however, 50 to 70 % of triple-negative breast cancer show overexpression of EGFR. Its role in breast cancer correlates to resistance to anti-estrogen chemotherapy, with an increased chance of bone metastasis. This makes EGFR an attractive target for chemotherapy [58]. In this chapter, we will explore further the detection of EGFR, then explain the essential steps for the development of a biosensor for its detection.

### 2.1.1 Structure

As mentioned in chapter 1, EGFR is a member of the human epidermal receptor (HER) family of tyrosine kinases made up of four members known collectively as HER1 (also called EGFR) HER2, HER3, and HER4. These receptors are made up of three parts, the amino-terminal is on the extracellular domain rich in leucine and cysteine, a hydrophobic rich transmembrane domain, and the carboxylic terminus is found inside the cell with a kinase domain [52].

EGFR is a variant of this structure. It is an 1186 amino acid chain weighing in around 170 kDa. Its extracellular domain is divided into 4 domains consisting of two ligand-binding domains called L1 and L2, and of two Cysteine-rich domains called CR1 and CR2. Its transmembrane domain consists of an  $\alpha$  helix structure that allows it to pass through from one side of the membrane surface to the other. The intercellular domain is divided into two parts, the tyrosine kinase domain and the regulatory domain [57]. A schematic of the protein's shape can be seen in figure 22.

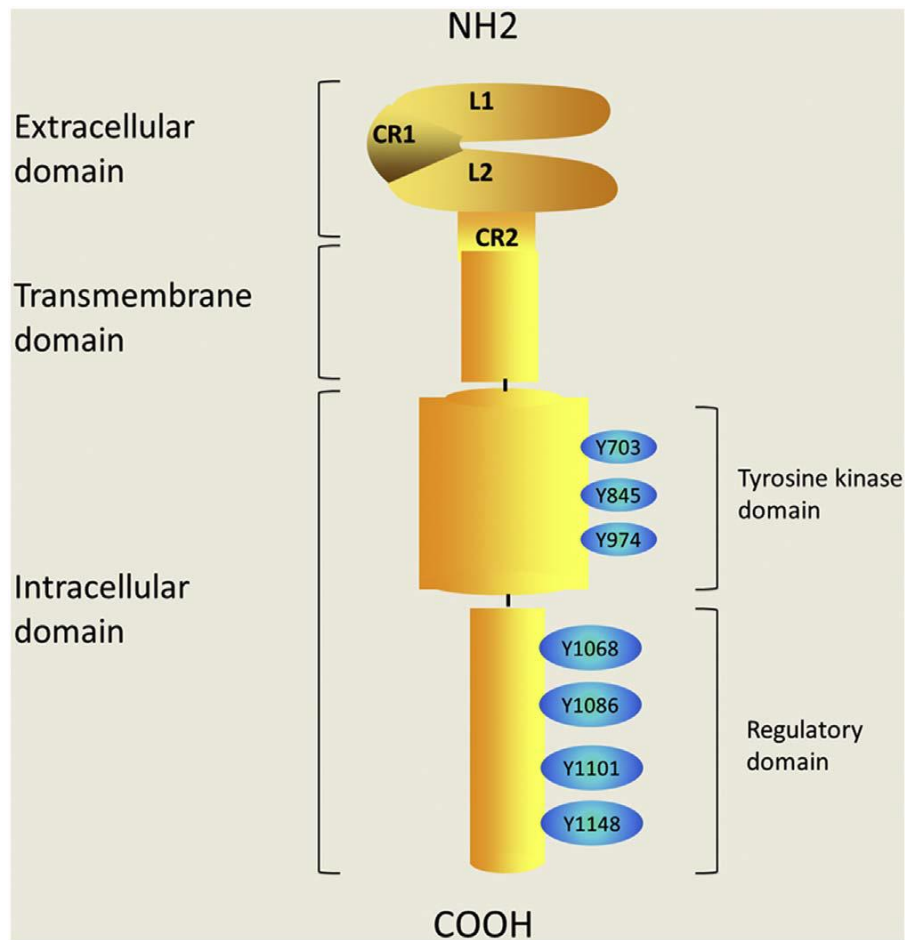


**Figure 22:** Schematic of EGFR structure [57].

### 2.1.2 Signaling pathway

As receptors, EGFR is mostly activated by epidermal growth factor protein family including the epidermal growth factor, the heparin-binding epidermal growth factor-like receptor, neuregulin, epiregulin, and amphiregulin, and transforming growth factor-alpha [58].

Once binding occurs with a ligand occurs, EGFR then binds with another HER kinase, typically another EGFR, to form a dimer and to activate its kinase function through phosphorylation. This action further activates downstream signaling actors such as AKT1, STAT3, and RAS [57].

Because of this function, 30 % of all types of all epithelial cancer deregulates EGFR. However, one problem with EGFR is that its tissue levels are good prognostic indicators, however, they are not good predictors of the

responsiveness of EGFR inhibitor therapy. This means that EGFR's activation can be independent of its kinase activity. It is worth mentioning that animal survival study shows that animals born with kinase defective EGFR can survive with only some epithelial defects, while EGFR knockout animals don't survive after their birth for long [51].

While, several studies linked this phenomenon to the heterodimerization function of EGFR [51] Other studies show that different ligands affect EGFR in different phosphorylation patterns of signaling which promotes different downstream signaling pathways [52].

As such, EGFR activity can be differentiated between its kinase activity and its non-kinase activity. EGFR's non-kinase activity plays an important role in cancer development, this includes the prevention of cancer death through autophagy. The regulation of glucose levels through non-kinase interactions with glucose-sodium pumps. It binds to pro-apoptotic signaling proteins such as PUMA to deactivates them. And finally, they can bind to specific transcription factors that can regulate and promote genes from the HER family. These activities are described in figure 23.

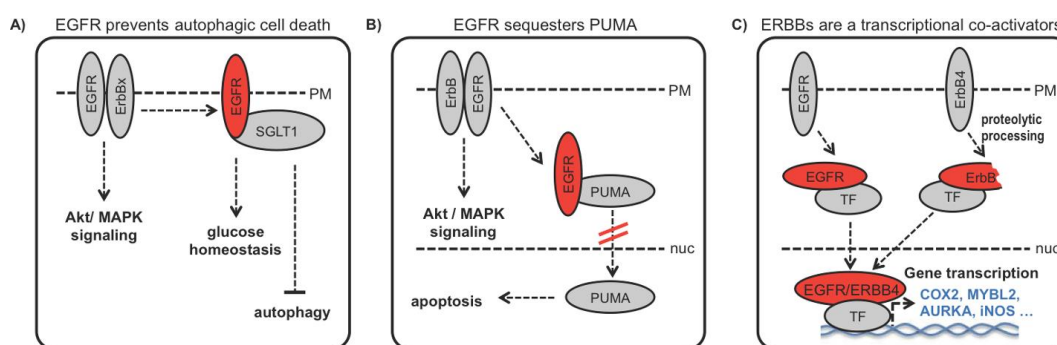


**Figure 23:** non-kinase pathways of EGFR and their outcomes showing EGFR role in A) preventing autophagy, B) inhibiting pro-apoptotic proteins, and C) regulating gene transcription pathways [51].

The canonical function of EGFR that occurs with its normal ligand-dependent activation and subsequent auto-phosphorylation and homo-dimerization include the activation of Ras/MAPK and the PI3K/AKT pathways as well as the phospholipase C and protein kinase C signaling

cascade, all of which are crucial pathways in the mobility, differentiation, and proliferation of the cell. Normal cell regulation has a tight regulation on EGFR pathways through compartmentalization and endocytosis [59]. These functions are explained in figure 24.

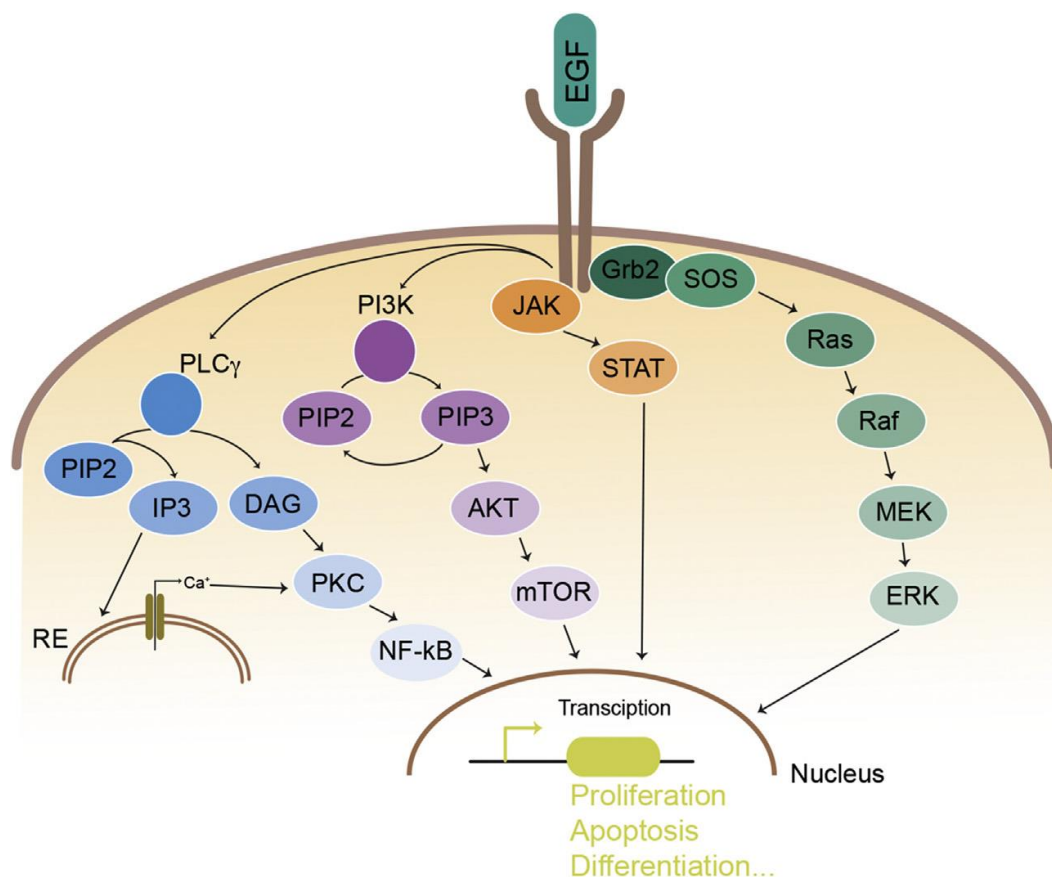


**Figure 24:** Canonical actions of the EGFR signaling pathway [60].

### 2.1.3 Clinicology of EGFR

The clinical relevance of serum EGFR has recently been studied concerning breast cancer, and it has been found that the cut-off serum concentration of EGFR is around 73 pg/mL [61]. While the salivary concentration of EGFR in breast cancer is around 100 pg/mL [62].

EGFR serum concentration is mostly used in the prognosis of breast cancer and for the prediction of the success of breast cancer anti-EGFR therapy [61].

## 2.2 Materials and Methods

### 2.2.1 Materials

All chemical reagents were purchased from Sigma Aldrich and they are:

- N-hydroxysuccinimide (NHS),
- N-(3-dimethylaminopropyl)-N-ethyl-carbodiimide hydrochloride (EDC),
- 4-aminophenylacetic acid (4-carboxymethylaniline (CMA)),
- sodium nitrite ( $\text{NaNO}_2$ ),
- hydrochloric acid (HCl),
- potassium Ferro cyanide,
- potassium Ferry cyanide trihydrate,
- Sodium Chloride,
- Potassium Chloride,
- Calcium Chloride anhydrous,
- Mucin from pork stomach extract,
- Sodium Phosphate dibasic,
- Sodium Hydroxide,
- Urea,
- ethanolamine,
- Phosphate buffer saline solution (PBS),

All biological compounds were purchased from R&D system:

- Anti-EGFR antibody
- EGFR antigen
- HER2 antigen
- HER3 antigen

The equipments used are as follows:

- Palmsens 4

- Fisher Scientific FB 15049 sonicator

The electrodes that were used for the detection are explained in appendix A.

## **2.2.2 Methods**

### **2.2.2.1 Microfluidic system**

The electrodes explained in annex A were used in a microfluidic system. The microfluidic system is a polyacrylic block that was microfabricated in two parts. The upper part is made up of eight microfluidic cells that align with each of the eight integrated working electrodes. Each cell has its own entry channel and exit channel. A specialized titanium oxide nutplug is used to seal these channels and to link them to PTFE microtubes. The cells themselves are sealed using rubber rings to prevent leakage. The lower part is used to seal the electrodes in place. Figure 25 (A-C) shows the microfluidic system, the nutplugs, the rubber rings and how the electrodes are sealed in place. And Figure 25 (D-E) shows how to insert the microarray into the microfluidic system.

The system is then filled connected to the potentiostat PalmSens 4 using a specialized connector that links each of the integrated electrodes on the array to the microfluidic system. The entire system is used in a Faraday cage in order to minimize the noise in the measurements. Figure 25 (F) showcases the system.

Finally, the introduction of solutions into the system is done manually through a 1 mL syringe with a 25G needle. The solution is introduced slowly to avoid the penetration of bubbles and the cell in which the electrode is being studied needs to remain wet throughout the experiment. An example of how to use the microfluidic system can be found in figure 25 (G).

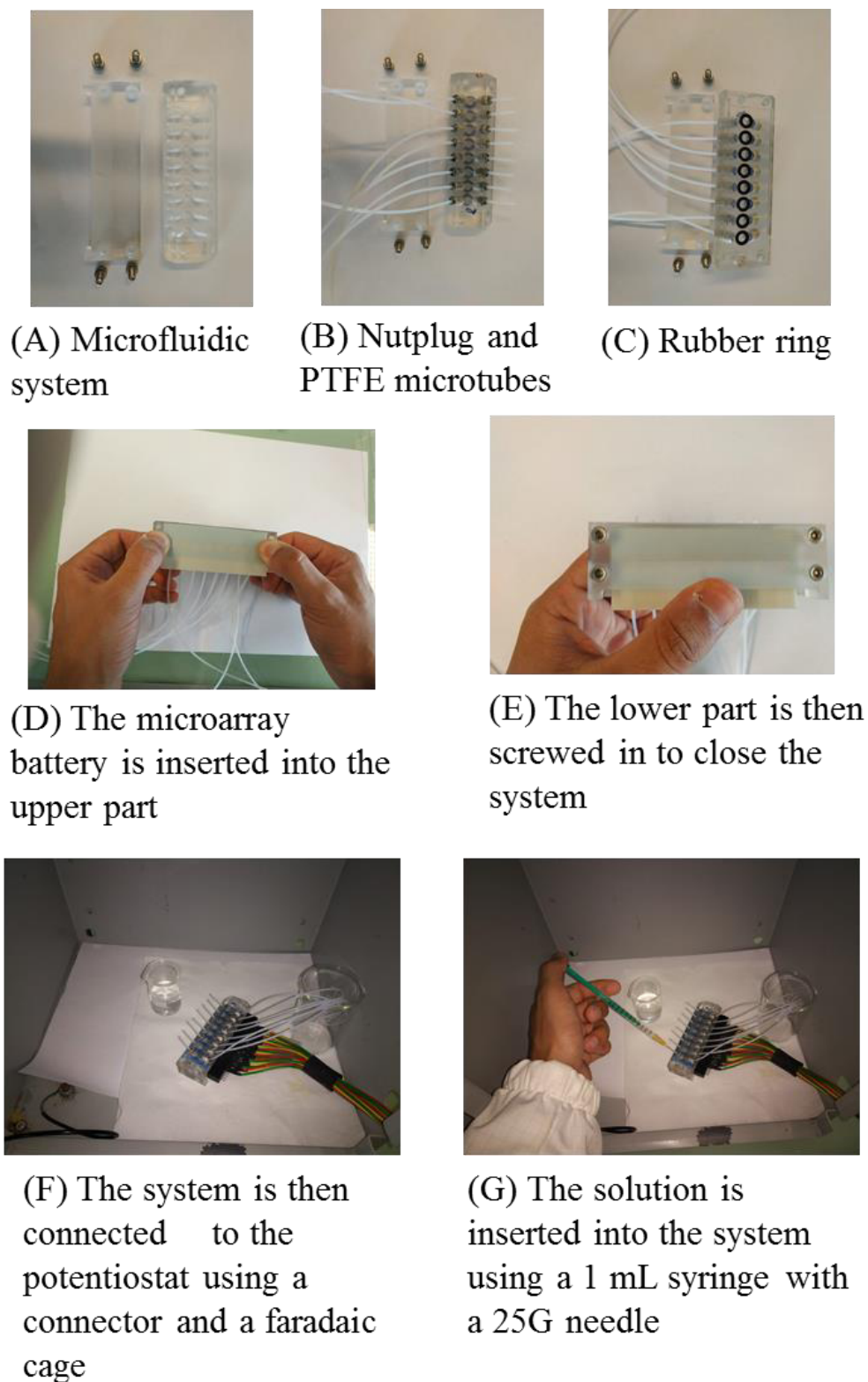


**Figure 25:** (A) A picture of the microfluidic system, (B) The nutplug and the PTFE tubes attached to the channels, (C) the rubber rings that seal the channel, (D) first step in closing the system, (E) the second step in closing the system, (F) the experimental set-up, (G) Filling the microfluidic system with solutions.

### 2.2.2.2 Electrochemical characterization

The characterization of the WE are done using two electrochemical techniques:

- Electrochemical impedance spectroscopy uses  $E_{dc} = 0.172$  V with an amplitude  $E_{ac} = 10$  mV from 1 Hz to 10000 Hz. It is performed in a 5 mM Ferro/Ferry cyanide PBS solution at room temperature.
- Cyclic voltammetry (CV) is also performed in 5 mM Ferro/Ferry cyanide PBS solution at room temperature. The applied potential window is from -0.4 to 0.6 V against the reference electrode, with a scan rate of 80 mV/s with an E-step of 1 mV. The scan is repeated 3 times.

### 2.2.2.3 CMA electrodeposition

The electrodeposition of CMA was performed as the first step for the functionalization of the working electrode. The electrodeposition was performed by first:

- Dissolving 3 mM CMA in deionized water using 10 min sonication.
- Activating the CMA solution by mixing it with 20 mM solution of  $\text{NaNO}_2$  and 20 mM of HCL solutions
- Incubating the activated for 10 min at 4°C.
- Electrodeposition of CMA using CV with the following parameters:
  - The scan rate of 15 mV/s.
  - Potential window: from -1.2 to 0 V.
  - The number of scans: 15 cycles.

It is worth mentioning that the electrodeposition of CMA was optimized, the optimization steps are discussed in the supplementary materials under the Apeendix B.

#### **2.2.2.4 Immobilization of anti-EGFR antibody.**

The immobilization of anti-EGFR was done using esters EDC/NHS protocol:

- The electrode was first incubated in a solution of EDC (0.4 M)/NHS (0.1 M) dissolved in deionized water for 40 min.
- The electrode is then washed with PBS and incubated in a solution of anti-EGFR (10 µg/mL) in PBS for 40 min.
- The electrode is washed in PBS then incubated with a solution of ethanolamine in PBS (1/1000) for 30 min.
- Characterization of the electrode using EIS as described in paragraph 2.2.2.1.

It should be mentioned that the parameters of the immobilization of the anti-EGFR antibody were optimized. The optimization steps are described in the supplementary materials in appendix C.

#### **2.2.2.5 Electrochemical measurement of EGFR, HER2, and HER3 concentrations**

The electrochemical measurement was performed inside a microfluidic system following these steps:

- cleaning the microfluidic cell with the electrode inside with 1 mL PBS.
- introducing the lowest standard protein concentration inside the cell for 30 min.
- the cell is then cleaned with 1mL PBS.
- The cell is then filled with 0.5 mL of 5 mM of Ferro/Ferry cyanide in PBS before performing EIS characterization as described above.
- The cycle is then repeated for the second standard protein concentration.

### **2.2.2.6 Study of the effect of artificial saliva on the SPE**

Artificial saliva is a mixture of 0.6 g/L anhydrous calcium chloride, 0.6 g/L phosphoric acid dibasic, 0.4 g/L potassium chloride, 0.4 g/L sodium chloride, 4 g/L mucin, and 4 g/L urea dissolved in deionized water through sonication and later had its pH is adjusted to 7.2 using NaOH (0.1M), before finally being sterilized by autoclaving before storing it at  $-4^{\circ}\text{C}$ .

The use of artificial saliva is meant to mimic the effects of real saliva while using desired concentrations of a particular biomarker. As such, it was imperative to study the effects of artificial saliva has on the biosensor without the addition of the biomarker, this was done through diluting the artificial saliva five times (1/2, 1/10, 1/100, 1/500, 1/1000) then characterizing the SPE using EIS after incubating it in the diluted artificial saliva starting from the least concentrated artificial saliva to the most concentrated.

### **2.2.2.7 Standard addition method**

The use of artificial saliva is to imitate the matrix effect of real saliva for studying, as such, a standard solution of EGFR of pre-determined concentration of 1 ng/mL is first prepared by mixing a stock solution of 1000  $\mu\text{g}/\text{mL}$  of EGFR in artificial saliva then diluting said EGFR concentration using artificial saliva to the desired concentration of 1 ng/mL. The pre-determined EGFR concentration of 25  $\text{pg}/\text{mL}$  is then prepared by adding it at a constant volume of to each of five volumetric flasks of 1.5 mL.

The first flask is then filled to the final volume using PBS. For the flasks 2 to 5, a volume of the standard solution of EGFR of 2 ng/mL is then added in increasing volumes to the volumetric flasks in ascending order, in order to create the desired concentration of 50  $\text{pg}/\text{mL}$ , 80  $\text{pg}/\text{mL}$  100  $\text{pg}/\text{mL}$ , 120  $\text{pg}/\text{mL}$  in their subsequent flasks after filling them to the final volume using PBS.

## 2.3 Results and discussion

### 2.3.1 CMA electrodeposition

The electrodeposition of CMA for the detection of EGFR has been fully explored in Appendix B.

### 2.3.3 Detection of EGFR, HER2 and HER3

The EIS measurement of EGFR was carried out for each and every concentration that was use. The results can be displayed in either Nyquist plot which shows the real impedance versus the imaginary impedance, while the bode plot shows the logarithmic of the total impedance versus the logarithmic of the frequency. Each graphical representation is explained in chapter 1. For the detection of EGFR, the Nyquist plot was used for the better presentation as seen in figure 26.

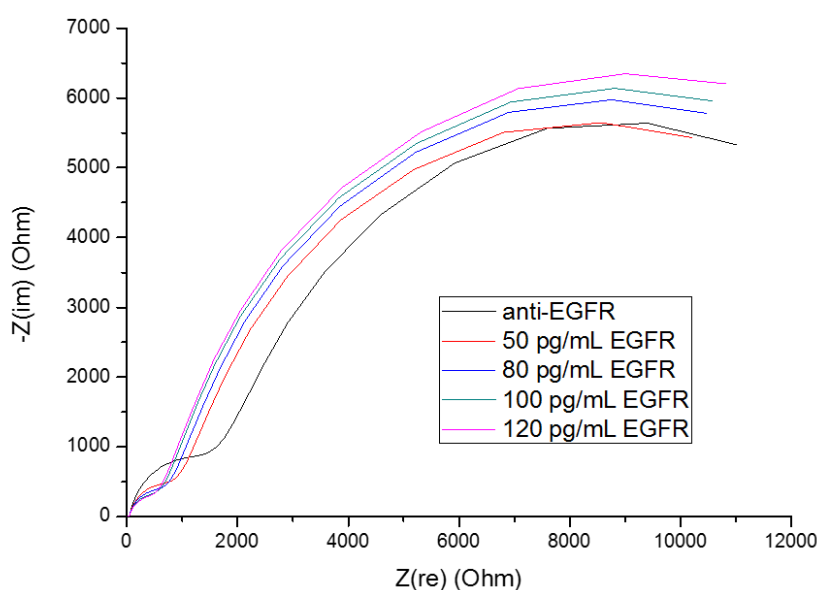


**Figure 26:** Nyquist plots showing the EIS measurements of EGFR concentrations with the measurement after the immobilization of anti-EGFR antibody in black, after incubation of 50 pg/mL EGFR in red, 80 pg/mL EGFR in blue, 100 pg/mL EGFR in green, and 120 pg/mL EGFR in magenta

The Nyquist plots of the concentrations shows Two semi circles that are behaving rather differently from one another, while the first semicircle

shows a continuous decline with the increased concentrations, the second part of the semicircle shows a continuous increase with the increased concentrations. This responsiveness to the concentrations indicate that the biofunctionalized electrodes have a good reactivity toward EGFR.

Each of the Nyquist plots was then fitted using EIS analyzer, an open source software whose function is to take a Nyquist plot and turn it into an arithmetic value through modelization of the plot values with an equivalent circuit. The equivalent circuit used can be found in figure 27.

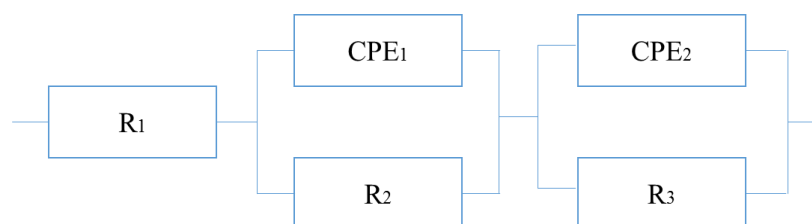


**Figure 27:** Equivalent circuit used in the modelization of the Nyquist plots.

The use of the above equivalent circuit is due to the two semi-circles of the Nyquist plots, it allows for better fitting with less amount of errors. This equivalent circuit is made up of five components,  $R_1$  is the solution resistance, and two charge transfer resistances  $R_2$  and  $R_3$ , and two double layer capacitance called  $CPE_1$  and  $CPE_2$  with each of the charge transfer resistances being in parallele to a constant phase element. The result of the fitting can be seen in table 1 below.

**Table 1:** Modelization result of the EGFR Nyquist plot.

	<b>0 pg/mL EGFR</b>	<b>50 pg/mL EGFR</b>	<b>80 pg/mL EGFR</b>	<b>100 pg/mL EGFR</b>	<b>120 pg/mL EGFR</b>
$R_1 (\Omega)$	45.353	43.015	41.802	40.355	39.955
$R_2 (\Omega)$	1552.1	865.37	703.91	572.58	517.21
$R_3 (\Omega)$	14832	15144	16122	17033	18193
$Q_1 (s^n \Omega^{-1})$	0.0000071	0.0000083	0.0000091	0.000010	0.000010
$n_1$	0.8614	0.8377	0.8255	0.8111	0.8101
$Q_2 (s^n \Omega^{-1})$	0.000067	0.000069	0.000066	0.000065	0.000066
$n_2$	0.8289	0.8186	0.8150	0.8116	0.8033

<i>Fitting error</i>	0.000090	0.000089	0.00011	0.00012	0.00012
----------------------	----------	----------	---------	---------	---------

From table 1, R3, which is the charge transfer resistance of the second semi-circle, is the parameter with the highest degree of correlation toward the increase in EGFR concentration, as such, it is used for the calculation of the normalization of the results. Normalization is the calculation of the charge transfer resistance that allows the removal of inter-electrodes variation, it follows equation 2.1.

$$\Delta R/R = \frac{|R_{EGFR} - R_{anti-EGFR}|}{R_{anti-EGFR}} \quad 2.1$$

From the normalization of the result, the standardization curve for all the repetitions can then be calculated. The resulting standardization curve of the detection of EGFR is seen in figure 28.

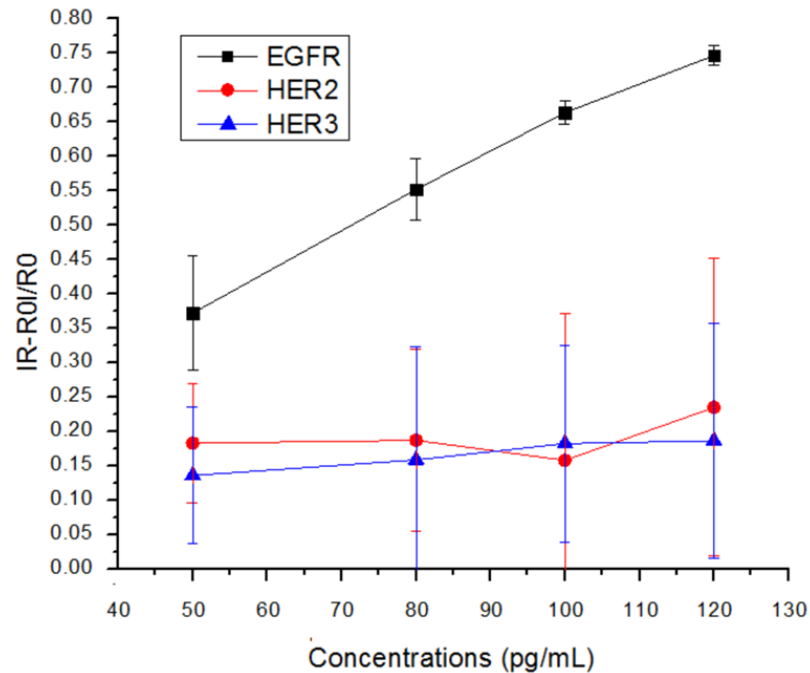


**Figure 28:** Standardization curve of the detection of EGFR (black), HER2 (red), and HER3 (blue) showing the normalized signal versus the concentration of the proteins in pg/mL.

The equation of the standardization curve of EGFR is then:

$$Y = (0.0048 \pm 0.0005) X + (0.1761 \pm 0.0540) / R\text{-square} = 0.9710.$$

In addition to the detection of EGFR, HER2 and HER3 were used to test the selectivity of the biosensor for the detection of EGFR. The main reason for using HER2 and HER3 is their close structure to EGFR, in addition, it was recommended by the manufacturer R&D systems to use them to test the cross-reactivity of the system. The resulting standardization curve for HER2 is  $Y = (-0.0001 \pm 0.0011) X + (0.3946 \pm 0.1116)$ / R-square = 0.4934 and for HER3 is

$Y = (0.0008 \pm 0.0001) X + (0.0963 \pm 0.0080)$ / R-square = 0.9553, their sensitivity being far lower than that of EGFR proves that the biosensor is selective to EGFR. It should be noted that the errors on the curve are the representation of the standard deviation obtained after several repeats of the measurements.

#### **2.3.4 Effect study of artificial saliva on the biosensor**

Artificial saliva is a medium in which simulates the chemical composition and properties of real saliva. Because of that, it needed to be studied in order to fully understand its effect on the biosensor before its use. The study shows the effect of increasing artificial saliva concentration has on the biosensor, the result is seen in figure 29. We can see the matrix effect increases with the increase in the artificial saliva concentration. This study allows us to determine which concentration is necessary to perform the standard addition method.

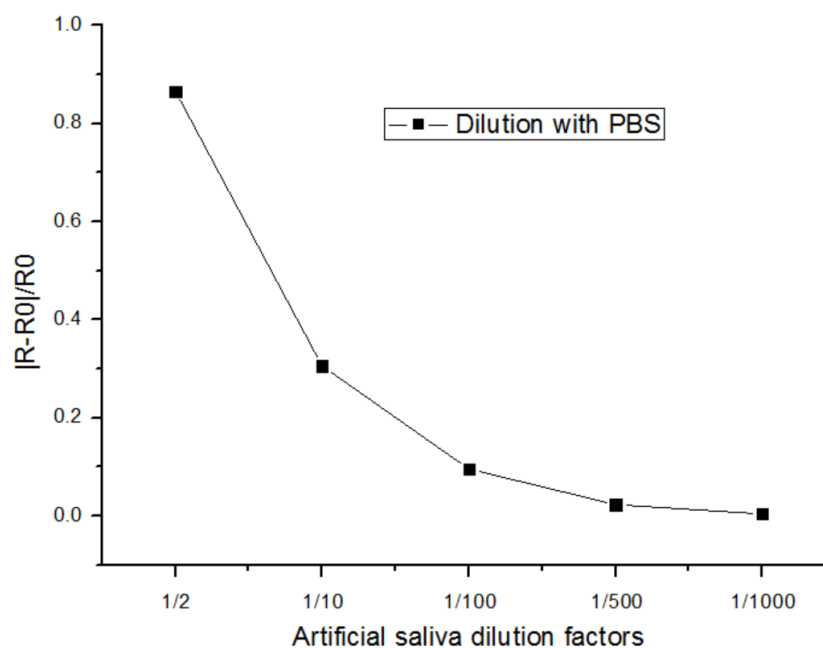


**Figure 29:** Effect of artificial saliva concentration on the biosensor.

### **.2.3.5 Detection of EGFR in artificial saliva using the standard addition method.**

The standard addition method is a method generally used to detect a specific molecule such as minerals and biomarkers in a complex medium such as biological fluids including saliva. The modus operandi of this method is through adding a known amount of standard solution of the specific molecule that is being detected in a linearly increasing order to a solution of unknown sample analyte. The accuracy of the biosensor was then calculated with the following equation:

$$\text{Accuracy} = \frac{[\text{EGFR}]_{\text{artificial saliva}}}{\left| \frac{\text{Y-intercept}}{\text{Slope}} \right|} * 100 \quad 2.2$$

The accuracy is obtained by dividing the EGFR concentration in artificial saliva with the x-axis intercept in absolute (obtained from dividing the y-axis intercept of the linear regression obtained from the detection of EGFR using the standard addition method), then multiplying it by 100

The method in which this is done is described in paragraph 2.2.2.6, the resulting Nyquist plot from this detection was fitted then its values were normalized. This value was then placed in the y-axis and drawn versus the standard concentration that was added in the x-axis. This resulted in figure 30 shown below.

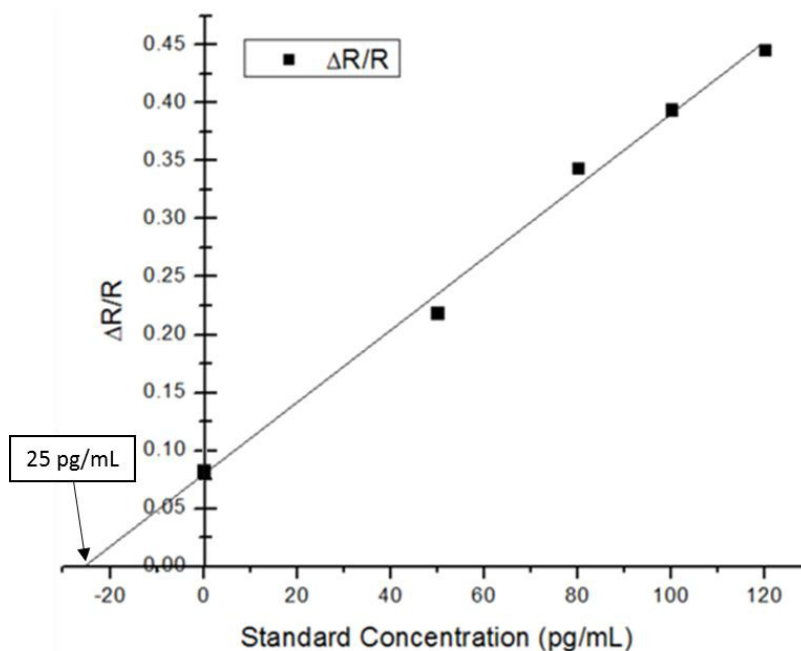


**Figure 30:** Plot showing the detection of EGFR in artificial saliva using the standard addition method.

The standard addition method showed high levels of linearity:

R-square = 0.9912 as well as high levels of accuracy; with a detection curve of  $Y = 0.0031 X + 0.0795$  detecting the pre-determined concentration of 25 pg/mL with an accuracy of 97.5%. showing that the biosensor can be used for the detection of EGFR in saliva. When compared to other biosensors in the literature, found in table 2, our biosensor remains the only biosensor specifically designed for the detection of EGFR in saliva on the market.

**Table 2:** List of electrochemical biosensors developed for the detection of EGFR.

<b>Electrode type and material</b>	<b>Detection method</b>	<b>Optimization</b>	<b>Linear detection range</b>	<b>Limit of detection</b>	<b>Medium of detection</b>	<b>reference</b>
Gold SPE modified with Molecular imprinted polymer based on acrylamide	PSA*	Antibody decorated liposomes filled with CdII and CuII	0.05 – 50000 pg/mL	0.01 pg/mL	Human serum	[63]
streptavidin-coated magnetic beads	SWASV**	Bovine serum albumin templated Pb nanocluster probe	0.4 ng/mL - 35 ng/mL	8 pg/mL	Human serum, in vivo detection	[64]

\* potentiometric stripping analysis, \*\* square wave anodic stripping voltammetry

## 2.4 Conclusion

This chapter explored the development of a biosensor for the detection of EGFR. This chapter covers all the optimization steps taken to create the best detection possible, from optimization of the immobilization of anti-EGFR antibody to optimizing the electrodeposition of CMA on the SPE's surface. This is followed by detecting EGFR in PBS using EIS and drawing a standardization curve for this detection, then showing the selectivity of the biosensor by showing that it is six times more sensitive to EGFR than HER3 while it is not sensitive at all to HER2. This is followed by testing the effect of artificial saliva on the biosensor's surface then detecting EGFR in artificial saliva using the standard addition method. Thus, showing that the biosensor can be used for the detection of EGFR in real saliva.

## CHAPTER 3

### DEVELOPMENT OF A BIOSENSOR FOR THE DETECTION OF P53

#### Objective

The aim of this chapter is to report on the development of a biosensor for the detection of p53 in saliva. The biosensor must henceforth fulfill the following conditions for it to be functional for the detection of p53, first it must detect p53 in PBS with greater sensitivity against the interferences. The other is that p53 must be able to show a linear detection with a relative level of accuracy when detecting p53 in artificial saliva. These two conditions will allow p53 to be clear for use with real saliva from patients. Carrying out these two detections are done through two phases:

Phase one allowed the detection of p53 in PBS. This phase cover firsts testing the fabrication of the biosensor for such detection, this step is followed by confirmation of the recognition using Bradford assay. Then the biosensor was tested for interferences.

Phase two is the detection of p53 in artificial saliva, this phase uses artificial saliva to mimics real saliva in testing the detection method for p53 which is done through the standard addition method. The aim of phase two as mentioned above is to test whether the detection of p53 in artificial saliva is linear or not, as linearity implies that standard addition method can be further used for the detection of p53 in real patients.

### **3.1 Introduction**

p53 is, without competition, the most comprehensively studied tumor suppressor protein to date. While, canonically, its main function is to regulate the life of a cell and search for gene damage, p53 is proving to be much more multifaceted than previously thought because of its role in regulatory pathways functioning for metabolic homeostasis. This role is most prevalent in breast cancer where p53 shows a clear association through the modulation of key proteins in mitochondrial metabolism, cytochrome c oxidase 2 synthesis, and the TP53-induced glycolysis and apoptosis regulator (TIGAR) [47]. In this introduction, we will explore p53 further along with its association with breast cancer.

#### **3.1.1 P53 structure**

p53 protein is made up of 393 amino acids (a.a.) consisting of six main domains: The N-terminal transactivation domain (TAD1) made up of the 1-42 a.a. is followed by another transactivation domain (TAD2) from 43-61 a.a. and they are the parts of the protein responsible for the activation of several transcription factors (such as TFIID and TFIIH) along with several TATA box-binding protein associated factors; the Pro-rich domain (PRD) from 61-92 a.a. is important for p53 stability and activity; the central DNA binding domain (DBD) from 101-300 a.a. is the region that recognizes DNA; the tetramerization domain (TD) from 326-356 a.a. allow the full-length p53 to reversibly form tetramers; and the C-terminal basic domain (BD) from 364–393 regulates the binding of p53 on specific sequences of DNA [65]. Details about its structure can be found in figure 31.

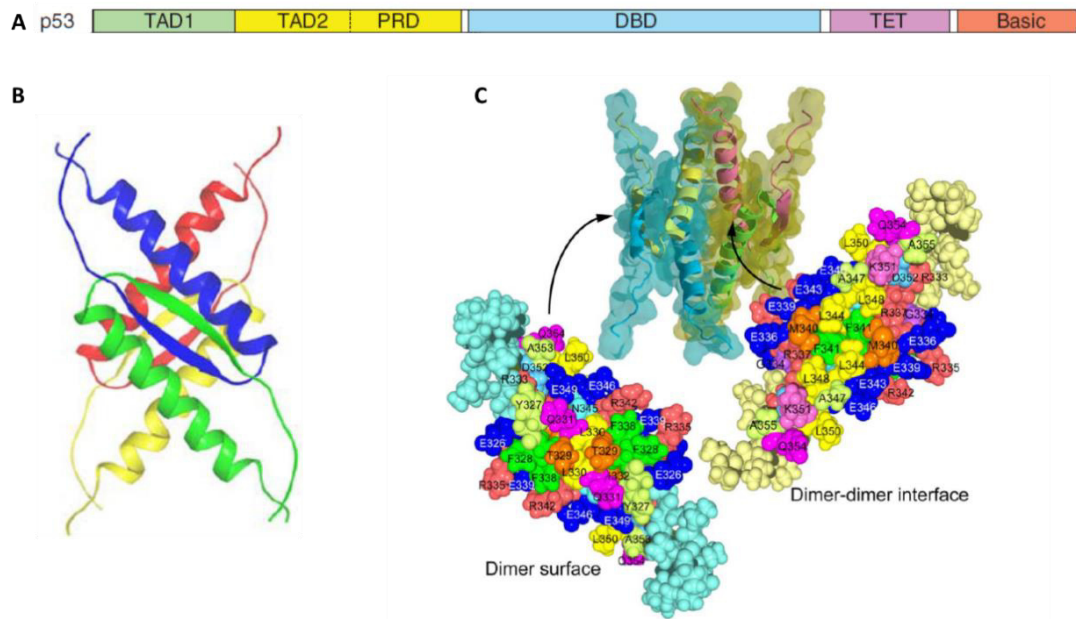


**Figure 31:** Structure of p53 showing A the relative position of each domain, B the structure of each domain, and C the dimer surface of each domain [65].

### 3.1.2 P53 functions in breast cancer

The canonical function of p53 is the protection of DNA and triggering apoptosis when DNA is irreversibly damaged. However, p53 function is strongly regulated by female hormones that regulate mammary glands during pregnancy, which in turn, influences women's predisposition to breast cancer. However, the use of p53 during pregnancy to predict the onset of hormone-dependent breast cancer is still in its early stages and as such it is too early to tell, although the role of p53 in hormone-dependent breast cancer and its role in pregnancy is well documented [48]. Its activity is summarized in figure 32.

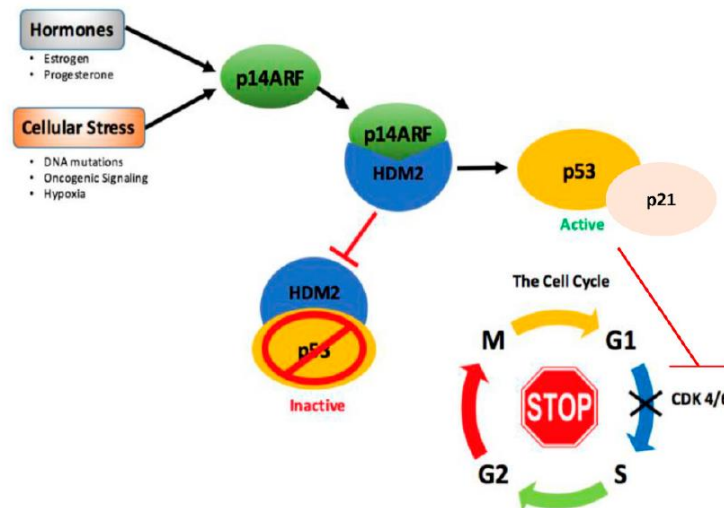


**Figure 32:** Activation pathway of p53 through hormone or cellular stresses [48].

### 3.1.3 Clinicology of p53 in breast cancer

Currently, p53 is mostly used for prognostic and predictive analysis in breast cancer [66]. However, some research has been carried out regarding its presence in saliva which showed a concentration of 4  $\mu\text{g/mL}$  for healthy individuals and 6  $\mu\text{g/mL}$  for patients with metastatic cancer [62]. In addition, recent studies are showing that p53 has great clinical importance because of its function in triple-negative breast cancer [67], while at the same time suffering mutations in most other types of breast cancer as shown in figure 33.

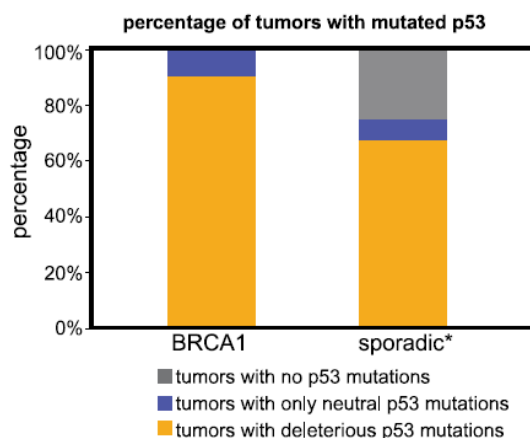


**Figure 33:** percentage of mutation in BRCA1 breast cancer and other types of breast cancer [68].

## 3.2 Experimental

### 3.2.1 Materials

All chemical reagents were purchased from Sigma Aldrich and they are:

- 4-aminophenylacetic acid (4-carboxymethylaniline (CMA)),
- sodium nitrite ( $\text{NaNO}_2$ ),
- hydrochloric acid (HCl),
- N-hydroxysuccinimide (NHS),
- N-(3-dimethylaminopropyl)-N-ethyl-carbodiimide hydrochloride (EDC),
- ethanolamine,
- Phosphate buffer saline solution (PBS),
- potassium Ferrocyanide,
- potassium Ferry cyanide trihydrate,
- Sodium Chloride,
- Potassium Chloride,
- Calcium Chloride anhydrous,
- Mucin from pork stomach extract,
- Sodium Phosphate dibasic,
- Sodium Hydroxide,
- Urea,
- Bradford reagent

All biological compounds were purchased from two subsidiaries of Biotechne and they are:

- From Novus analytica
  - p53 antigen
  - MUC1 antigen
- From R&D system:
  - p53 antibody

- HER3 antigen

The equipments used are as follows:

- Palmsens 4
- Fisher Scientific FB 15049 sonicator
- Jenway 7205 UV/Visible spectrophotometer

The electrodes used are explained in appendix A.

### **3.2.2 Methods**

#### **3.2.2.1 Electrochemical characterization**

Two techniques used for the characterization of the SPE:

- Cyclic voltammetry (CV) is performed in 5 mM Ferro/Ferry cyanide PBS solution under room temperature, the parameters used are from -0.4 to 0.6 V against the reference electrode, with a scan rate of 80 mV/s with an E-step of 1 mV. The scan is repeated 3 times
- Electrochemical impedance spectroscopy is performed in 5 mM Ferro/Ferry cyanide PBS solution at room temperature, the parameters used are  $E_{dc} = 0.172$  V against the reference electrode,  $E_{ac} = 10$  mV, Frequency window from 1 Hz to 10000 Hz.

#### **3.2.2.2 CMA deposition**

The electrodeposition of CMA was done by:

- Dissolution of 3 mM CMA in 3 mL of deionized water using sonication.
- Mixing the CMA solution with 60  $\mu$ L solution of 1 M sodium nitrite and 60  $\mu$ L of 1 M solution of hydrochloric acid.
- Incubating the CMA solution at a temperature of 4° C for 10 min
- Introduction of CMA solution in the microfluidic cell
- Launching a CV with the following parameters:
  - The potential window is 0 to -1.2 V

- Scan rate is 15 mV/s
- Number of scans: 15

### **3.2.2.3 Antibody immobilization**

The antibody anti-p53 is immobilized on the electrode surface by using EDC/NHS without a microfluidic system using a here step process:

- The electrode, activated with CMA, is submerged in a solution of 1 mL EDC (0.4 M)/ NHS (0.1 M) for 40 min before washing it with PBS and drying it with air.
- The same electrode is then submerged in 10  $\mu\text{g/mL}$  of the antibody anti-p53 for 40 min.
- The same electrode is finally submerged in a solution of 1/1000 ethanalamine in PBS for 30 min

Once the immobilization is done, the electrode is characterized in EIS using the technique described above. It is worth mentioning that from this point forward, the electrode must always remain submerged in a form of PBS solution to not destroy the proteins on the surface.

### **3.2.2.4 Electrochemical measurement of p53 concentrations**

The electrochemical measurement is performed by first cleaning the microfluidic cell with the electrode inside with 1 mL PBS, then introducing the lowest standard protein concentration inside the cell for 30 min. It is worth mentioning that the minimum volume needed to introduce any solution is 100  $\mu\text{L}$  however, a volume of 300  $\mu\text{L}$  is preferable to ensure the removal of any possible impurities inside the cell.

After the 30 min, the cell is cleaned using a PBS solution, followed by introducing 0.5 mL of 5 mM of Ferro/Ferry cyanide in PBS before performing EIS characterization as described above.

Once the characterization is performed, the cell is then cleaned with PBS before introducing a higher concentration of the standard protein solution for

another 30 min. The cycle is then repeated for all the designated standard protein concentrations in ascending order.

### 3.2.2.5 Bradford assay.

It is worth mentioning that Bradford assay is performed without the use of a microfluidic system. After immobilization of anti-p53, 100  $\mu\text{L}$  of the standard protein concentration is placed on top of the electrode for 30 min in the same order described above, then 100  $\mu\text{L}$  of the solution is removed for further analysis. This is followed by mixing 100  $\mu\text{L}$  of the standard protein concentrations and the sampled standard concentration after incubation, and mixing each with 100  $\mu\text{L}$  of the Bradford assay reagent for 5 min before measuring their absorbance at 595 nm [69]. Figure 34 further explains how the assay is carried out.

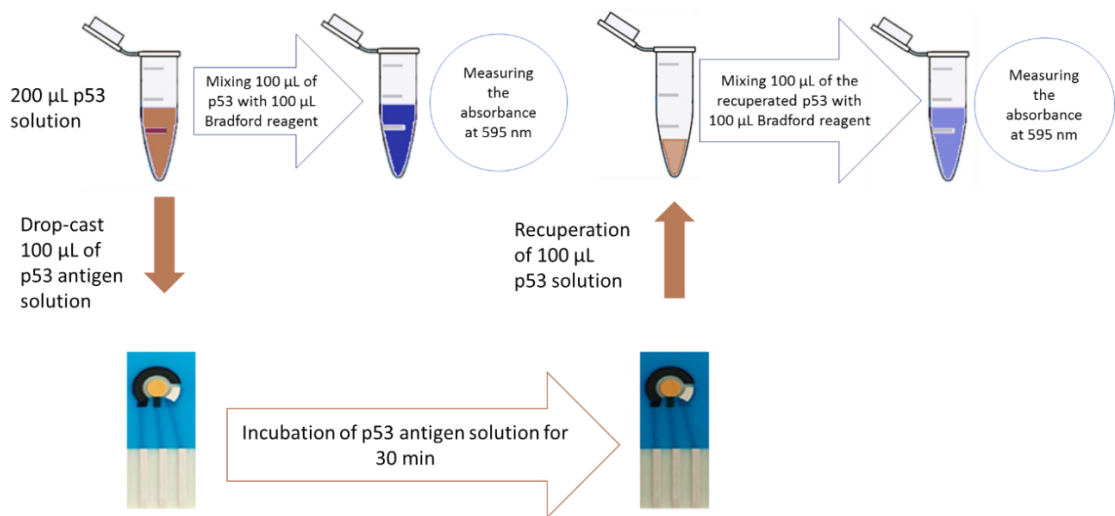


**Figure 34:** Schematic of the Bradford assay.

### 3.2.2.6 Standard addition method using artificial saliva

Artificial saliva is prepared by mixing 0.6 g/L  $\text{Na}_2\text{HPO}_4$ , 0.6 g/L anhydrous  $\text{CaCl}_2$ , 0.4 g/L  $\text{KCl}$ , 0.4 g/L  $\text{NaCl}$ , 4 g/L mucin, and 4 g/L urea in deionized water and the pH is adjusted to 7.2 using  $\text{NaOH}$  (0.1M) and finally sterilized by autoclaving before storing it at  $-4^\circ\text{C}$ .

Artificial saliva is used to prepare standard p53 solutions to use them in the detection of a predetermined concentration of p53. This is done as a proof of concept to test whether the biosensor works in saliva or not. The standard solutions are first prepared by mixing a stock solution of 4.5 mg/mL p53 in the artificial saliva to create a 100  $\mu\text{g/mL}$  solution. The pre-determined p53 concentration is then prepared by adding it at a constant volume of 9  $\mu\text{L}$  to each of five volumetric flasks of 1.5 mL. This creates a pre-determined solution of 3  $\mu\text{g/mL}$  of p53 to be determined.

A volume of 291  $\mu\text{L}$  of PBS with 1M Urea was added to the first flask containing only the predetermined concentration to reach a total of 300  $\mu\text{L}$ . For the flasks 2 to 5, the p53 standard solution (dissolved in PBS with 1 M Urea) of 100  $\mu\text{g/mL}$  is then added in increasing volumes (3, 12, 21, and 30  $\mu\text{L}$ ) to the volumetric flasks in ascending order, which corresponds respectively to the concentration of 1, 4, 7 and 10  $\mu\text{g/mL}$  of p53 in the subsequent flasks and each flask was then filled to the final volume of 300  $\mu\text{L}$  with PBS with 1M Urea.

### **3.3 Results**

#### **3.3.1 CMA electrodeposition**

To further elaborate on the electrodeposition of CMA, this step is done by first reducing CMA into diazonium salt *in situ* by mixing it with  $\text{NaNO}_2$  in a solution of HCl, followed by electrodeposition by CV as explained in paragraph 3.2.2.2, the steps taken for the electrodeposition are elaborated in Figure 35 (A). Several observations can be made on the electrodeposition's cyclo-voltammogram, shown here in figure 35 (B); the first cycles showed a reduction wave at -1.1V which corresponds with the reduction reaction of diazonium salt and the formation of radical amine. The cycles that followed the first one showed a continuous decrease in the resulting current. This can be caused by the decrease in electron transfer rate which follows the

formation of CMA blocking layer on the surface of the electrodes [70]. The outcome of the electrodeposition on the conductivity of the SPE is shown in figure 35 (C). The disappearance of the oxido/reduction peaks from bare gold after deposition of CMA was caused by the blocking effect of CMA thus creating a weak electron transfer kinetics.

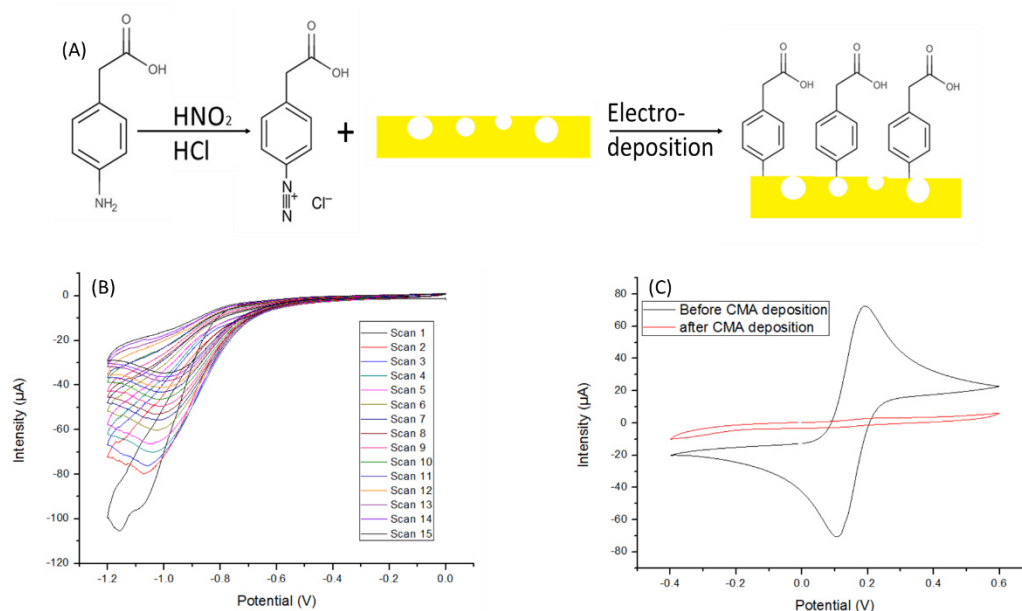


**Figure 35:** (A) reactions for the electrodeposition of CMA on gold SPE, (B) cyclic voltammogram for the electrodeposition of CMA, (C) CV characterization of SPE before and after electrodeposition.

### 3.3.2 EIS measurements of p53

The resulting EIS measurement of p53 is a spectrum that can be represented in two forms, Nyquist and Bode plots. The shape of these two plots informs the choice of the equivalent circuit which is a necessary step in the detection process. For this detection Nyquist plot showed better differentiation as such, it was chosen to represent the measurement.

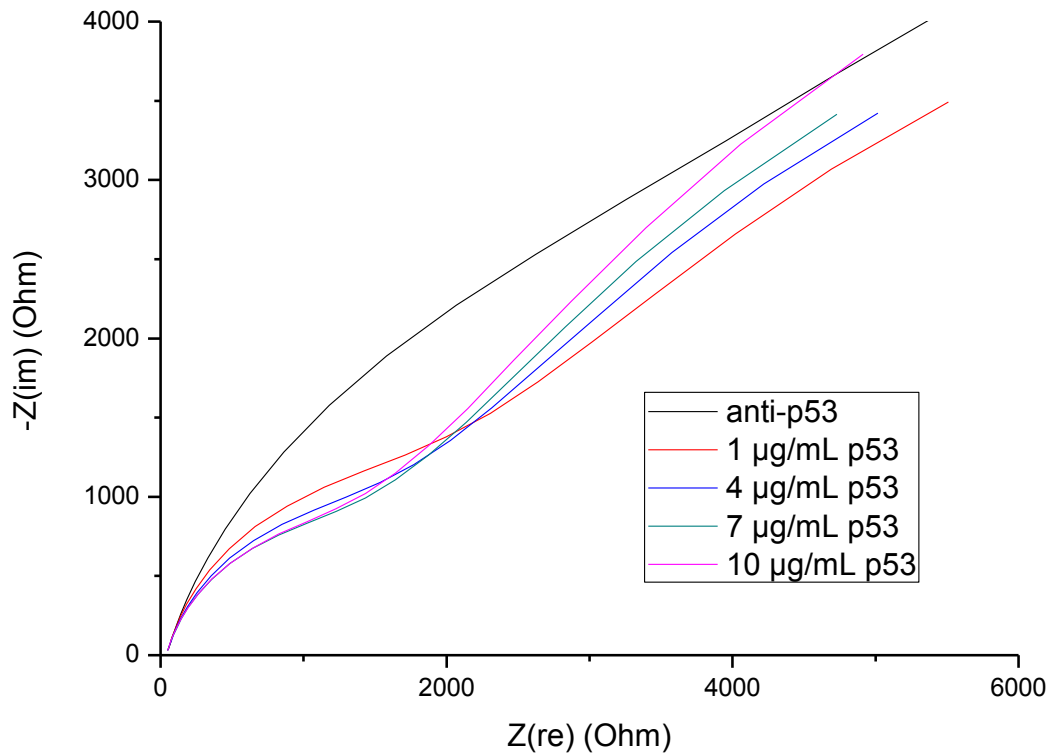


**Figure 36:** The Nyquist plot of a typical detection of p53 showing the variation of different concentrations (from anti-p53 (black), 1 (red), 4 (blue), 7 (green), 10 (magenta)  $\mu\text{g/mL}$ ).

The Nyquist plots in figure 36 show two distinct variations, a gradual fall at the high frequencies (the left part of the plot) and a repeated increase in the high frequencies (the right part of the graph). This indicates that there exist two distinct layers that behave differently from each other, as such, the equivalent circuit needs to reflect that by having two sets of parallel components in  $CPE_1$ ,  $R_2$ , and  $CPE_2$ , and  $R_3$ , with  $R_1$  being the solution resistance, the configuration can be seen in figure 37. This is typical for a Nyquist plot of a porous electrode and it conforms with present literature as explored in chapter 1 part 1.2.4.2.2.

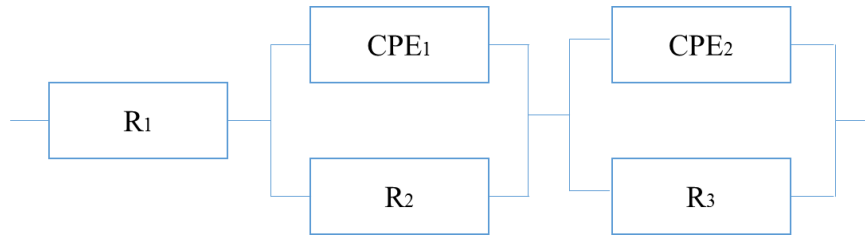


**Figure 37:** Equivalent circuit used for the fitting of the Nyquist plot.

From this equivalent circuit, the resulting EIS spectrums parameters are calculated through modelization by using the open-source software EIS analyzer. The results can be seen in table 3. As this is a faradaic detection of the parameters, the charge transfer resistances were the ones used to draw the standardization curves.

**Table 3:** Result of the fitting of the Nyquist plots of p53 concentrations.

	0 $\mu\text{g/mL}$ p53	1 $\mu\text{g/mL}$ p53	4 $\mu\text{g/mL}$ p53	7 $\mu\text{g/mL}$ p53	10 $\mu\text{g/mL}$ p53
$R_1$ ( $\Omega$ )	38.504	38.51	37.549	36.86	36.384
$R_2$ ( $\Omega$ )	3204.4	1658.3	1348	1188.8	1169.7
$R_3$ ( $\Omega$ )	9197	12822	13850	14812	17021
$Q_1$ ( $s^n \Omega^{-1}$ )	0.000006	0.000005	0.000005	0.000005	0.000005
$n_1$	0.79703	0.84012	0.8318	0.8314	0.82979
$Q_2$ ( $s^n \Omega^{-1}$ )	0.000021	0.000041	0.000045	0.000048	0.000045
$n_2$	0.74123	0.68165	0.66873	0.66406	0.67061
Fitting error	0.00013	0.00027	0.00017	0.00015	0.00016

From the fitting we can see that only  $R_3$  shows a continuous and linear increase from anti-p53 antibody measurement to the final p53 concentration, as such, it is used for the analysis. The analysis is done through normalization of the results following equation 3.1.

$$\Delta R/R = \frac{|R_{p53} - R_{\text{anti-p53}}|}{R_{\text{anti-p53}}} \quad 3.1$$

The normalization allows us to remove the differences between different measurements on different electrodes, which allows us to compare multiple analyses and conclude a standardization curve which is shown in figure 38.

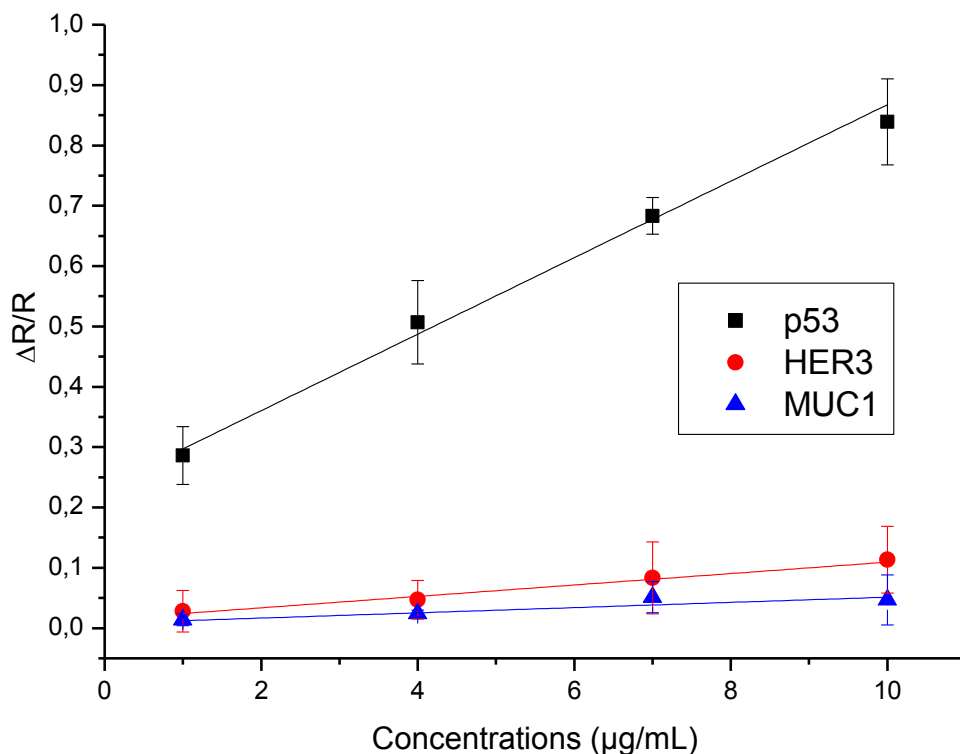


**Figure 38:** Graphical representation of the detection of p53 showing (A) the standardization curves of p53 (black), the interferences HER3 (red) and MUC1 (blue), and their respective equations

Then, the standard deviation was calculated from the normalized results of each concentration after obtaining several EIS measurements of several electrodes.

From these experiments, the resulting standardization curve for p53  $Y = (0.0634 \pm 0.0080) X + (0.2337 \pm 0.0503)$  / R-square = 0.9922 showed greater sensitivity than that of the interference molecules of HER3  $Y = (0.0095 \pm 0.0068) X + (0.0147 \pm 0.0034)$  / R-square = 0.9602 and MUC1  $Y = (0.0043 \pm 0.0030) X + (0.0080 \pm 0.012)$  / R-square = 0.8025. This shows that the developed biosensor is selective to p53 when compared to that of the interference. The error calculation on the graph are the results of the standard deviation calculated after taking all the repeated measurements into account.

### 3.3.3 Detection of p53 using Bradford.

The detection of p53 was then confirmed using Bradford assay. Bradford assay is a total protein assay used to quantify the amount of protein in a biological sample. However, Bradford has a limit of detection in the order of 1  $\mu\text{g/mL}$  protein concentration, as such it was only used in the detection of p53 as it is the only protein found in saliva at this concentration. The aim of using Bradford is to find physical evidence for the bio-recognition process to confirm the electrochemical signal. This is done by comparing the resulting signal obtained before incubating the p53 solution after incubating the p53 solution.

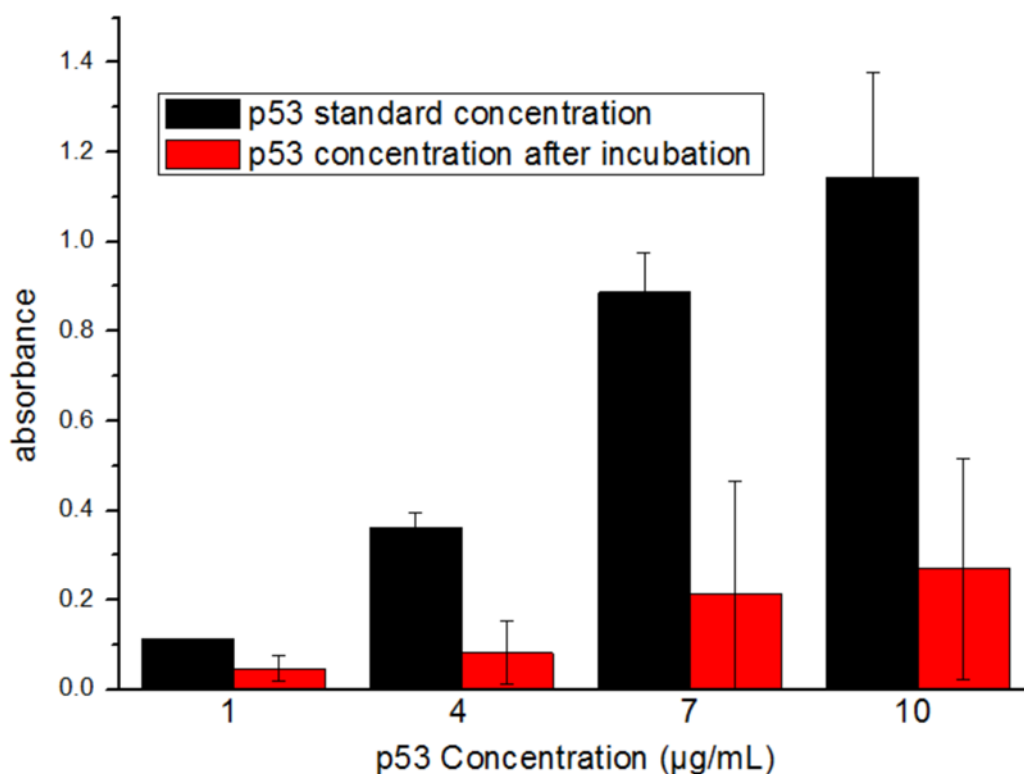


**Figure 39:** Absorbance of the Bradford assay for each p53 concentration before and after incubation on the electrode's surface.

The results, seen here in figure 39, shows that the solution concentration before incubation has a higher absorbance than that of the solution after incubation, indicating a high level of p53 absorbance for each concentration on the electrode surface, and thus, confirming that the change to EIS

spectrum is due to p53 absorbance on the electrode's surface. The graph errors are obtained by calculating the standard deviation of all the repeats.

### 3.3.4 Detection of p53 in artificial saliva.

The primary function of the developed biosensor is its ability to work in a complex medium such as saliva which it is being developed for. As such, the most appropriate technique used for p53 detection in the saliva is the standard addition method; an analytical technique that is developed for the measurement and study of molecules in biological samples.

The main purpose to use artificial saliva instead of real saliva is the control over p53 concentrations which allows the study of the effect such a complex medium has on the device's surface. The result of this detection can be seen in figure 40.

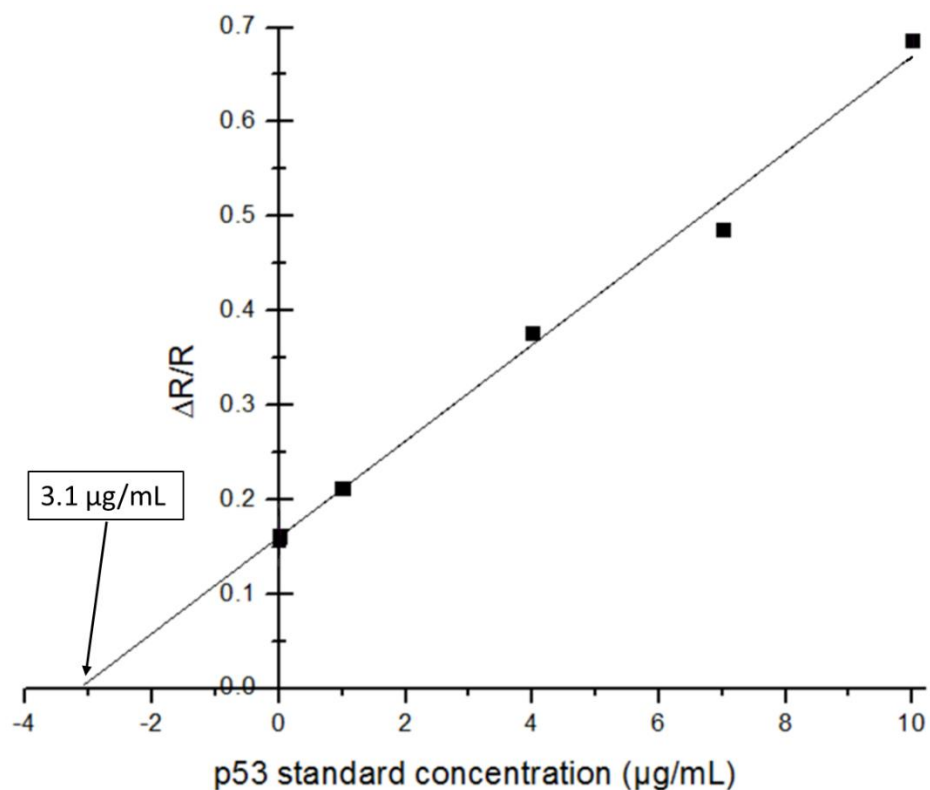


**Figure 40:** detection of p53 in artificial saliva using the standard addition method.

The result of this detection is a standard detection curve:

$Y = 0.0509 X + 0.1606$  with a linearity of R-square = 0.9902. The resolution of the standard addition method is a concentration of 3.1  $\mu\text{g/mL}$  which by following the equation 2.2 found in the previous chapter and replacing the EGFR concentration with that of the p53 is an accuracy of 96.8% of the prepared solution's p53 concentration. When compared to other results found in the literature in table 4, the sensor manages to detect p53 at its salivary concentration with high accuracy in addition to it being the only biosensor that has been developed for the detection of the salivary concentration of p53.

**Table 4:** List of p53 biosensors, their assay types, detection techniques, optimization, functional range, the limit of detection, and medium of detection.

Electrode type and materials	Assay type	Detection technique	Optimizations used	Functional range	Limit of detection	Medium of detection	Reference
Gold nanoparticles on a carbon SPE	Competitive assay	LSV*	Biotin-p53 in conjugation to <i>Streptomyces avidinii</i> labeled with alkaline phosphatase	2 nM – 50 nM	0.05 nM	Human plasma	[71]
Gold electrode	Direct assay	SWV** and DPV***	A nanocomposite containing poly L-cysteine, graphene quantum dots and gold nanoparticles	0.000197-0.016 pM (for SWV) and 0.195 - 50pM (for DPV)	0.065 fM	Human plasma and cell lysate	[72]
Glassy carbon electrode	Sandwich assay	DPV	Graphene oxide-gold nanoparticle- biotinylated antibody and HRP labeled antibody	0.2 pM – 200 pM	115 fM	Human serum and cell surface	[73]
Indium tin oxide electrode	Direct assay	EIS	Chitosan-carbon black composite layer	0.01 pg/mL – 2 pg/mL	3 fg/mL.	Human serum	[74]
Disposable carbon nanotube-	Competitive assay	DPV	Alkaline Phosphatase-conjugated secondary Rabbit Anti-Mouse IgG	20 pM - 10 nM	14 pM	urine	[75]

gold nanoparticles modified SPE							
Indium tin oxide electrode	Direct assay	EIS	tetra armed star-shaped poly(glycidylmethacrylate	0.02 pg/mL – 4 pg/mL	7 fg/mL	Human plasma and cell lysate	[76]
Gold SPE	Direct Assay	EIS	-	1 µg/mL – 10 µg/mL	-	Saliva	This chapter

\*Linear Sweep voltammetry (LSV), \*\*Square wave voltammetry (SWV), \*\*\*Differential pulse voltammetry (DPV).

This result lays the foundation for the use of this biosensor for the detection of p53 in the saliva of patients.

### 3.4 Conclusion

We would like to present in this chapter the development of a biosensor for the detection of p53 concentration in saliva for the detection of breast cancer. The biosensor uses CMA to immobilize the antibody anti-p53 on the surface then uses EIS to detect p53 concentration label-free. The biosensor shows greater sensitivity and selectivity toward p53:  $Y = (0.0634 \pm 0.0080) X + (0.2337 \pm 0.0503)$ / R-square = 0.9922 than toward other molecules that can interfere with the detection including HER3:  $Y = (0.0095 \pm 0.0068) X + (0.0147 \pm 0.0034)$ / R-square = 0.9602 and MUC1:  $Y = (0.0043 \pm 0.0030) X + (0.0080 \pm 0.012)$ / R-square = 0.8025. The biorecognition was also proved using Bradford assay by showing the decrease in p53 concentration before and after incubation of the solution on the biosensor. Finally, the biosensor was tested for the detection of p53 in artificial saliva and was proven to detect the biomarker with remarkable linearity (R-square= 0.9902) and precision (Only 3.1% deviation from the prepared concentration).

## **CHAPTER 4**

### **DEVELOPMENT OF A BIOSENSOR FOR THE DETECTION OF HER2**

#### **Objective**

This chapter covers all the results obtained from the technology transfer to Lebanon, as well as the experiments that were carried out in Lebanon. The experiments consisting of first optimizing the electrodeposition of 4-aminobenzoic acid, then using this electrodeposition to detect Human epidermal receptor 2 (HER2). The biosensor's selectivity was tested with epidermal growth factor receptor (EGFR) and human epidermal growth factor 3 (HER3). This was followed by the detection of HER2 in real saliva.

## **4.1 Introduction**

As described in chapters 1 and 2, HER2 is part of the human epidermal receptor family that includes EGFR. However, unlike EGFR, HER2's gene is amplified in 15-20 % of breast cancer patients. This activation affects a lot of the downstream pathways later on, something that will be talked about further ahead, which causes an increase in cancer proliferation [53]. However, what makes HER2 special is that its role in breast cancer was discovered nearly 35 years ago with several drugs discovered to target it since then [77].

In this chapter, we are going to discuss the biological structure, function and clinical importance of HER2

### **4.1.1 Structure of HER2**

HER2's structure is similar to that of other human epidermal receptor families discussed in chapter 2. HER2 specifically is a 185 kDa transmembrane glycoprotein that is encoded by a gene found on chromosome 17q call oncogene HER2/neu. Its structure is also the same as that of EGFR in that it's made of three parts, the amino-terminal found in the extracellular region is made up of two separate binding regions (LD1 and LD2) and two cysteine-rich regions (CR1 and CR2), all this is linked to a transmembrane region rich in hydrophobic amino acids which link to the acid terminal region in the intracellular domain containing a tyrosine kinase catalytic domain with multiple phosphorylation sites [78]. An image of HER2 can be found in figure 41.

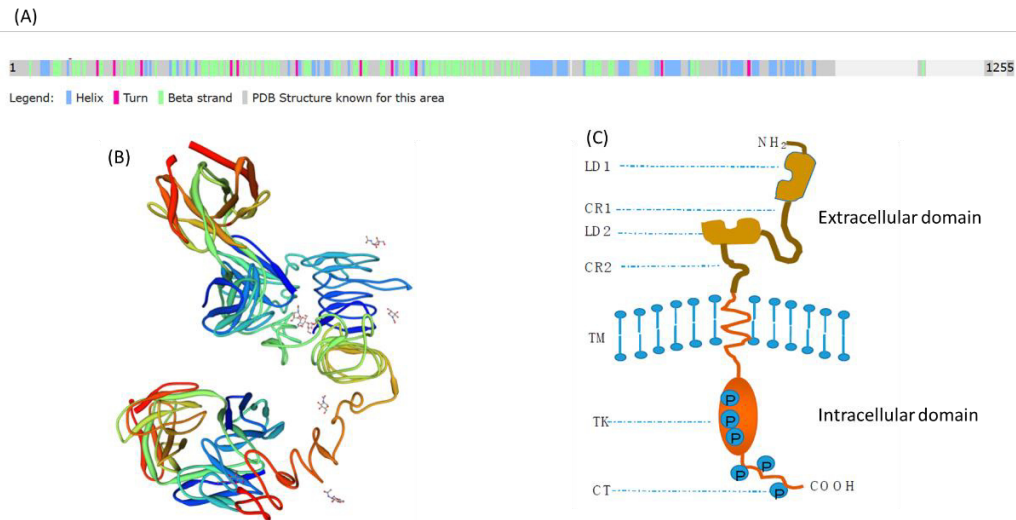


**Figure 41:** (A) HER2 secondary structure (B) HER2 tertiary structure (C) Schematic of HER2 structure [78].

#### 4.1.2 Signaling pathway

The signaling pathway of HER2 differs from that of EGFR explained in chapter 2 in a few key features. The most important difference is that HER2 does not have an identifying ligand, HER2 constitutively exist in an activated conformation. Therefore, HER2 functions are activated by dimerizing preferably with other human epidermal receptor family members with the dimerization with HER3 being the most enzymatically active. Once dimerization occurs, HER2 activates the autophosphorylation function of its tyrosine residue. This phosphorylation in turns enlists adaptor proteins which activate two signaling cascades called phosphatidylinositol 3-kinase (PI3K)-Akt and Ras/Raf/mitogen-activated protein kinase (MAPK). It should be noted that different dimers induce different cascades, however, the PI3K and MAPK signaling pathways are the most studied. In normal functioning cells, the signal pathway is cut off by endocytosis through dimerization with EGFR, this leads to either recycling or degradation of HER2 [52,77,78]. The full signaling pathway is summarized in figure 42.

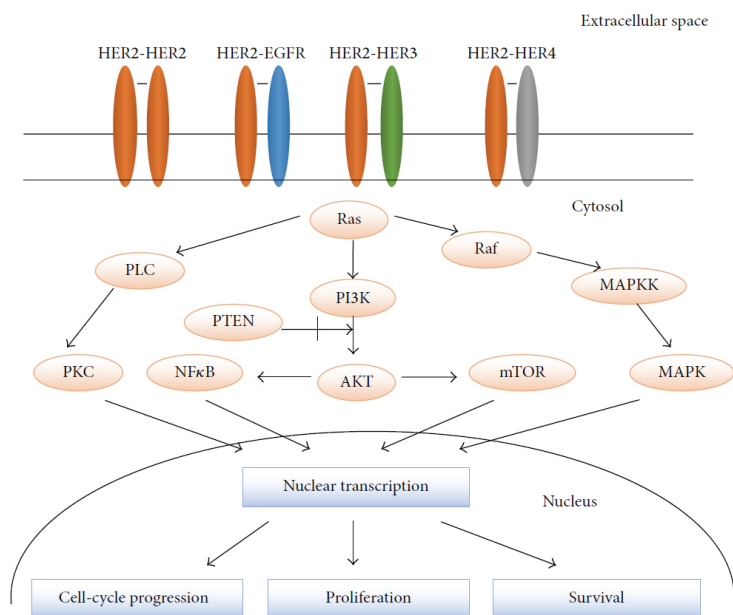


**Figure 42:** Signaling pathways of HER2 dimerization [79].

### 4.1.3 HER2 and breast cancer

With the above information, the role of HER2 in cancer becomes clear. In normal cell function, HER2/neu genes encode an appropriate amount of HER2 for heterodimerization which establishes a normal response of the growth factors that target human epidermal receptors family. In cancer, overexpression of HER2 reaches 10 to 100 times the amount of normal cells, this leads to an excessive amount of HER2-containing heterodimers to form on the cell surface, which amplifies the signal to these growth factors to a greater degree, thus leading to malignant growth and tumorigenesis [78].

In breast cancer, this overexpression occurs in nearly 20% of cases. Breast cancer can increase the number of expressed HER2/neu gene to anywhere between 25 to 40 folds. This results in an increase anywhere between 40 to 100 folds than normal breast cancer tissue, this gives HER2 amplified breast cancer special clinical and biological characteristics such as increased sensitivity to certain cytotoxic agents while being resistant to hormonal agents, and a tendency to metastasize to the brain [77].

One particular mutation to the HER2/neu gene causes it to lose its extracellular domain. This mutation is called p95 and it gives HER2-amplified breast cancer resistance to most of the drugs that target it [79].

In conclusion, HER2-amplification in breast cancer is an indication of poor prognosis and survival [77–79]. The target location for each breast cancer therapy s highlighted in figure 43.

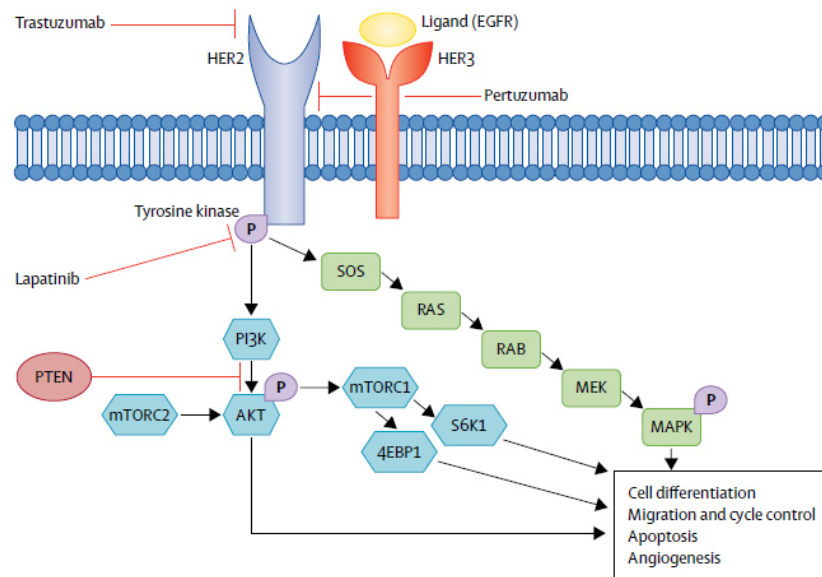


**Figure 43:** Location of trastuzumab drug and lapatinib drug activity in breast cancer [80].

#### 4.1.4 HER2 detection

The most recommended form of detection of HER2 is Immunohistochemistry, however, due to the invasiveness of the technique and due to high levels of error, new techniques have been developed, the most common protein proxy blood test for HER2 is the HERmark test [77]. In saliva, several articles used Enzyme-Linked Immuno-Sorbent Assays for HER2 detection, with a detection concentration being around 25 pg/mL HER2-amplified breast cancer (HER2 in saliva), and around 10 pg/mL for HER2 negative breast cancer. Though in the same article, it concluded that there is no correlation between the salivary concentration of HER2 and its expression in breast cancer tissue, the results can be seen in figure 4.

However, that could also be due to the low concentration of HER2 and the fact that the technique used may not be optimized for the detection of HER2 in saliva in addition to the low number of participants in the study which casts doubt on the validity of said results shown in figure 44 [81,82].

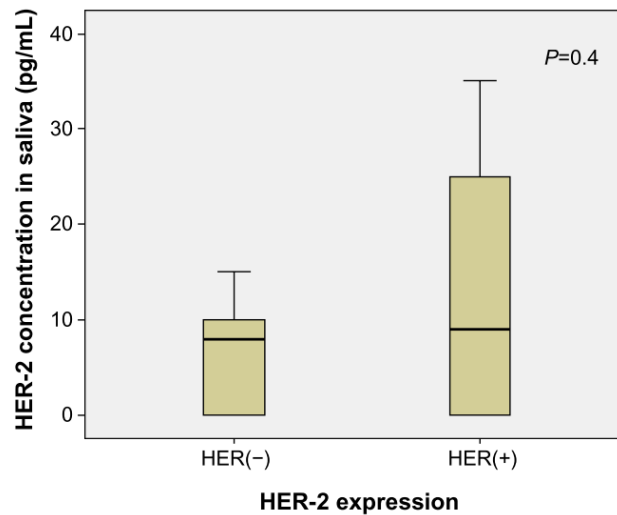


**Figure 44:** salivary HER2 concentration in relation to HER2 tissue expression in breast cancer [82].

## 4.2 Materials and methods

### 4.2.1 Materials

All chemical reagents were purchased from Sigma Aldrich and they are:

- sodium nitrite ( $\text{NaNO}_2$ ),
- hydrochloric acid (HCl),
- ethanolamine,
- Phosphate buffer saline solution (PBS),
- N-hydroxysuccinimide (NHS),
- potassium Ferrocyanide,
- potassium Ferry cyanide trihydrate,
- 4-aminobenzoic acid (ABA)

The product that was bought from Carl Roth were:

- N-(3-dimethylaminopropyl)-N-ethyl-carbodiimide hydrochloride (EDC),

All biological compounds were purchased from R&D system:

- Anti-HER2 antibody
- EGFR antigen
- HER2 antigen
- HER3 antigen

The equipment used is as follows:

- Palmsens 4

Real saliva was obtained by passive drooling in a sterilized cup from a healthy 28-year-old male volunteer after breakfast at 10 am.

The electrodes used were fully described in appendi A.

## 4.2.2 Methods

### 4.2.2.1 ABA electrodeposition

The electrodeposition of ABA was the first step performed in the functionalization of the SPE. This electrodeposition was performed by:

- Dissolution of 5 mM ABA in a solution of 0.5 M HCl
- Activation of ABA solution by adding 5 mM solution of NaNO<sub>2</sub> to the mixture.
- Incubating the activated ABA solution for 5 min in ice.
- Electrodeposition of ABA using the following CV parameters:
  - Scan rate: 100 mV/s
  - Potential window: -0.4 to 0.4 V
  - The number of scans: 15 cycles.

It should be mentioned that the electrodeposition of ABA was optimized. The optimization of ABA was described in the supplementary materials under the title optimization of ABA electrodeposition.

#### 4.2.2.2 Anti-HER2 antibody immobilization

The immobilization of the anti-HER2 antibody was done through the following steps without a microfluidic system:

- Incubation of the SPE with the electrodeposited ABA in EDC (0.4M) / NHS (0.1 M) in deionized water for 40 min.
- Washing the SPE with 1 mL of PBS
- Incubation of the SPE in anti-HER2 antibody (10  $\mu\text{g}/\text{mL}$ ) for 40 min.
- Washing the SPE in 1 mL PBS and putting it inside the microfluidic system
- Incubation of the SPE in 1/1000 solution of Ethanolamine in PBS.
- Washing the electrode in PBS
- Characterizing the electrode using EIS.

#### 4.2.2.3 Characterization methods:

Two methods of characterization were implemented EIS and CV.

##### 4.2.2.3.1 Characterization using EIS

The characterization using EIS was done through the following steps at room temperature:

- Filling the microfluidic cell with Fe(II)/Fe(III) 5mM in PBS solution
- Measuring the SPE using the following parameters
  - $E_{dc} = 0.172 \text{ V}$
  - $E_{ac} = 10 \text{ mV}$
  - Frequency window: 10000 to 0.5 Hz
  - Number of repeats: 10 times

This is usually followed by washing the SPE with a PBS solution.

#### **4.2.2.3.1 Characterization using CV**

The characterization using CV is done using the following steps at room temperature:

- Filling the microfluidic cell with Fe(II)/Fe(III) 5mM in PBS solution.
- Measuring the CV with the following parameters
  - The scan rate of 0.8 V/s
  - Potential window: from -0.4 to 0.6 V
  - Number of scans: 3 scans

#### **4.2.2.4 Measurement of HER2, EGFR, and HER3 concentration in PBS**

The protein concentrations are made by diluting the appropriate amount of the stock solutions in PBS. The measurement of protein concentrations (5 pg/mL, 10 pg/mL, 20 pg/mL, 40 pg/mL) follow these steps:

- First, the microfluidic cell is cleaned with the electrode inside with 1 mL PBS,
- The lowest standard concentration protein is introduced inside the cell for 30 min.
- After which cell is cleaned using 1 mL PBS solution,
- Then EIS measurements are performed per part 4.2.2.3.1.
- The cell is then cleaned with PBS before introducing the higher concentration and repeating the steps above.

#### **4.2.2.5 Measurement of HER2 in real saliva**

The standard addition method was done with a sample of real saliva. The standard solution of HER2 of 1 ng/mL was prepared by diluting the stock HER2 (50 µg/mL) solution in the real saliva sample.

This solution of HER2 in saliva was then used to create the pre-determined concentration of HER2 of 10 pg/mL by diluting it with the standard HER2 concentrations in PBS.

### 4.3 Results

#### 4.3.1 ABA electrodeposition

The electrodeposition of ABA was fully explored in Appendix D.

#### 4.3.2 Measurement of HER2 concentration in PBS.

EIS characterization was carried out after each concentration of protein biomarkers. The results can be displayed in either the Nyquist plot or Bode plot, however. The result of the measurement of HER2 concentrations in Nyquist can be found in figure 45.

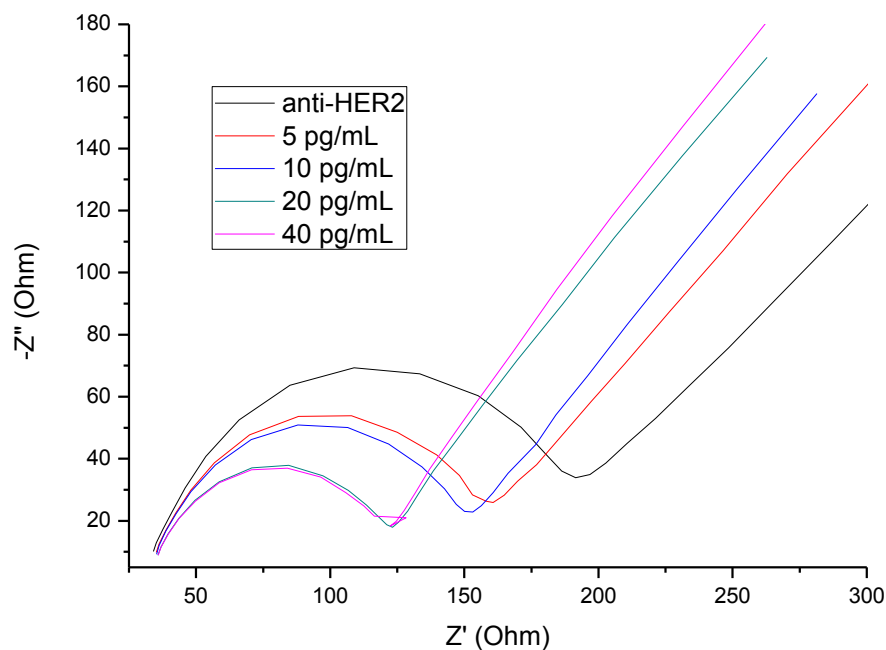


**Figure 45:** Nyquist plot showing the measurements of the different concentrations of HER2 starting with the Nyquist from the immobilization of anti-HER2 antibodies

(black), then 5 pg/mL HER2 (red), 10 pg/mL HER2 (blue), then 20 pg/mL HER2 (green), then finally 40 pg/mL HER2 (magenta).

The Nyquist plot shows the real impedance versus the imaginary impedance. The measurement of HER2 concentration shows two distinctive parts, a large semicircle in the beginning and a smaller semicircle in the end. As described in chapter 1, 2, and 3. This is typical for a porous electrode, however, due to the use of ABA instead of 4-aminophenyl acetic acid, the shape of the holes formed is different causing a change in the form of the semicircle [31], this form is better registered with the use of the Bode plot figure 46.

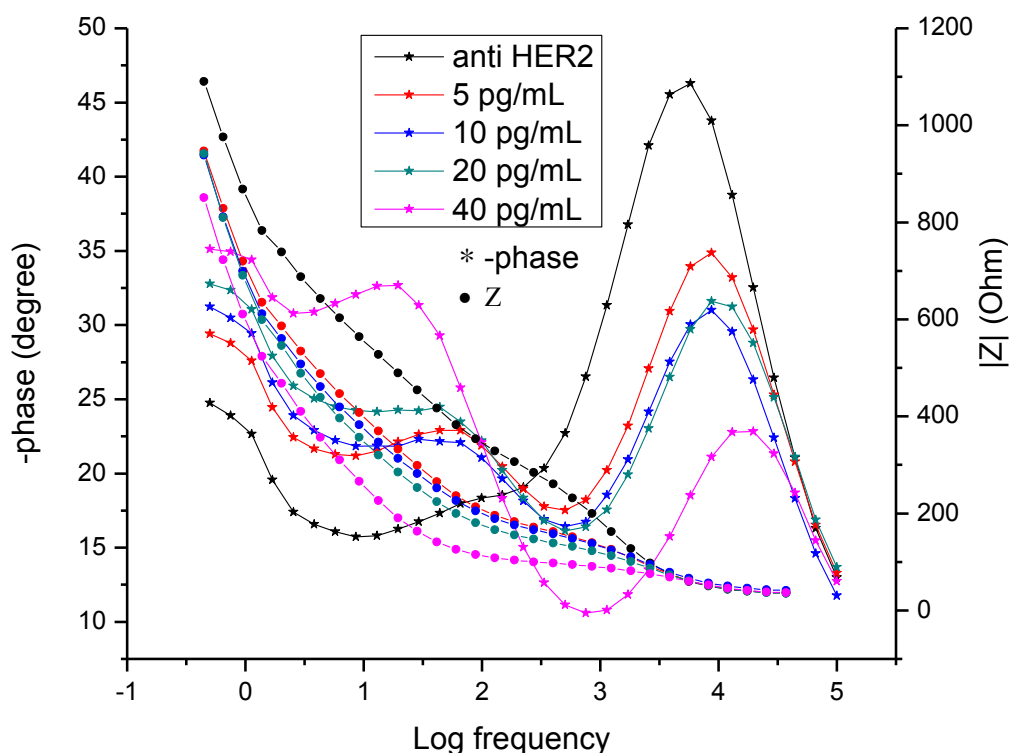


**Figure 46:** Bode plot showing the impedance Bode in dots and the phase degree shift in stars versus the logarithm of the frequencies for the EIS measurements of HER2 concentrations starting with the immobilization of anti-HER2 antibodies (black), then 5 pg/mL HER2 (red), 10 pg/mL HER2 (blue), then 20 pg/mL HER2 (green), then finally 40 pg/mL HER2 (magenta).

The Bode plot shows three distinct parameters, the logarithm of the frequency versus the phase shift versus the total impedance. This results in two distinct overlapping plots and often provides information regarding the nature of the detection. In the Bode plot, the measurement of HER2 concentration shows a divide into two distinct parts the same as in the Nyquist plot. The first part, which coincides with the high frequencies (From  $\log(f)$  of 5 to 1.5), shows high and inconsistent levels of variations of the phase shifts in regards to the concentration of HER2, while at the lower end of the frequency range (below  $\log(f)$  of 1.5) the phase shift consistently increased with the increase in HER2 concentration. With the total impedance, however, we see two steps, the first in the high frequency ( $\log(f)$  between 5 and 3) range shows no difference between the concentration of HER2, then in the lower frequency (below  $\log(f)$  of 3), the total impedance increases with the concentration of HER2.

From these observations, we can conclude that the concentration of HER2 is mostly detected in the lower frequency. As such, when performing the fitting using the equivalent circuit discussed in chapters 1, 2, and 3 for porous electrodes and found in figure 47.

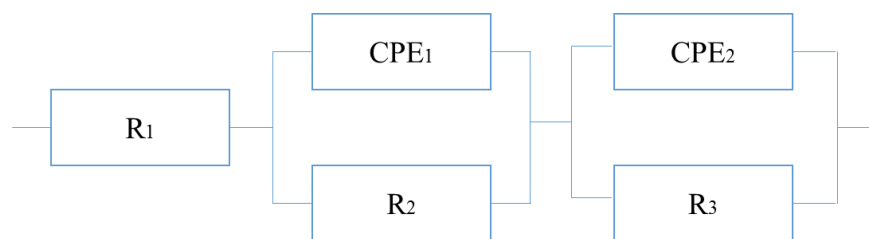


**Figure 47:** Equivalent circuit used for the modelization of the measurement of HER2 concentrations.

The charge transfer resistance used is  $R_3$  which is the resistance for the lower frequency detection and the one whose values correlates well with the concentrations of HER2 as seen in table 5.

**Table 5:** resulting parameters from the modelization of HER2 detection.

	<b>0 pg/mL</b>	<b>5 pg/mL</b>	<b>10 pg/mL</b>	<b>20 pg/mL</b>	<b>40 pg/mL</b>
	<b>HER2</b>	<b>HER2</b>	<b>HER2</b>	<b>HER2</b>	<b>HER2</b>
<i>R1</i> ( $\Omega$ )	24.39	32.9	38.59	32.69	33.99
<i>R2</i> ( $\Omega$ )	170.78	87.93	84.88	85.54	60.61
<i>R3</i> ( $\Omega$ )	822.18	800.05	726.89	610.6	516.42
<i>Q2</i> ( $s^n\Omega^{-1}$ )	0.00000066	0.00000074	0.00000093	0.0000012	0.0000019
<i>n2</i>	0.97896	0.95149	0.92472	0.89392	0.83093
<i>Q3</i> ( $s^n\Omega^{-1}$ )	030002	0.00025	0.00025	0.00019	0.00015
<i>n3</i>	0.4665	0.5146	0.5282	0.6027	0.7511
<i>Fitting error</i>	0.00037	0.0003	0.00018	0.000089	0.000062

From this conclusion, the resulting resistance values are then normalized following equation 4.1. The values obtained are then used to create the standardization curve for the detection of HER2 found in figure 48.

$$\Delta R/R = \frac{|R_{\text{HER2}} - R_{\text{anti-HER2}}|}{R_{\text{anti-HER2}}} \quad 4.1$$

The standardization curve for HER2 had the following equation:

$Y = (0.0055 \pm 0.0003) X + (0.1127 \pm 0.0052)$  \ R-square = 0.9909. This was followed by detection of interference molecules:

HER3  $Y = (0.0020 \pm 0.0169) X + (0.0530 \pm 0.0151)$  \ R-square = 0.1302 and

EGFR  $Y = (0.0018 \pm 0.0005) X + (0.0166 \pm 0.0049)$  \ R-square = 0.8072.

The detection of HER2 showed a higher level of sensitivity and linearity than that of the interferences EGFR and HER3, proving that the biosensor is selective to HER2.

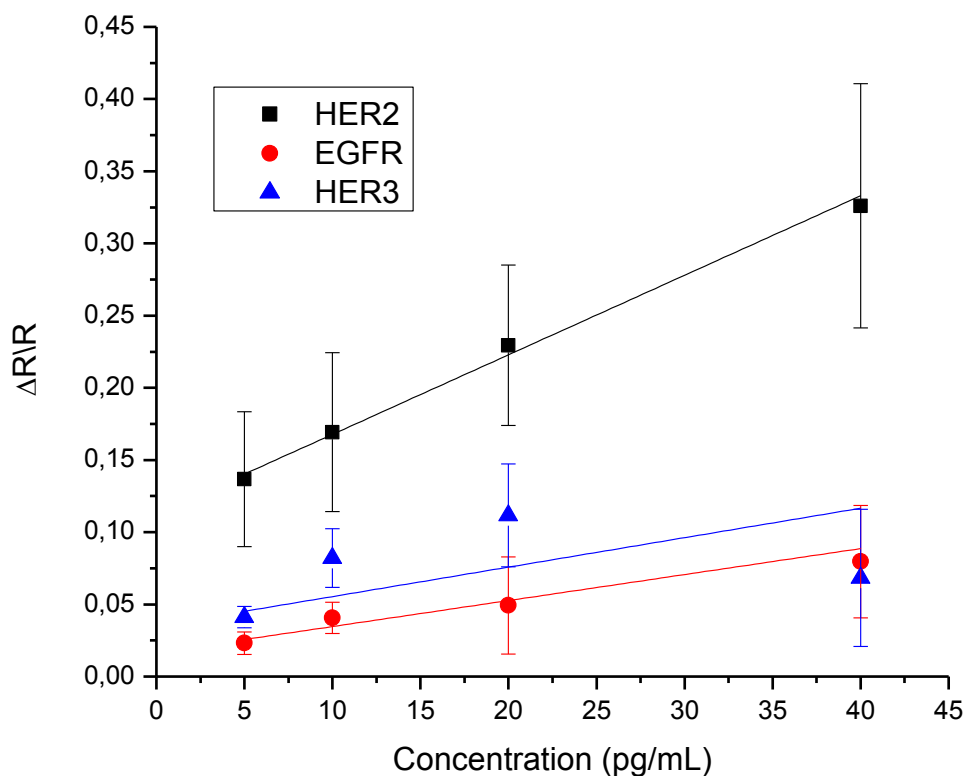


**Figure 48:** Standardization curves for the detection of HER2 (black) with the detection of the interference proteins EGFR (red) and HER3 (blue).

### 4.3.3 Measurement of HER2 concentration in real saliva.

The standard addition method was used for the detection of a predetermined concentration of HER2 that was diluted in real saliva of a healthy 28-year-old male volunteer. The standard addition method is generally used for the detection of analytes in complex matrixes such as biological samples. The purpose of this detection is to show as a proof of concept that the salivary matrix effect does not affect the overall detection of HER2.

The detection of HER2 using standard addition method has yielded the curve seen in figure 49. The curve has an equation of  $Y = 0.0118 X + 0.1282$  with a linearity of  $R\text{-square} = 0.9876$ , thus calculating a concentration of 10.8 pg/mL. Thus, by applying Equation 2.2 gives it an accuracy of 92.59%.

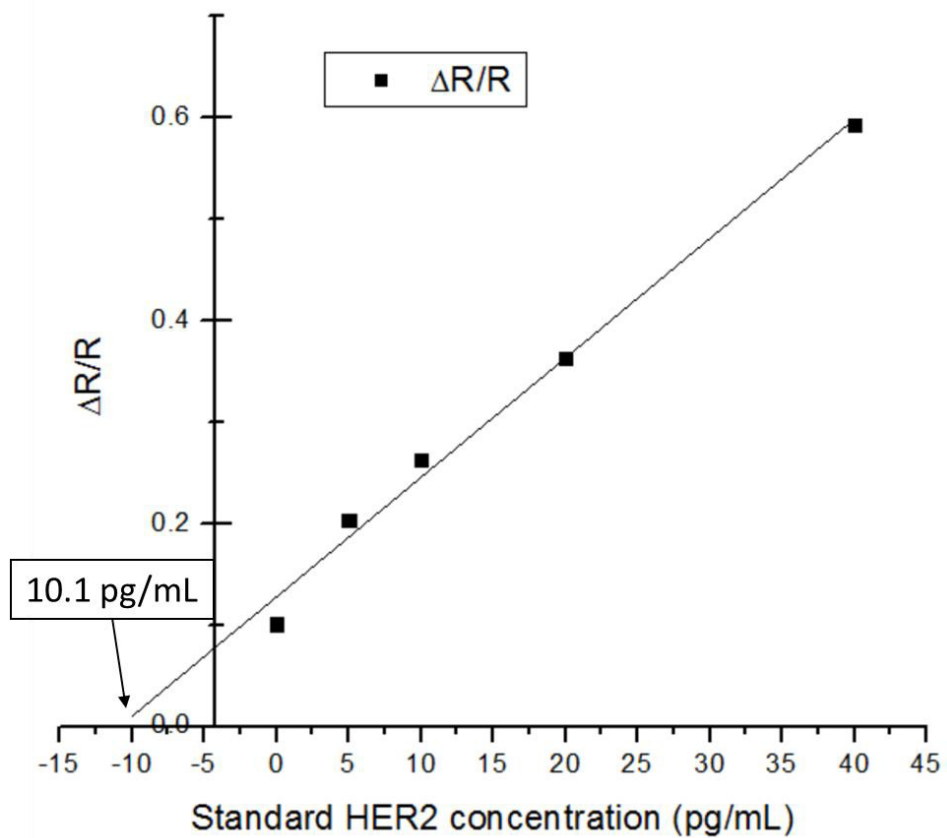


**Figure 49:** Detection of HER2 concentration in real saliva using the standard addition method.

When compared to current literature on the subject, the current biosensor offers a simple, easy to use method for detection that is geared toward salivary detection, while other biosensors found in table 6 are only optimized for the detection of HER2 in serum.

**Table 6:** List of biosensors for the detection of HER2.

<b>Electrode materials used</b>	<b>Electrochemical technique</b>	<b>Amplification strategy</b>	<b>Limit of detection</b>	<b>Medium of detection</b>	<b>reference</b>
Gold electrode	DPV	tetrahedral DNA nanostructures aptamer as recognition probe with flower-like nanozymes (MnO <sub>2</sub> ) HRP as signal nanoprobe decorated with aptamer 2	0.08 ng/mL	Serum	[83]
Ink-jet gold electrode	Amperometry	Sandwich assay with HRP bound to biotinylated antibodies	12 pg/mL	Serum	[84]
Organic electrochemical transistor	Amperometry, CV	HRP nanoprobe	10 fg/mL	Serum	[85]
Screen-printed carbon electrode	DPV	Cd quantum dot nanoprobe	2.1 ng/mL	Serum	[86]
Carbon electrode	LSV	Gold nanoparticle	2.9 ng/mL	Serum	[87]

Glassy carbon electrode	DPV	Magnetic nanoparticles as a recognition probe with gold and silver nanoparticles as signaling probe	0.02 pg/mL	Serum	[88]
Carbon electrode	CV	Gold nanoparticles conjugated with mal	10.2 pg/mL	Serum	[89]
Screen printed carbon electrode	LSV	Cerium oxide nanoparticles	34.9 pg/mL	Serum	[90]
screen-printed carbon electrodes	EIS	Zwitterion hydrogel and lectin-based glycol-profiling	5 pg/mL	Serum	[91]

DPV: differential pulse voltammetry/ HRP horseradish peroxidase/ LSV: Linear sweep voltammetry

#### **4.4 Conclusion**

In this chapter, we have discussed the development of a biosensor for the detection of salivary HER2 concentration. First, the biosensor was optimized before detecting HER2 concentration using electrochemical impedance spectroscopy. The fitting and normalization of the resulting measurements create the standardization curve. From here the biosensor showed its selectivity toward HER2 by double the sensitivity toward it than toward the interference molecules HER3 and EGFR. This is then followed the detection of HER2 in real saliva using the standard addition method. The biosensor can detect HER2 in its physiological concentration, despite that many biosensors can detect in that concentration, this is the first biosensor that is optimized for salivary HER2 concentration detection.

## CONCLUSION AND PERSPECTIVE

To surmise, three biosensors for the detection of salivary breast cancer biomarkers have been developed. The first biosensor is for the detection of salivary EGFR. The biosensor was first developed using SPE microarray where CMA was deposited on the surface of its gold working electrode. This is followed by the immobilization of the anti-EGFR antibody on its surface using EDC/NHS. The biosensor was then used for the detection of EGFR protein in PBS using EIS. The biosensor proved to be selective for EGFR with a sensitivity to be 40 times higher than that of HER2 and 7 times higher for HER3. The effect of the artificial salivary matrix proved to be inconsequential below 100 times dilution, and the biosensor was able to detect EGFR in artificial saliva with 97 % accuracy using the standard addition method.

The second biosensor developed was for the detection of a salivary concentration of p53. The biosensor used CMA electrodeposition and EDC/NHS linkers to immobilize the anti-p53 antibody on the surface. p53 concentrations in PBS were detected using EIS. The biosensor detected p53 with a sensitivity that is 7 times higher than that of HER3 and 15 times higher than that of MUC1 proving its selectivity toward its target biomarker. The detection of p53 was further tested using Bradford's total protein assay where the concentration of p53 in PBS fell after incubating it on the biosensor. The biosensor was then used for the detection of p53 concentration in artificial saliva with a 96% accuracy using the standard addition method.

The third biosensor developed was for the detection of the salivary concentration of HER2. The biosensor used ABA electrodeposition and

EDC/NHS linkers to immobilize the anti-HER2 antibody on the surface of the SPE. The concentration of HER2 in PBS was then detected using EIS. The biosensor's sensitivity toward HER2 was 3 times higher than both HER3 and EGFR, proving its sensitivity. The biosensor was then able to detect HER2 concentration in real saliva with 92% accuracy using the standard addition method.

The aim of this project is to develop a bio-analytical tool for the detection of salivary breast cancer biomarkers, and with the results presented in this thesis, we can conclude that great strides have been made toward this goal. However, much work remains. The first part is to develop a biosensor for the remaining salivary protein biomarker for breast cancer MUC1. The second is the optimization of the functionalization by providing a direct comparison study of the effects of using CMA or ABA molecules for the electrodeposition, and finally, by optimizing the detection process to involve as fewer steps as possible to mitigate procedural errors, this can be done by changing the shape of the EIS plots, or by testing different electrochemical methods for a simplified data analysis, or development of a pre-concentration protocol instead of the standard addition method to mitigate the multi-step detection process.

Once the development of the bioanalytical tool is complete, we can then tackle the major issue regarding the small number of publications related to the topic of salivary breast cancer biomarker detection. As it stands, the number of publications and the pool of breast cancer patients whose salivary biomarkers were tested remains too low and the evidence remains too conflicted regarding the use of saliva as an alternative for blood.

Saliva is a great alternative for blood analysis as it contains all the blood biomarkers but without the inconvenience of invasiveness and safety, however, due to its matrix effects, saliva is seen as unreliable when compared

to blood analysis. This research is a step in the right direction in making saliva a more prominent medium for clinical analysis.

## ARTICLES PUBLISHED

Abrao Nemeir, I.; Saab, J.; Hleihel, W.; Errachid, A.; Zine, N. Impedimetric label-free detection of salivary EGFR on screen printed electrode. *Integr. Cancer Sci. Ther.* **2019**, *6*, 1–3.

Nemeir, I.A.; Saab, J.; Hleihel, W.; Errachid, A.; Zine, N. Salivary Protein Antigens for Breast Cancer Biomarkers. **2019**, *1*, 24–30.

Abrao Nemeir, I.; Saab, J.; Hleihel, W.; Errachid, A.; Jafferzic-Renault, N.; Zine, N. The Advent of Salivary Breast Cancer Biomarker Detection Using Affinity Sensors. *Sensors* **2019**, *19*, 2373.

Zouaoui, F.; Bourouina-Bacha, S.; Bourouina, M.; Abrao-Nemeir, I.; Ben Halima, H.; Gallardo-Gonzalez, J.; El Alami El Hassani, N.; Alcacer, A.; Bausells, J.; Jaffrezic-Renault, N.; et al. Electrochemical impedance spectroscopy determination of glyphosate using a molecularly imprinted chitosan. *Sensors Actuators B Chem.* **2020**, *309*, 127753.

Zea, M.; Moya, A.; Abrao-Nemeir, I.; Gallardo-Gonzalez, J.; Zine, N.; Errachid, A.; Villa, R.; Gabriel, G. All Inkjet Printing Sensor Device on Paper: for Immunosensors Applications. In Proceedings of the 2019 20th International Conference on Solid-State Sensors, Actuators and Microsystems & Eurosensors XXXIII (TRANSDUCERS & EUROSENSORS XXXIII); **2019**; pp. 2472–2475.

Abrao Nemeir, I.; Saab, J.; Hleihel, W.; Errachid, A.; Jafferzic-Renault, N.; & Zine, N. Impedimetric Label-Free Immunosensor for the Detection of Salivary p53 Breast Cancer Biomarker on Screen Printed Electrodes. *Eurosensors XXXVI*; **2021**; under submission

Abrao Nemeir, I.; Mouawad, L.; Saab, J.; Hleihel, W.; Errachid, A.; & Zine, N. Label-free Detection of HER2 in Saliva on Screen Printed Electrodes Using Electrochemical Impedance Spectroscopy. *Biosensors*; **2020**; under submission.

**CONFERENCE ATTENDED**

32nd Eurocongress on Cancer Science and Therapy (03/2019 – 03/2019),  
Barcelona. Conference series, Cancer Science and Therapy

Euroensors XXXIV Conference, Lecce.

The 1st International Electronic Conference on Biosensors, (02/11/2020-  
17/11/2020), online

## REFERENCES

1. Abrao Nemeir, I.; Saab, J.; Hleihel, W.; Errachid, A.; Jafferzic-Renault, N.; Zine, N. The Advent of Salivary Breast Cancer Biomarker Detection Using Affinity Sensors. *Sensors* **2019**, *19*, 2373.
2. Sabel, M.S. Principles of Breast Cancer Screening. In *Essentials of Breast Surgery*; Elsevier, 2009; pp. 19–40.
3. Greabu, M.; Battino, M.; Mohora, M.; Totan, A.; Didilescu, A.; Spinu, T.; Totan, C.; Miricescu, D.; Radulescu, R. Saliva--a diagnostic window to the body, both in health and in disease. *J. Med. Life* **2009**, *2*, 124–32.
4. Nemeir, I.A.; Saab, J.; Hleihel, W.; Errachid, A.; Zine, N. Salivary Protein Antigens for Breast Cancer Biomarkers. **2019**, *1*, 24–30.
5. Porto-Mascarenhas, E.C.; Assad, D.X.; Chardin, H.; Gozal, D.; De Luca Canto, G.; Acevedo, A.C.; Guerra, E.N.S. Salivary biomarkers in the diagnosis of breast cancer: A review. *Crit. Rev. Oncol. Hematol.* **2017**, *110*, 62–73.
6. Chiu, M.L.; Lawi, W.; Snyder, S.T.; Wong, P.K.; Liao, J.C.; Gau, V. Matrix Effects-A Challenge Toward Automation of Molecular Analysis. *JALA - J. Assoc. Lab. Autom.* **2010**, *15*, 233–242.
7. Malcovati, P.; Baschiroto, A.; d'Amico, A.; Natale, C. Sensors and microsystems. In *Proceedings of the AISEM 2009 Proc.*, Springer; Springer, 2010.
8. Luka, G.; Ahmadi, A.; Najjaran, H.; Alocilja, E.; DeRosa, M.; Wolthers, K.; Malki, A.; Aziz, H.; Althani, A.; Hoorfar, M. Microfluidics Integrated Biosensors: A Leading Technology towards

- Lab-on-a-Chip and Sensing Applications. *Sensors* 2015, 15.
9. Schmickler, W.; Santos, E. *Interfacial electrochemistry*; Springer Science & Business Media, 2010; ISBN 3642049370.
  10. Lefrou, C.; Fabry, P.; Poignet, J.-C. *Electrochemistry: the basics, with examples*; Springer Science & Business Media, 2012; ISBN 3642302505.
  11. Bard, A.J.; Faulkner, L.R. Fundamentals and applications. *Electrochem. Methods* **2001**, 2, 580–632.
  12. Mishra, R.K.; Nunes, G.S.; Souto, L.; Marty, J.L. Screen Printed Technology—An Application Towards Biosensor Development. *Encycl. Interfacial Chem.* **2018**, 487–498.
  13. Michalska, A.; Kisiel, A.; Maksymiuk, K. Screen-printed disposable reference electrodes. In *Handbook of Reference Electrodes*; Springer, 2013; pp. 325–330.
  14. Kim, J.; Kumar, R.; Bandodkar, A.J.; Wang, J. Advanced Materials for Printed Wearable Electrochemical Devices: A Review. *Adv. Electron. Mater.* **2017**, 3, 1–15.
  15. Ahmed, M.U.; Hossain, M.M.; Safavieh, M.; Wong, Y.L.; Rahman, I.A.; Zourob, M.; Tamiya, E. Toward the development of smart and low cost point-of-care biosensors based on screen printed electrodes. *Crit. Rev. Biotechnol.* **2016**, 36, 495–505.
  16. Wang, J.; Musameh, M. Carbon nanotube screen-printed electrochemical sensors. *Analyst* **2004**, 129, 1–2.
  17. Sekar, N.C.; Shaegh, S.A.M.; Ng, S.H.; Ge, L.; Tan, S.N. A paper-based amperometric glucose biosensor developed with Prussian Blue-modified screen-printed electrodes. *Sensors Actuators B Chem.* **2014**, 204, 414–420.
  18. Cinti, S. Polymeric materials for printed-based electroanalytical (Bio) applications. *Chemosensors* **2017**, 5, 31.

19. Climent, V.; Feliu, J.M. Cyclic voltammetry. **2018**.
20. Srivastava, A.K.; Upadhyay, S.S.; Rawool, C.R.; Punde, N.S.; Rajpurohit, A.S. Voltammetric techniques for the analysis of drugs using nanomaterials based chemically modified electrodes. *Curr. Anal. Chem.* **2019**, *15*, 249–276.
21. Elgrishi, N.; Rountree, K.J.; McCarthy, B.D.; Rountree, E.S.; Eisenhart, T.T.; Dempsey, J.L. A practical beginner's guide to cyclic voltammetry. *J. Chem. Educ.* **2018**, *95*, 197–206.
22. Zhao, G.; Wang, H.; Liu, G. Recent advances in chemically modified electrodes, microfabricated devices and injection systems for the electrochemical detection of heavy metals: A review. *Int. J. Electrochem. Sci* **2017**, *12*, 8622–8641.
23. Opallo, M.; Lesniewski, A. A review on electrodes modified with ionic liquids. *J. Electroanal. Chem.* **2011**, *656*, 2–16.
24. Yáñez-Sedeño, P.; Campuzano, S.; Pingarrón, J.M. Integrated affinity biosensing platforms on screen-printed electrodes electrografted with diazonium salts. *Sensors (Switzerland)* **2018**, *18*.
25. Cao, C.; Zhang, Y.; Jiang, C.; Qi, M.; Liu, G. Advances on Aryldiazonium Salt Chemistry Based Interfacial Fabrication for Sensing Applications. *ACS Appl. Mater. Interfaces* **2017**, *9*, 5031–5049.
26. Gilbraith, W.; Booksh, K.S. Strategies for Designing Chemical Functionalities for Biochemical Sensing With Diazonium Salts. *Encycl. Interfacial Chem.* **2018**, 517–523.
27. Hermanson, G.T. *Bioconjugate techniques*; Academic press, 2013; ISBN 0123822408.
28. Felix, F.S.; Angnes, L. Electrochemical immunosensors – A powerful tool for analytical applications. *Biosens. Bioelectron.* **2018**, *102*, 470–478.

29. Ciucci, F. Modeling Electrochemical Impedance Spectroscopy. *Curr. Opin. Electrochem.* **2018**, *13*, 132–139.
30. Zhu, S.; Sun, X.; Gao, X.; Wang, J.; Zhao, N.; Sha, J. Equivalent circuit model recognition of electrochemical impedance spectroscopy via machine learning. *J. Electroanal. Chem.* **2019**, *855*, 113627.
31. Lasia, A. *Electrochemical impedance spectroscopy and its applications*; 2014; Vol. 9781461489; ISBN 9781461489337.
32. Macdonald, J.R.; Barsoukov, E. Impedance spectroscopy: theory, experiment, and applications. *History* **2005**, *1*, 1–13.
33. Huang, J.; Li, Z.; Liaw, B.Y.; Zhang, J. Graphical analysis of electrochemical impedance spectroscopy data in Bode and Nyquist representations. *J. Power Sources* **2016**, *309*, 82–98.
34. Huang, J. Diffusion impedance of electroactive materials, electrolytic solutions and porous electrodes: Warburg impedance and beyond. *Electrochim. Acta* **2018**, *281*, 170–188.
35. Vieira, D.S.; Fernandes, P.R.G.; Mukai, H.; Zola, R.S.; Lenzi, G.G.; Lenzi, E.K. Surface roughness influence on CPE parameters in electrolytic cells. *Int. J. Electrochem. Sci.* **2016**, *11*, 7775–7784.
36. de Pauli, M.; Gomes, A.M.C.; Cavalcante, R.L.; Serpa, R.B.; Reis, C.P.S.; Reis, F.T.; Sartorelli, M.L. Capacitance spectra extracted from EIS by a model-free generalized phase element analysis. *Electrochim. Acta* **2019**, *320*, 134366.
37. Bray, F.; Ferlay, J.; Soerjomataram, I.; Siegel, R.L.; Torre, L.A.; Jemal, A. Global cancer statistics 2018: GLOBOCAN estimates of incidence and mortality worldwide for 36 cancers in 185 countries. *CA. Cancer J. Clin.* **2018**, *68*, 394–424.
38. Lakkis, N.A.; Adib, S.M.; Osman, M.H.; Musharafieh, U.M.; Hamadeh, G.N. Breast cancer in Lebanon: incidence and comparison to regional and Western countries. *Cancer Epidemiol.* **2010**, *34*, 221–

- 225.
39. Fares, M.Y.; Salhab, H.A.; Khachfe, H.H.; Khachfe, H.M. Breast cancer epidemiology among Lebanese women: an 11-year analysis. *Medicina (B. Aires)*. **2019**, *55*, 463.
  40. Jalkh, N.; Chouery, E.; Haidar, Z.; Khater, C.; Atallah, D.; Ali, H.; Marafie, M.J.; Al-Mulla, M.R.; Al-Mulla, F.; Megarbane, A. Next-generation sequencing in familial breast cancer patients from Lebanon. *BMC Med. Genomics* **2017**, *10*, 8.
  41. Lukong, K.E. Understanding breast cancer—The long and winding road. *BBA Clin.* **2017**, *7*, 64–77.
  42. Tsang, J.; Tse, G.M. Molecular classification of breast cancer. *Adv. Anat. Pathol.* **2020**, *27*, 27–35.
  43. Hamdan, D.; Nguyen, T.T.; Leboeuf, C.; Meles, S.; Janin, A.; Bousquet, G. Genomics applied to the treatment of breast cancer. *Oncotarget* **2019**, *10*, 4786.
  44. Duffy, M.J.; Harbeck, N.; Nap, M.; Molina, R.; Nicolini, A.; Senkus, E.; Cardoso, F. Clinical use of biomarkers in breast cancer: Updated guidelines from the European Group on Tumor Markers (EGTM). *Eur. J. Cancer* **2017**, *75*, 284–298.
  45. Powers, A.D.; Palecek, S.P. Protein analytical assays for diagnosing, monitoring, and choosing treatment for cancer patients. *J. Healthc. Eng.* **2012**, *3*, 503–534.
  46. Wang, L. Early diagnosis of breast cancer. *Sensors* **2017**, *17*, 1572.
  47. Moulder, D.E.; Hatoum, D.; Tay, E.; Lin, Y.; McGowan, E.M. The roles of p53 in mitochondrial dynamics and cancer metabolism: the pendulum between survival and death in breast Cancer? *Cancers (Basel)*. **2018**, *10*, 189.
  48. McGowan, E.M.; Lin, Y.; Hatoum, D. Good Guy or Bad Guy? The Duality of Wild-Type p53 in Hormone-Dependent Breast Cancer

- Origin, Treatment, and Recurrence. *Cancers (Basel)*. **2018**, *10*, 172.
49. Apostolopoulos, V.; Stojanovska, L.; Gargosky, S.E. MUC1 (CD227): a multi-tasked molecule. *Cell. Mol. life Sci.* **2015**, *72*, 4475–4500.
  50. Kufe, D. Oncogenic function of the MUC1 receptor subunit in gene regulation. *Oncogene* **2010**, *29*, 5663–5666.
  51. Rauch, J.; Volinsky, N.; Romano, D.; Kolch, W. The secret life of kinases: functions beyond catalysis. *Cell Commun. Signal.* **2011**, *9*, 23.
  52. Ferreira, P.M.P.; Pessoa, C. Molecular biology of human epidermal receptors, signaling pathways and targeted therapy against cancers: new evidences and old challenges. *Brazilian J. Pharm. Sci.* **2017**, *53*.
  53. Omenn, G.S.; Guan, Y.; Menon, R. A new class of protein cancer biomarker candidates: Differentially expressed splice variants of ERBB2 (HER2/neu) and ERBB1 (EGFR) in breast cancer cell lines. *J. Proteomics* **2014**, *107*, 103–112.
  54. Elizalde, P. V; Russo, R.I.C.; Chervo, M.F.; Schillaci, R. ErbB-2 nuclear function in breast cancer growth, metastasis and resistance to therapy. *Endocr. Relat. Cancer* **2016**, *23*, T243–T257.
  55. Wu, S.-G.; He, Z.-Y.; Ren, H.-Y.; Yang, L.-C.; Sun, J.-Y.; Li, F.-Y.; Guo, L.; Lin, H.-X. Use of CEA and CA15-3 to predict axillary lymph node metastasis in patients with breast cancer. *J. Cancer* **2016**, *7*, 37.
  56. Fu, Y.; Li, H. Assessing clinical significance of serum CA15-3 and carcinoembryonic antigen (CEA) levels in breast cancer patients: a meta-analysis. *Med. Sci. Monit. Int. Med. J. Exp. Clin. Res.* **2016**, *22*, 3154.
  57. Li, H.; You, L.; Xie, J.; Pan, H.; Han, W. The roles of subcellularly located EGFR in autophagy. *Cell. Signal.* **2017**, *35*, 223–230.
  58. Foley, J.; Nickerson, N.K.; Nam, S.; Allen, K.T.; Gilmore, J.L.; Nephew, K.P.; Riese, D.J. EGFR signaling in breast cancer: Bad to the bone. *Semin. Cell Dev. Biol.* **2010**, *21*, 951–960.

59. Sigismund, S.; Avanzato, D.; Lanzetti, L. Emerging functions of the EGFR in cancer. *Mol. Oncol.* **2018**, *12*, 3–20.
60. Barberán, S.; Cebrià, F. The role of the EGFR signaling pathway in stem cell differentiation during planarian regeneration and homeostasis. *Semin. Cell Dev. Biol.* **2019**, *87*, 45–57.
61. Banys-Paluchowski, M.; Witzel, I.; Riethdorf, S.; Rack, B.; Janni, W.; Fasching, P.A.; Solomayer, E.F.; Aktas, B.; Kasimir-Bauer, S.; Pantel, K.; et al. Evaluation of serum epidermal growth factor receptor (EGFR) in correlation to circulating tumor cells in patients with metastatic breast cancer. *Sci. Rep.* **2017**, *7*, 1–10.
62. Streckfus, C.; Bigler, L.; Tucci, M.; Thigpen, J.T. A preliminary study of CA15-3, c-erbB-2, epidermal growth factor receptor, cathepsin-D, and p53 in saliva among women with breast carcinoma. *Cancer Invest.* **2000**, *18*, 101–109.
63. Johari-Ahar, M.; Karami, P.; Ghanei, M.; Afkhami, A.; Bagheri, H. Development of a molecularly imprinted polymer tailored on disposable screen-printed electrodes for dual detection of EGFR and VEGF using nano-liposomal amplification strategy. *Biosens. Bioelectron.* **2018**, *107*, 26–33.
64. Ilkhani, H.; Sarparast, M.; Noori, A.; Bathaie, S.Z.; Mousavi, M.F. Electrochemical aptamer/antibody based sandwich immunosensor for the detection of EGFR, a cancer biomarker, using gold nanoparticles as a signaling probe. *Biosens. Bioelectron.* **2015**, *74*, 491–497.
65. Raj, N.; Attardi, L.D. The transactivation domains of the p53 protein. *Cold Spring Harb. Perspect. Med.* **2017**, *7*.
66. Núñez, C. Blood-based protein biomarkers in breast cancer. *Clin. Chim. Acta* **2019**, *490*, 113–127.
67. Bae, S.Y.; Nam, S.J.; Jung, Y.; Lee, S.B.; Park, B.W.; Lim, W.; Jung, S.H.; Yang, H.W.; Jung, S.P. Differences in prognosis and efficacy of

- chemotherapy by p53 expression in triple-negative breast cancer. *Breast Cancer Res. Treat.* **2018**, *172*, 437–444.
68. Holstege, H.; Joosse, S.A.; Van Oostrom, C.T.M.; Nederlof, P.M.; De Vries, A.; Jonkers, J. High incidence of protein-truncating TP53 mutations in BRCA1 -related breast cancer. *Cancer Res.* **2009**, *69*, 3625–3633.
69. Product information: Bradford reagent Available online: <https://www.sigmaaldrich.com/content/dam/sigmaaldrich/docs/Sigma/Bulletin/b6916bul.pdf>.
70. Rabai, S.; Benounis, M.; Catanante, G.; Baraket, A.; Errachid, A.; Jaffrezic Renault, N.; Marty, J.-L.; Rhouati, A. Development of a label-free electrochemical aptasensor based on diazonium electrodeposition: Application to cadmium detection in water. *Anal. Biochem.* **2021**, *612*, 113956.
71. Amor-Gutiérrez, O.; Costa-Rama, E.; Arce-Varas, N.; Martínez-Rodríguez, C.; Novelli, A.; Fernández-Sánchez, M.T.; Costa-García, A. Competitive electrochemical immunosensor for the detection of unfolded p53 protein in blood as biomarker for Alzheimer's disease. *Anal. Chim. Acta* **2020**, *1093*, 28–34.
72. Hasanzadeh, M.; Baghban, H.N.; Shadjou, N.; Mokhtarzadeh, A. Ultrasensitive electrochemical immunosensing of tumor suppressor protein p53 in unprocessed human plasma and cell lysates using a novel nanocomposite based on poly-cysteine/graphene quantum dots/gold nanoparticle. *Int. J. Biol. Macromol.* **2018**, *107*, 1348–1363.
73. Afsharan, H.; Khalilzadeh, B.; Tajalli, H.; Mollabashi, M.; Navaeipour, F.; Rashidi, M.R. A sandwich type immunosensor for ultrasensitive electrochemical quantification of p53 protein based on gold nanoparticles/graphene oxide. *Electrochim. Acta* **2016**, *188*, 153–164.

74. Aydın, E.B.; Aydın, M.; Sezgintürk, M.K. Electrochemical immunosensor based on chitosan/conductive carbon black composite modified disposable ITO electrode: An analytical platform for p53 detection. *Biosens. Bioelectron.* **2018**, *121*, 80–89.
75. Giannetto, M.; Bianchi, M.V.; Mattarozzi, M.; Careri, M. Competitive amperometric immunosensor for determination of p53 protein in urine with carbon nanotubes/gold nanoparticles screen-printed electrodes: A potential rapid and noninvasive screening tool for early diagnosis of urinary tract carcinoma. *Anal. Chim. Acta* **2017**, *991*, 133–141.
76. Aydın, M.; Aydın, E.B.; Sezgintürk, M.K. A disposable immunosensor using ITO based electrode modified by a star-shaped polymer for analysis of tumor suppressor protein p53 in human serum. *Biosens. Bioelectron.* **2018**, *107*, 1–9.
77. Gutierrez, C.; Schiff, R. HER2: biology, detection, and clinical implications. *Arch. Pathol. Lab. Med.* **2011**, *135*, 55–62.
78. Lv, Q.; Meng, Z.; Yu, Y.; Jiang, F.; Guan, D.; Liang, C.; Zhou, J.; Lu, A.; Zhang, G. Molecular mechanisms and translational therapies for human epidermal receptor 2 positive breast cancer. *Int. J. Mol. Sci.* **2016**, *17*.
79. Iqbal, N.; Iqbal, N. Human Epidermal Growth Factor Receptor 2 (HER2) in Cancers: Overexpression and Therapeutic Implications. *Mol. Biol. Int.* **2014**, *2014*, 1–9.
80. Loibl, S.; Gianni, L. HER2-positive breast cancer. *Lancet* **2017**, *389*, 2415–2429.
81. Laidi, F.; Bouziane, A.; Lakhdar, A.; Khabouze, S.; Amrani, M.; Rhrab, B.; Zaoui, F. Significant Correlation between Salivary and Serum Ca 15-3 in Healthy Women and Breast Cancer Patients. *Asian Pacific J. Cancer Prev.* **2014**, *15*, 4659–4662.
82. Laidi, F.; Bouziane, A.; Lakhdar, A.; Khabouze, S.; Rhrab, B.; Zaoui,

- F. Salivary expression of soluble HER2 in breast cancer patients with positive and negative HER2 status. **2014**, 1285–1289.
83. Ou, D.; Sun, D.; Lin, X.; Liang, Z.; Zhong, Y.; Chen, Z. A dual-aptamer-based biosensor for specific detection of breast cancer biomarker HER2 via flower-like nanozymes and DNA nanostructures. *J. Mater. Chem. B* **2019**, *7*, 3661–3669.
84. Carvajal, S.; Fera, S.N.; Jones, A.L.; Baldo, T.A.; Mosa, I.M.; Rusling, J.F.; Krause, C.E. Disposable inkjet-printed electrochemical platform for detection of clinically relevant HER-2 breast cancer biomarker. *Biosens. Bioelectron.* **2018**, *104*, 158–162.
85. Fu, Y.; Wang, N.; Yang, A.; Law, H.K. wai; Li, L.; Yan, F. Highly Sensitive Detection of Protein Biomarkers with Organic Electrochemical Transistors. *Adv. Mater.* **2017**, *29*, 1–7.
86. Freitas, M.; Neves, M.M.P.S.; Nouws, H.P.A.; Delerue-Matos, C. Quantum dots as nanolabels for breast cancer biomarker HER2-ECD analysis in human serum. *Talanta* **2020**, *208*, 120430.
87. Marques, R.C.B.; Costa-Rama, E.; Viswanathan, S.; Nouws, H.P.A.; Costa-García, A.; Delerue-Matos, C.; González-García, M.B. Voltammetric immunosensor for the simultaneous analysis of the breast cancer biomarkers CA 15-3 and HER2-ECD. *Sensors Actuators, B Chem.* **2018**, *255*, 918–925.
88. Shamsipur, M.; Emami, M.; Farzin, L.; Saber, R. A sandwich-type electrochemical immunosensor based on in situ silver deposition for determination of serum level of HER2 in breast cancer patients. *Biosens. Bioelectron.* **2018**, *103*, 54–61.
89. Hartati, Y.W.; Nurdjanah, D.; Wyantuti, S.; Anggraeni, A.; Gaffar, S. Gold nanoparticles modified screen-printed immunosensor for cancer biomarker HER2 determination based on anti HER2 bioconjugates. *AIP Conf. Proc.* **2018**, 2049.

90. Hartati, Y.W.; Letelay, L.K.; Gaffar, S.; Wyantuti, S.; Bahti, H.H. Cerium oxide-monoclonal antibody bioconjugate for electrochemical immunosensing of HER2 as a breast cancer biomarker. *Sens. Bio-Sensing Res.* **2020**, *27*, 100316.
91. Chocholova, E.; Bertok, T.; Lorencova, L.; Holazova, A.; Farkas, P.; Vikartovska, A.; Bella, V.; Velicova, D.; Kasak, P.; Eckstein, A.A. Advanced antifouling zwitterionic layer based impedimetric HER2 biosensing in human serum: Glycoprofiling as a novel approach for breast cancer diagnostics. *Sensors Actuators B Chem.* **2018**, *272*, 626–633.
92. Barhoumi, L.; Bellagambi, F.G.; Vivaldi, F.M.; Baraket, A.; Clément, Y.; Zine, N.; Ali, M. Ben; Elaissari, A.; Errachid, A. Ultrasensitive immunosensor array for TNF- $\alpha$  detection in artificial saliva using polymer-coated magnetic microparticles onto screen-printed gold electrode. *Sensors (Switzerland)* **2019**, *19*.
93. Radi, A.E.; Lates, V.; Marty, J.L. Mediatorless hydrogen peroxide biosensor based on horseradish peroxidase immobilized on 4-carboxyphenyl film electrografted on gold electrode. *Electroanalysis* **2008**, *20*, 2557–2562.

## **APPENDIXES**

### **Appendix A**

#### **Design and fabrication of the transducer**

As mentioned in part 1.2.1. Screen-printed technology was used to develop the transducer which is a lab-on-chip made out of eight sets of integrated microelectrodes. These electrodes were built by iMiCROQ, Spain. Each set is made up of a gold working microelectrode of 2.7 mm diameter with an integrated silver/silver chloride reference microelectrode and carbon counter microelectrodes, the microarray can be found in figure 50. Each of the microelectrodes is connected to a silver pad; for each integrated microelectrode there are three pads linking the electrodes to the external devices, these pads are in the sequence of counter electrode, working electrode, and reference electrode subsequently. The external dimensions of the developed Lab-on-a-chip are L34 x W78 x H1 mm. Further dimensions of the lab-on-chip used are discussed below.

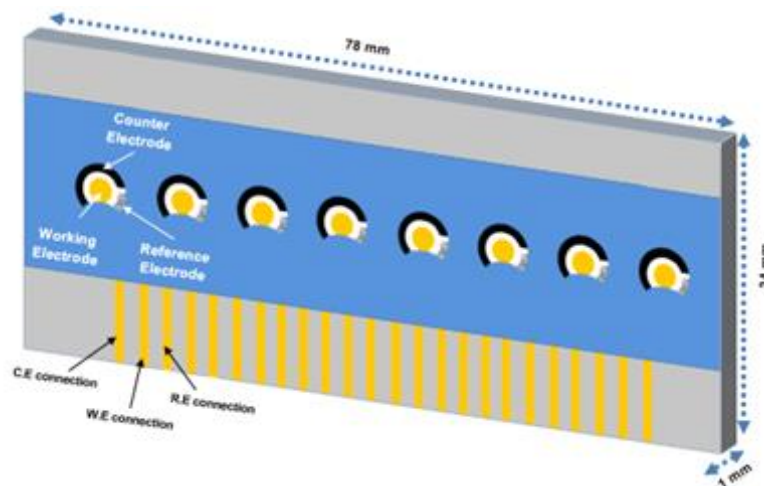


**Figure 50:** Design and proportions of the transducer.

### Fabrication process

The fabrication of the transducer used CleWind4 designer program, it used Mylar substrate with a nominal thickness of 1 mm. It was fabricated using 5 different mask levels, with each mask level building on top of the previous one. Table 7 summarizes the levels according to the technological steps used.

**Table 7:** Summary of the Mask Steps Designed for the Fabrication of the Lab-on-a-chip

Level	Lab-on-a-chip definition
1	Silver microelectrodes definition
2	Gold working microelectrode definition
3	Silver/Silver chloride reference microelectrode definition
4	Carbon counter microelectrode definition
5	Passivation layer

The fabrication process is as follows:

- Cleaning of the Mylar sheet
- Applying the first mask on the Mylar surface:
  - A silver layer (8  $\mu\text{m}$ ) is deposited. These are the pads that connect the electrodes to the external devices; each pad's width is 1 mm and the

distance between each pad is 1.54 mm, while the distance between the pads and the border to the Mylar sheet is 9.3 mm, thus the distance between the first and last pad is 59.42 mm. These pads start off as parallel up until reaching the height of 9.3 mm before diverging to the position of each pad's respective microelectrode's position.

- The second level of mask is used to deposit the gold layer (10  $\mu\text{m}$ ) of the working microelectrode pattern.

- o The gold part of the working microelectrode is a circle with a rectangle connecting it to its respective pad, the circle has a diameter of 2.7 and the rectangle has a width of 1.36 mm and a length of 2 mm. the distance between each working microelectrode is 9 mm, and it is 15.5 mm from the top of the Mylar sheet.

- The third level defined a Silver/silvers chloride with thickness about 15  $\mu\text{m}$ .

- o The silver microelectrode is made up of a left-slanted trapeze with a quarter of a cylinder situated 1 mm on the left of the gold working microelectrode. The trapeze dimensions are 2.1 mm on the inward side, 1.03 mm on the outward side and a width of 0.7 mm, the same width as the quarter cylinder.

- The fourth mask then deposits the carbon layer (20  $\mu\text{m}$ ).

- o The carbon layer is the counter microelectrode, it is made of a trapeze that connects a cylindrical portion to the pad, the cylindrical is a three quarters cylinder that stops just 0.6 mm away from the silver microelectrode, it is situated 1 mm to the right of the gold working electrode with a width of 1.15 mm. The trapeze's dimensions are 1.5 mm in length on the outward part, 1 mm in length on the inward part and a width of 1 mm.

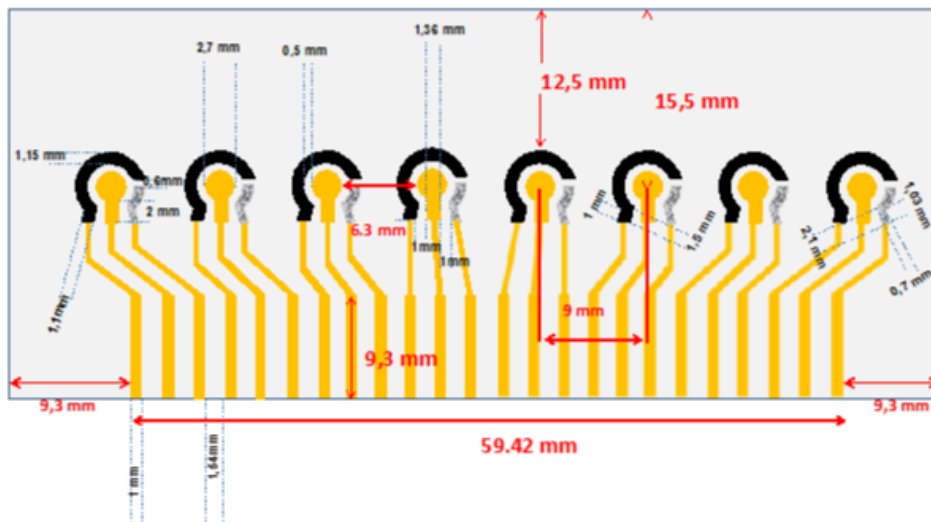
- Finally, the fifth mask is a layer of epoxy resin of 8  $\mu\text{m}$  thickness as a passivation layer is then applied for the packaging of the patterned metals,

thus isolating the living open active areas on microelectrodes and pads for electrical connection.

o The passivation layer is 9.3 mm from the bottom of the Mylar sheet and covers a width of 18.2 mm of the sheet while leaving on the cylinders of the third and fourth mask and the circle of the second mask, thus creating a layer of 6.5 mm tangent to the electrodes as protection.

The full schematic of the screen printed microelectrodes and their respective dimensions can be found in figure 51.

(A)



(B)

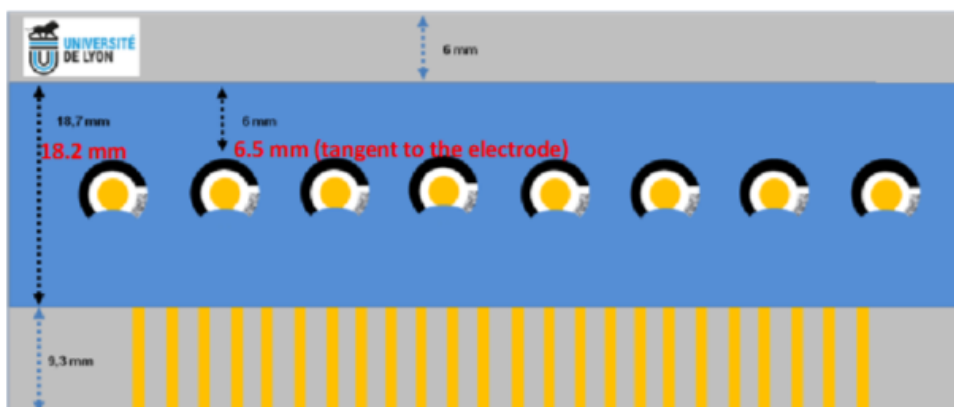


**Figure 51:** the dimensions of the biotransducers showing the result of the applied first four masks in (A) and the fifth and final mask in (B).

These disposable transducers have the typical electrochemical cell configuration and are suitable for working with micro-volumes, and for decentralized assays. Specially designed for the development of multiple simultaneous analyses.

## **Appendix B**

### **Optimization of CMA electrodeposition**

#### **Introduction**

The optimization of CMA electrodeposition follows the detection of EGFR and it follows the same materials and methods described in chapter 2.

#### **Method**

The protocol for the electrodeposition of CMA was originally taken from previously published experiments [92] and then subsequently optimized.

- CMA is prepared by first dissolving 3 mM CMA in 3 mL deionized water using ultrasound for 10 min.
- Then the CMA solution is mixed with 60  $\mu\text{L}$  of 1 M Sodium Nitrite and 60  $\mu\text{L}$  of 1 M HCl and placed for 10 min at 4°C.
- Then the activated CMA is placed on the electrode in the microfluidic system and electrodeposited using CV.

The electrodeposition is preceded and succeeded by CV and EIS characterization as described in paragraph 1.2.2.1.

The optimization of CMA electrodeposition was carried out to yield better detection. Three parameters were optimized, and they are the number of cycles (5 cycles, 10 cycles, and 15 cycles), the scan rate (100, 50, 30, and 15 mV/s).

Once the best number of cycles and the scan rate were chosen, the potential window (-1.2 to 0.2 V, -1.2 to 0 V) was adjusted to shorten the time of electrodeposition as it exceeded an hour. The passivation layer resulting from each parameter was recorded using CV as described in the previous paragraph 1.2.2.1. A schematic showing the experiments that were done for the optimization of CMA electrodeposition can be seen in figure 52.

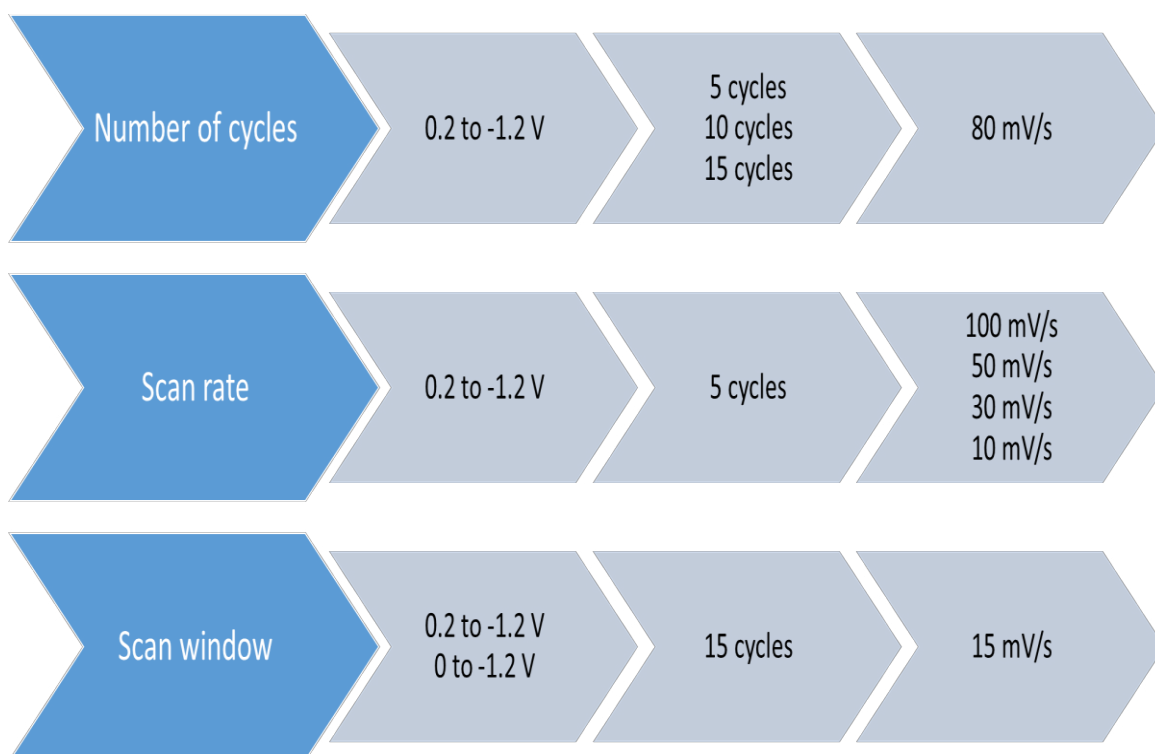


**Figure 52:** Scheme showing the steps taken for the optimization of CMA electrodeposition parameters.

## Results

The starting parameters for the deposition of 3 mM CMA were as follows:

- Potential window: from -1.2 to 0.2
- Scan rate: 50 mV/s
- Number of scans: 5 scans per deposition

However, these parameters could not create a satisfying deposition layer as seen in figure 53 for the 5 cycles. As such, the first parameter to be optimized was the number of cycles, and as can be seen in figure 53, 15 cycles created a better passivation layer.

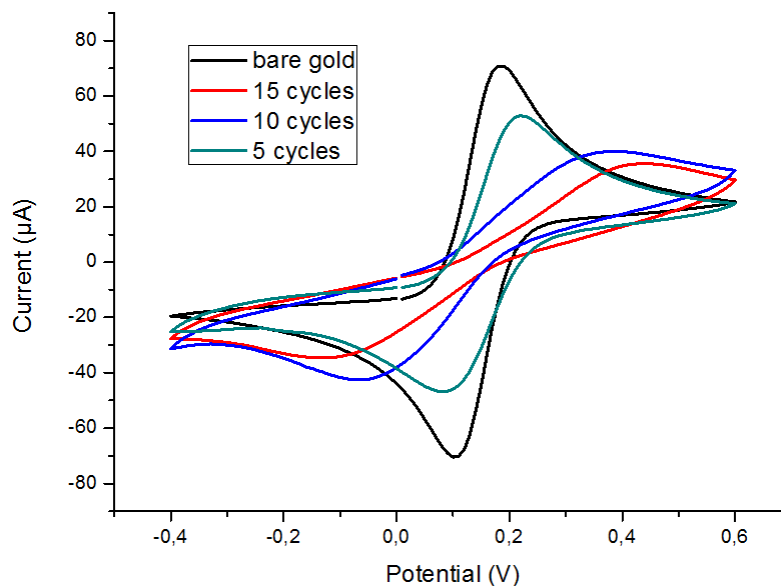


**Figure 53:** passivation layers resulting from different cycles of electrodeposition of CMA.

To confirm that a better passivation layer corresponds to better sensitivity, each of the SPE that was used for the number of cycles was then functionalized with anti-EGFR and then EGFR was detected using EIS. The sensitivity of each passivation layer was then compared to each other in figure 54.

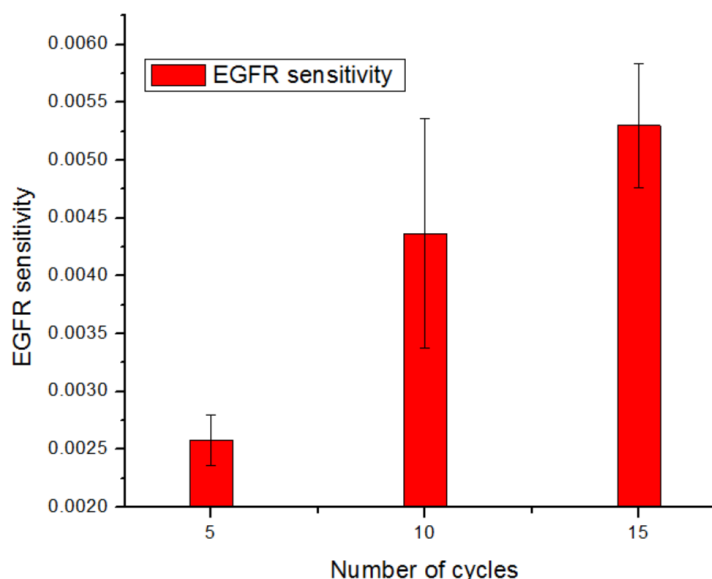


**Figure 54:** Sensitivity of the biosensor in relation to the number of cycles.

As can be seen from figure 54, the sensitivity of the biosensor toward EGFR increases with the number of cycles. As such, it is confirmed that the greater the passivation layer, the higher the sensitivity toward EGFR is.

The second parameter to be optimized was the scan rate, 5 different scan rates were tested (100, 50, 30, 15 mV/s) and the results were that the lower the scan rate the greater the deposition as seen in figure 55.

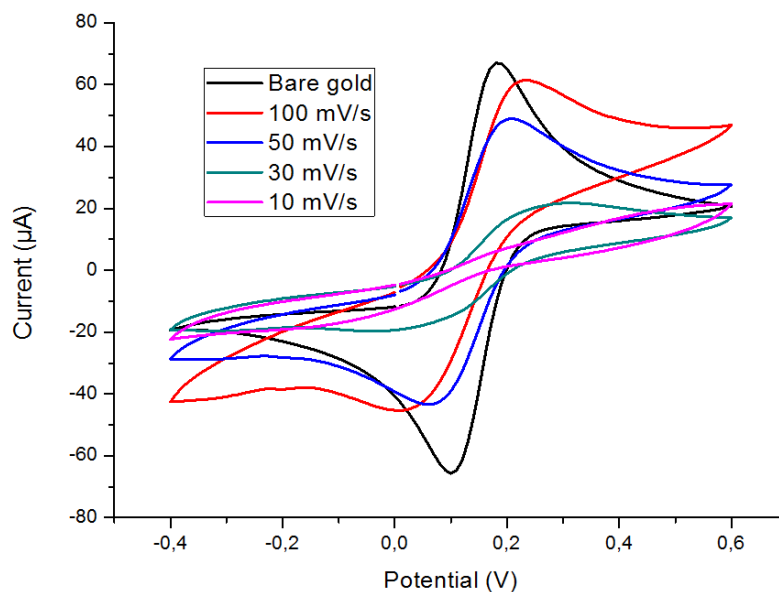


**Figure 55:** Passivation layer resulting from the electrodeposition of CMA at different scan rates.

The third parameter to be tested was the window of electrodeposition. Here, only 2 windows were tested, from 0.2 to -1.2 V and from 0 to -1.2 V and the results can be seen in figure 56, with the window between 0 and -1.2 V showing better passivation layer than the larger window.

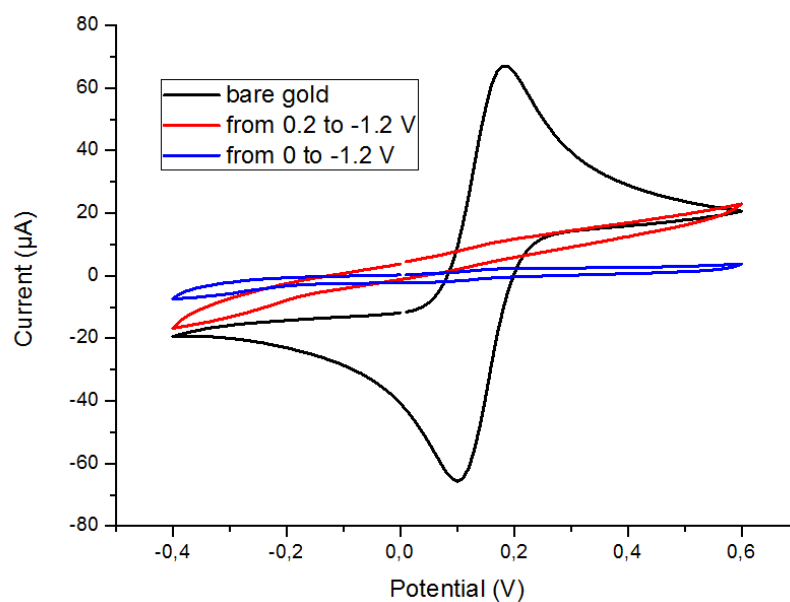


**Figure 56:** passivation layer resulting from the electrodeposition of CMA at the different potential window of detection.

### Conclusion

Two conclusions can be drawn from this optimization, the first is that the better passivation layer obtained, the better the detection of EGFR. The other conclusion is that the best passivation was the result of the following electrodeposition parameters:

- Scan rate: 15 mV/s
- Window of detection: 0 to -1.2 V
- The number of scans: 15 cycles.

## **Appendix C**

### **Optimization of EDC/NHS for antibody immobilization**

#### **Introduction**

The optimization for EDC/NHS follows the detection of EGFR and it follows the same materials and methods described in chapter 2.

#### **Method**

Two parameters of EDC/NHS were optimized, the concentrations of EDC and of NHS (0.4 M EDC to 0.1 M NHS/ 0.1 M EDC to 0.4 M NHS/ 0.4 M EDC to 0.4 M NHS). These optimizations were done with the optimized protocol of and the time of electrode incubation (40 min EDC/NHS followed by 40 min antibody/ 20 min EDC/NHS followed by 20 min antibody/ 1 h EDC/NHS followed by 1 h 30 min for antibody).

The way the optimizations were carried out was that the initial protocol of [92] in which CMA was deposited on the SPE's surface using 5 cycles from 0.2 to -1.2 V on 80 mV/s for 5 cycles. This is then followed by incubation of EDC/NHS with the above-mentioned optimization concentration for 1 hour, then followed by incubation of the antibody anti-EGFR for 1 hour and 30 min, and finally 30 min of 1/1000 ethanolamine solution in PBS.

This is then followed by optimization of the time using 0.4 M EDC/ 0.1 M NHS, followed by incubation of antibody with the varying amount of time, before incubating the SPE using 1/1000 ethanolamine solution in PBS. Figure 57 summarizes the work that was done for this optimization.

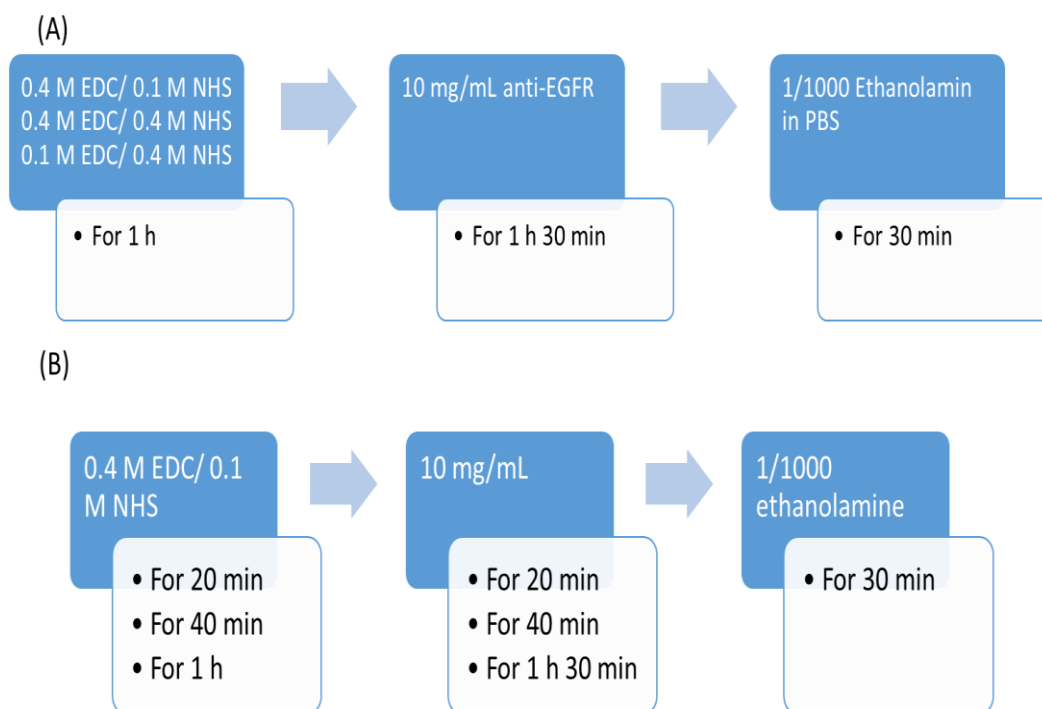


**Figure 57:** Schematic summarizing the optimization done for the immobilization of antibody anti-EGFR showing the optimization of the concentration of EDC/NHS (A) and the optimization of the time (B).

## Results

### Optimization of anti-EGFR antibody immobilization

The optimization of anti-EGFR antibody immobilization was done through the detection of EGFR as described in part 1.3.3. As such, each result is given as a standardization curve, and since the results were repeated three times, each curve gave a value for the sensitivity. As such, the sensitivity for each concentration of EDC/NHS used is compared in figure 58.

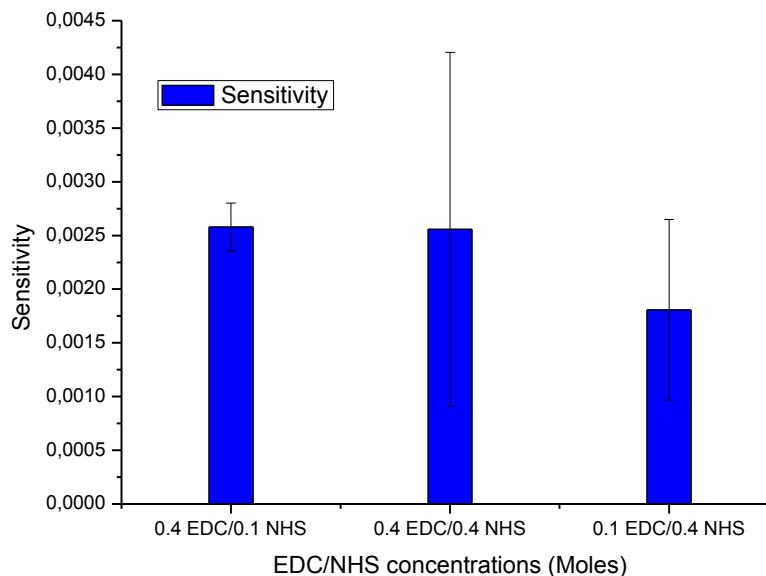


**Figure 58:** Optimization of EDC/NHS concentration showing the sensitivity of the detection against the concentration of EDC/NHS used.

From figure 58 we can see that the concentration of 0.4 M EDC/0.1 M NHS is slightly larger than that of 0.4 M EDC/ 0.4 M NHS and much larger than that of 0.1 M EDC/ 0.4 M NHS. In addition, the concentration of 0.4 M EDC/ 0.1 M NHS showed greater stability than that of 0.4 M EDC/ 0.4 M NHS. As such, the concentration used for the final protocol is 0.4 M EDC/0.1 M NHS.

The second parameter optimized is the length of time used for incubating the SPE in EDC/NHS and the antibody anti-EGFR, and from figure 59 we can conclude that the best time is 40 min for EDC/NHS and 40 min for antibody anti-EGFR.

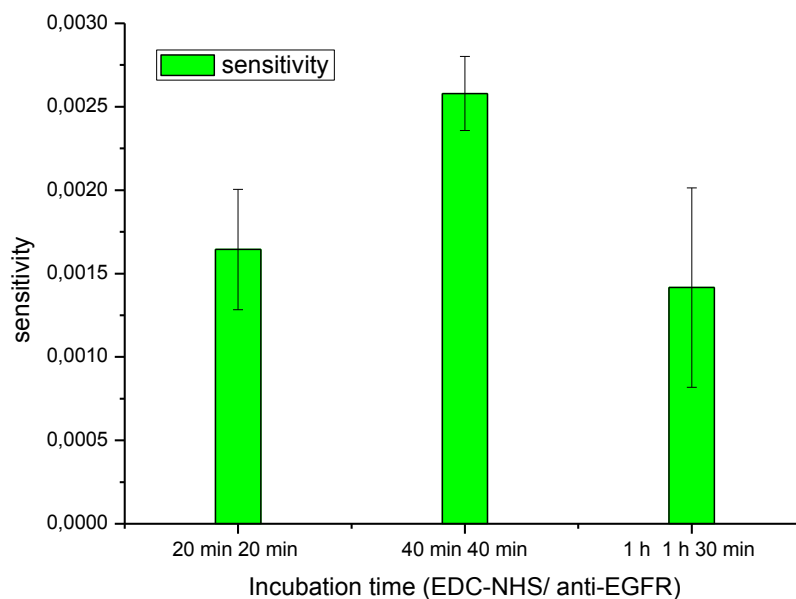


**Figure 59:** Optimization of the SPE incubation time in EDC/NHS and in the antibody anti-EGFR showing the sensitivity of the detection against the incubation time.

### Conclusion

The best concentrations for the immobilization of the antibody is 0.4 M EDC to 0.1 M NHS.

The best incubation time for the immobilization of the antibody is 40 min EDC/NHS, followed by 40 min of antibody immobilization, followed by 30 min ethanolamine 1/1000.

## Appendix D

### Optimization of ABA electrodeposition

#### Introduction

The optimization for ABA follows the detection of HER2, as such, it follows the same materials and methods described in chapter 4.

#### Method

The optimization of CMA showed that a better passivation layer during the electrodeposition phase gives overall better sensitivity toward the target protein.

The initial parameters used for the electrodeposition [93] were then optimized one by one. The original parameters used were:

- Dissolution of 1 mM ABA in 0.5 M HCl using a sonicator
- Addition of 1 mM NaNO<sub>2</sub>
- Incubation for 5 min in ice
- Electrodeposition of ABA using CV on the SPE using:
  - From -0.4 to 0.4 V
  - 100 mV/s
  - 1 cycle

This was followed by characterizing the SPE with CV before and after electrodeposition. The first parameters to be optimized are the CV parameters for the electrodeposition, a summary of these parameters, and how they were optimized is found in figure 60 (A). The first parameter to be optimized was the number of cycles as it is the most impactful one, and two numbers were used (1 and 15 cycles). A better number of cycles was then used to optimize the other parameters as it created better differentiation. The second parameter was the scan rate (150 mV/s, 100 mV/s, 50 mV/s),

followed by the potential window (-0.4 to 0.4 V, -0.8 to 0.4 V, -0.4 to 0.6 V).

These optimizations were then followed by the optimization of the chemical reaction. First, whether the incubation in ice or at room temperature affected the electrodeposition, then the time of incubation was increased from 5 min to 10 min and 15 min respectively. Then the concentration of ABA and was increased from 1 mM to 2 mM and 5 mM respectively. The final parameter that was optimized is the method of preparation of the ABA, ABA was either dissolved in deionized water using 10 min ultrasound then the addition of 5 mM HCl, or the dissolution of ABA in 0.5 M HCl directly with a simple shake. Figure 60 (B) summarizes the entire optimization process.

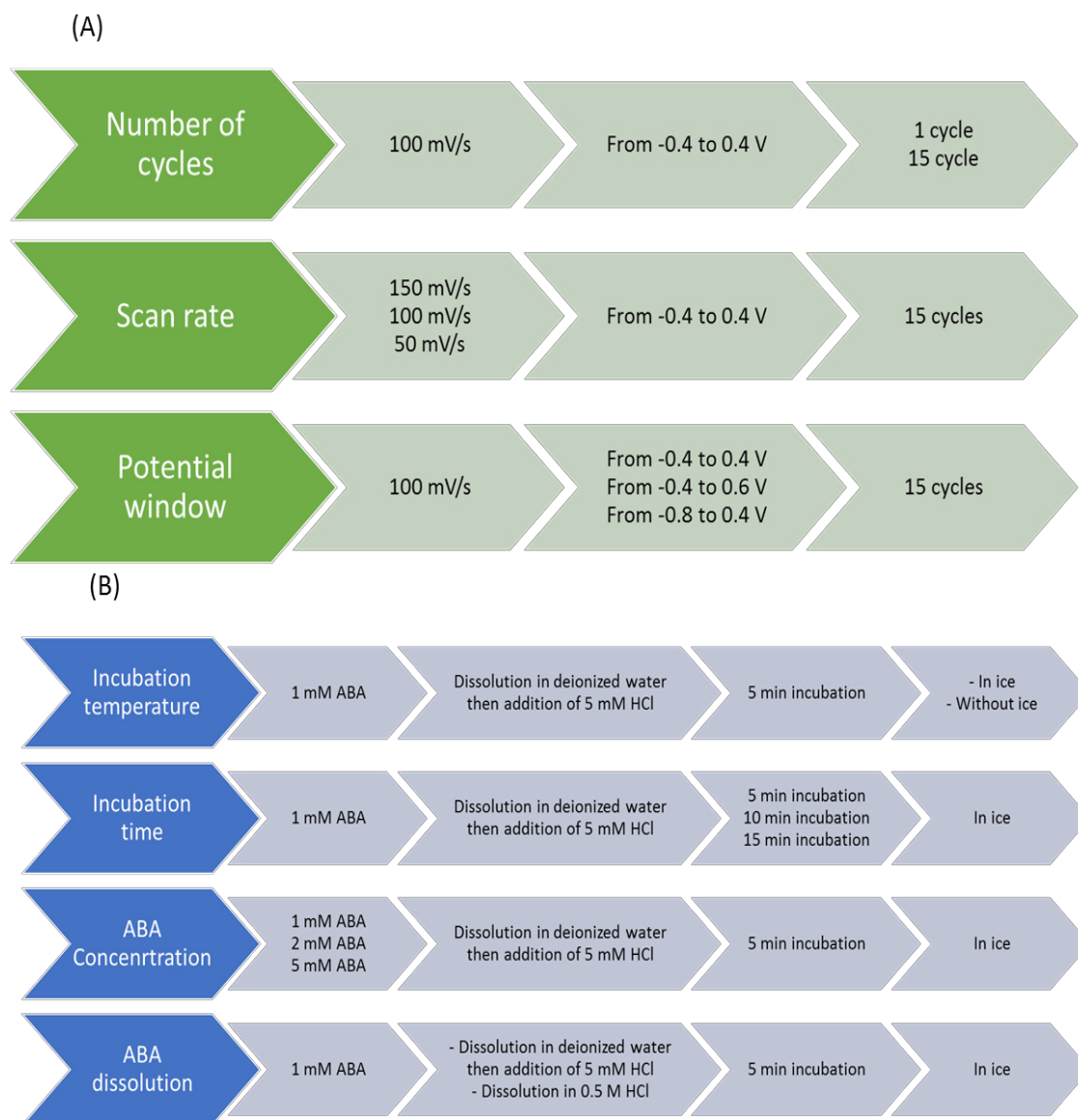


**Figure 60:** The optimization scheme for ABA electrodeposition through (A) CV parameters, (B) Chemical parameters.

## Results

The aim of the optimization steps for the electrodeposition of ABA was to fully pacify the electrode's surface. The parameters of [93] gave the result of figure 61.

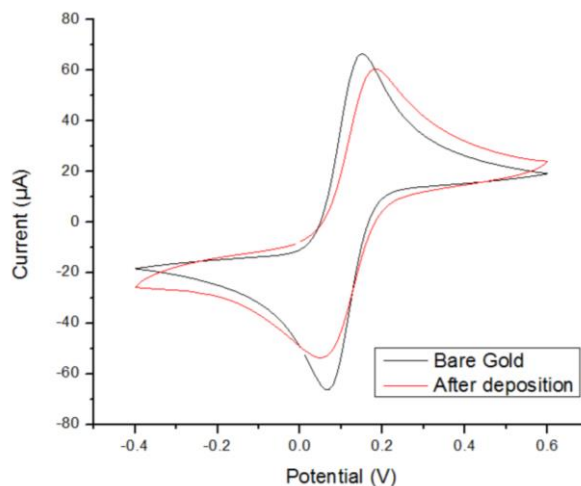


**Figure 61:** Electrodeposition using the literature electrodeposition parameters.

This was followed by optimizing the electrodeposition parameters. The first parameter that was optimized was the number of cycles. Two cycles were tested, 1 cycle and 15 cycles. The results of this optimization can be seen in figure 62.

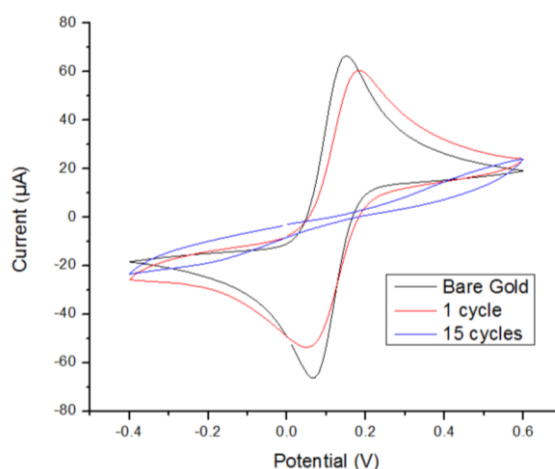


**Figure 62:** CV showing the result of the optimization of the number of cycles after the electrodeposition of ABA.

The resulting cyclic voltammogram shows that 15 cycles gave a better passivation layer than one cycle. As such, this is the parameter used for the subsequent electrodepositions.

The second parameter optimized was the scan rate. three different scan rates were tested, and they are 150 mV/s, 100 mV/s, 50 mV/s. The resulting electrodeposition can be seen in figure 63.

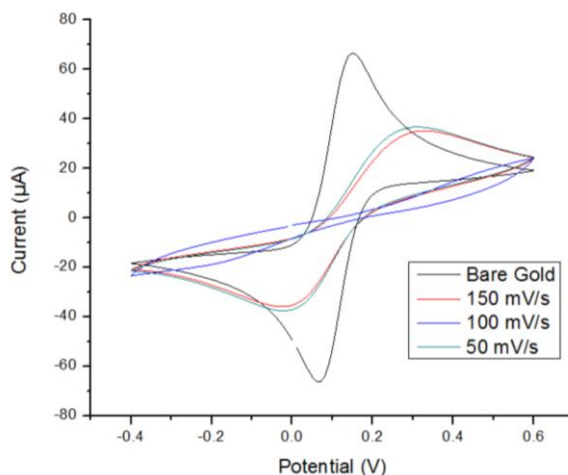


**Figure 63:** CV showing the result of the optimization of the scan rate after the electrodeposition of ABA.

From figure 57, the scan rate with the best electrodeposition is 100 mV/s.

The third and final CV parameter that was optimized is the potential window used, three potential windows were tested, from -0.4 to 0.4 V, from -0.8 to 0.4 V, and from -0.4 to 0.6 V. The results can be seen in figure 64.

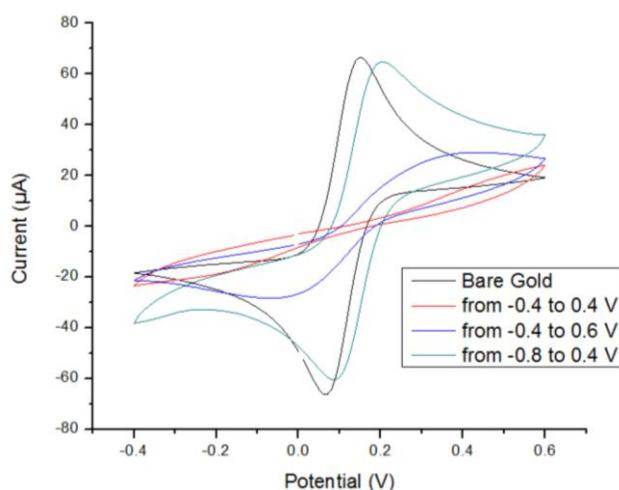


**Figure 64:** CV showing the result of the optimization of the potential window after the electrodeposition of ABA.

From figure 64, the best potential window for the electrodeposition of ABA is from -0.4 to 0.4 V.

The following optimization is changing the temperature of the electrodeposition, the incubation of ABA after mixing it with sodium nitrite, the incubation was done in ice and at room temperature. The results can be seen in figure 65.

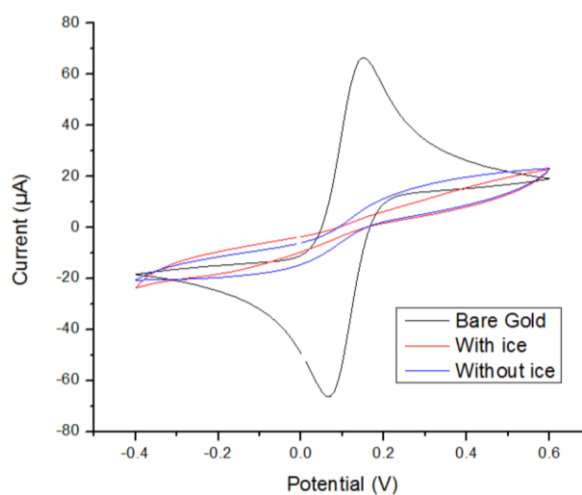


**Figure 65:** CV showing the resulting electrodeposition when ABA was incubated with ice and without ice.

From the resulting CV in figure 65, the incubation of ABA with ice gives better electrodeposition than incubation ABA without ice.

This is followed by optimizing the time of ABA incubation, the result can be seen in figure 66.

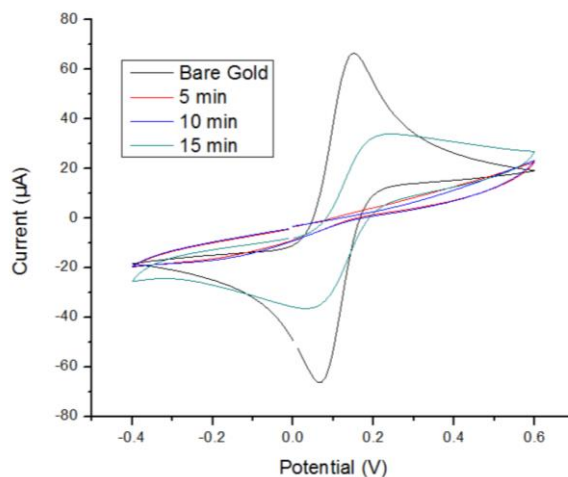


**Figure 66:** CV showing the resulting passivation layer from different ABA incubation time.

The resulting passivation layer shown in figure 66 shows that there is no difference between incubating the ABA for 5 min or 10 min before electrodeposition, however, the result drastically changes after 15 min, as such, the best incubation time is 5 min.

The next parameter that was optimized is ABA concentration, three concentrations were used to optimize the ABA electrodeposition, they were 1 mM, 2 mM, and 5 mM. The resulting CV is seen in figure 67.

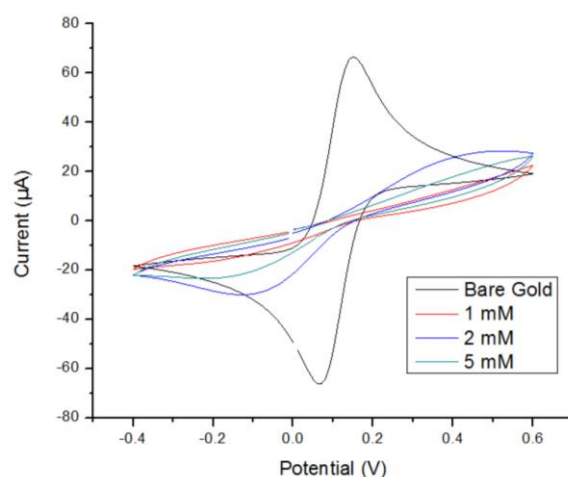


**Figure 67:** CV showing the resulting passivation layer from different ABA concentrations.

The final parameter that was optimized is the method of preparation of the ABA solution. Whether ABA is dissolved by sonication then HCl is added, or whether ABA is dissolved directly in 0.5 M HCl.

The solution of this optimization can be found in figure 68.

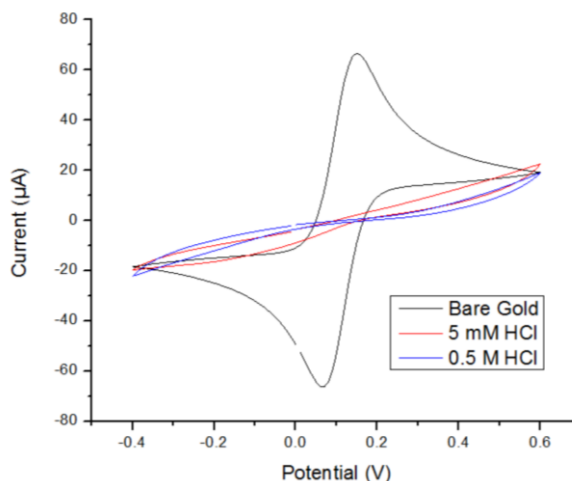


**Figure 68:** CV showing the resulting passivation layer from different methods of preparing ABA.

From figure 68, the preparation of ABA in 0.5 M HCl resulted in better electrodeposition of ABA than when ABA was dissolved in deionized water, and then HCl was added to the mix.

As a conclusion, the protocol for the electrodeposition of ABA that was used for the measurement of HER2 concentrations is:

- Dissolution of 1 mM of ABA in a solution of 0.5 M HCl
- Addition of 1 mM of sodium nitrite
- Incubation in ice for 5 min
- Electrodeposition of ABA with CV using the following parameters:
  - From -0.4 to 0.4 V
  - 100 mV/s
  - 15 cycles

The result of this parameter is the covering of the entire SPE in a layer of ABA, the difference between the unoptimized and optimized parameters can be seen in figure 69.

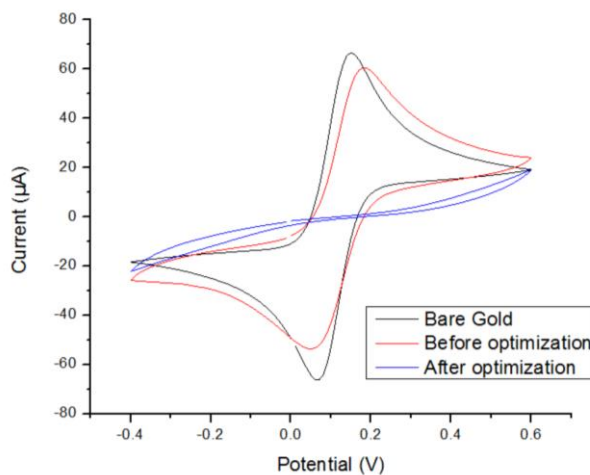


**Figure 69:** Difference between the electrodeposition of ABA with the original parameters, and with the optimized parameters.

### Conclusion

The electrodeposition parameters that gave the best passivation layer are:

- Scan rate: 100 mV/s
- Potential window: -0.4 to 0.4 V
- The number of cycles: 15 cycles.

### References

Radi, A.E.; Lates, V.; Marty, J.L. Mediatorless hydrogen peroxide biosensor based on horseradish peroxidase immobilized on 4-carboxyphenyl film electrografted on gold electrode. *Electroanalysis* **2008**, *20*, 2557–2562.

Barhoumi, L.; Bellagambi, F.G.; Vivaldi, F.M.; Baraket, A.; Clément, Y.; Zine, N.; Ali, M. Ben; Elaissari, A.; Errachid, A. Ultrasensitive immunosensor array for TNF- $\alpha$  detection in artificial saliva using polymer-coated magnetic microparticles onto screen-printed gold electrode. *Sensors (Switzerland)* **2019**, *19*.